



AFRL-AFOSR-VA-TR-2015-0313

---

## Noise Tomography and Adaptive Illumination in Noise Radar

Ram Narayanan  
PENNSYLVANIA STATE UNIVERSITY THE

---

10/01/2015  
Final Report

DISTRIBUTION A: Distribution approved for public release.

Air Force Research Laboratory  
AF Office Of Scientific Research (AFOSR)/ RTB1  
Arlington, Virginia 22203  
Air Force Materiel Command

# REPORT DOCUMENTATION PAGE

*Form Approved  
OMB No. 0704-0188*

Public reporting burden for this collection of information is estimated to average 1 hour per response, including the time for reviewing instructions, searching existing data sources, gathering and maintaining the data needed, and completing and reviewing this collection of information. Send comments regarding this burden estimate or any other aspect of this collection of information, including suggestions for reducing this burden to Department of Defense, Washington Headquarters Services, Directorate for Information Operations and Reports (0704-0188), 1215 Jefferson Davis Highway, Suite 1204, Arlington, VA 22202-4302. Respondents should be aware that notwithstanding any other provision of law, no person shall be subject to any penalty for failing to comply with a collection of information if it does not display a currently valid OMB control number. **PLEASE DO NOT RETURN YOUR FORM TO THE ABOVE ADDRESS.**

<b>1. REPORT DATE</b> 30-09-2015	<b>2. REPORT TYPE</b> Final	<b>3. DATES COVERED (From - To)</b> 01-04-2012 to 31-08-2015		
<b>4. TITLE AND SUBTITLE</b>  Noise Tomography and Adaptive Illumination in Noise Radar		<b>5a. CONTRACT NUMBER</b>  <b>5b. GRANT NUMBER</b> FA9550-12-1-0164		
		<b>5c. PROGRAM ELEMENT NUMBER</b>		
<b>6. AUTHOR(S)</b>  Ram M. Narayanan, Hee Jung Shin, and Mark A. Asmuth		<b>5d. PROJECT NUMBER</b>		
		<b>5e. TASK NUMBER</b>		
		<b>5f. WORK UNIT NUMBER</b>		
<b>7. PERFORMING ORGANIZATION NAME(S) AND ADDRESS(ES)</b>  The Pennsylvania State University Office of Sponsored Programs 110 Technology Center The Pennsylvania State University University Park, PA 16802		<b>8. PERFORMING ORGANIZATION REPORT NUMBER</b>		
<b>9. SPONSORING / MONITORING AGENCY NAME(S) AND ADDRESS(ES)</b>  Air Force Office of Scientific Research 875 North Randolph Street, Suite 325 Arlington, VA 22203		<b>10. SPONSOR/MONITOR'S ACRONYM(S)</b> AFOSR		
		<b>11. SPONSOR/MONITOR'S REPORT NUMBER(S)</b>		
<b>12. DISTRIBUTION / AVAILABILITY STATEMENT</b>				
<b>13. SUPPLEMENTARY NOTES</b>				
<b>14. ABSTRACT</b>  Ultra-wideband (UWB) waveforms achieve excellent spatial resolution for better characterization of targets in tomographic imaging applications compared to narrowband waveforms. In this report, two-dimensional tomographic images of multiple scattering objects are successfully obtained using the diffraction tomography approach by transmitting multiple independent and identically distributed (iid) UWB random noise waveforms. The feasibility of using a random noise waveform for tomography is investigated by formulating a white Gaussian noise (WGN) model using spectral estimation. The analytical formulation of object image formation using random noise waveforms is established based on the backward scattering, and several numerical diffraction tomography simulations are performed in the spatial frequency domain to validate the analytical results by reconstructing the tomographic images of scattering objects. The final image of the object based on multiple transmitted noise waveforms is reconstructed by averaging individually formed images which compares very well with the image created using the traditional Gaussian pulse. Pixel difference-based measure is used to analyze and estimate the image quality of the final reconstructed tomographic image under various signal-to-noise ratio (SNR) conditions. A UWB noise radar was designed to transmit multiple UWB random noise waveforms over the 3–5 GHz frequency range and to measure the backward scattering data for the validation of the theoretical analysis and numerical simulation results. The reconstructed tomographic images of the rotating cylindrical objects based on experimental results are seen to be in good agreement with the simulation results, which demonstrates the capability of UWB noise radar for complete two-dimensional tomographic image reconstruction of various shaped metallic and dielectric target objects.				
<b>15. SUBJECT TERMS</b> Noise Radar, Diffraction Tomography, Ultrawideband, Image Quality, Back-propagation				
<b>16. SECURITY CLASSIFICATION OF:</b>		<b>17. LIMITATION OF ABSTRACT</b> None	<b>18. NUMBER OF PAGES</b> 200	<b>19a. NAME OF RESPONSIBLE PERSON</b> Ram M. Narayanan
<b>a. REPORT</b> Unclassified	<b>b. ABSTRACT</b> Unclassified	<b>c. THIS PAGE</b> Unclassified		<b>19b. TELEPHONE NUMBER (include area code)</b> (814) 863-2602

Standard Form 298 (Rev. 8-98)  
Prescribed by ANSI Std. Z39.18

The Final Report is presented in the form of a doctoral (Ph.D.) dissertation written by Hee Jung Shin and a master's (M.S.) thesis written by Mark Asmuth. Also listed at the end are the publications based on the research.

## **TABLE OF CONTENTS**

Ultra Wideband Noise Tomography: Principles and Validation.....	3
Noise Radar Tomography System Design And Data Collection.....	118
Publications.....	200

The Pennsylvania State University

The Graduate School

Department of Electrical Engineering

**ULTRA WIDEBAND NOISE TOMOGRAPHY:**

**PRINCIPLES AND VALIDATION**

**Noise Tomography and Adaptive Illumination in Noise Radar**

A Dissertation in

Electrical Engineering

by

Hee Jung Shin

© 2015 Hee Jung Shin

Submitted in Partial Fulfillment  
of the Requirements  
for the Degree of

Doctor of Philosophy

December 2015

The dissertation of Hee Jung Shin was reviewed and approved\* by the following:

Ram M. Narayanan  
Professor of Electrical Engineering  
Dissertation Advisor  
Chair of Committee

W. Kenneth Jenkins  
Professor of Electrical Engineering

Douglas H. Werner  
Professor of Electrical Engineering

Karl M. Reichard  
Assistant Professor of Acoustics

Kultegin Aydin  
Professor of Electrical Engineering  
Head of the Department of Electrical Engineering

\*Signatures are on file in the Graduate School

## ABSTRACT

Imaging techniques have been used for a long time in many applications such as nondestructive testing, medical diagnosis, civil infrastructure assessment, and homeland security. Advances in signal and image processing techniques have made considerable progress in a way that the multi-dimensional images of the target object are successfully reconstructed from electromagnetic (EM) scattering; the shape of the object is clearly identified by visual inspection.

The dissertation explores the diffraction tomographic imaging of a target object using ultra-wideband (UWB) white Gaussian noise (WGN) waveforms in radar system. The principles and validation of UWB noise radar system for tomography application are presented including the theoretical analysis, numerical simulations and experimental results.

Using WGN waveform as the transmit signal ensures the low probability of intercept (LPI) since the transmitted noise waveform is constantly varying and never repeats exactly. Ideally, such a signal is a stochastic process with a flat spectral density over a wide frequency range; however, the spectral density of WGN cannot be uniform and consistent for all frequencies in reality. In order to obtain a flat spectral density over the desired frequency range, a method of averaging multiple independent and identically distributed (iid) noise waveforms is proposed. From the simulation results, tomographic images of various target scenarios are successfully reconstructed with random noise waveforms.

In addition, the hardware system of bistatic UWB noise radar for tomographic imaging application is designed and implemented. The tomographic image processing technique for large sets of collected data samples are also proposed. Both metallic and dielectric target objects are correctly imaged based on measured scattering data, and the experimental results compare well with the numerical simulation results.

## TABLE OF CONTENTS

List of Figures .....	vi
List of Tables .....	xii
Acknowledgements.....	xiii
Chapter 1 Introduction .....	1
1.1 Motivation and Background.....	1
1.2 Contributions of the Dissertation .....	2
1.3 Overview.....	3
1.3 References.....	4
Chapter 2 Diffraction Tomography using UWB Random Noise Waveforms .....	6
2.1 Overview.....	6
2.2 Analysis of White Gaussian Noise Model .....	8
2.3 Formulation of the Scattering Properties for Cylindrical PEC Object.....	10
2.4 Numerical Simulation Results.....	15
2.4.1 Diffraction tomography with a single transmitted WGN waveform for a single scattering object .....	15
2.4.2 Diffraction tomography with multiple transmitted iid WGN waveforms for a single scattering object.....	19
2.4.3 Diffraction tomography with multiple transmitted iid WGN waveforms for two symmetrically distributed scattering objects.....	21
2.4.4 Diffraction tomography with multiple transmitted iid WGN waveforms for two randomly distributed scattering objects .....	24
2.4.5 Diffraction tomography with multiple transmitted iid WGN waveforms for three randomly distributed scattering objects in different sizes.....	25
2.5 Image Quality Measure .....	27
2.5.1 Reference image generation .....	28
2.5.2 Pixel difference-based measure.....	31
2.5.3 Signal-to-noise ratio effects on image quality.....	33
2.6 Summary .....	39
2.7 References.....	40
Chapter 3 Principle and Simulations of UWB Noise Radar Tomographic System .....	46
3.1 Overview .....	46
3.2 Formulation of the Scattering Properties .....	47
3.3 Numerical Simulation Results.....	52
3.3.1 Image quality measure .....	52
3.3.2 Multiple transmitted iid WGN waveforms and rotational angle .....	56
3.3.3 Tomographic image with multiple transmitted iid WGN waveforms for a circular PEC cylinder .....	58
3.3.4 Tomographic image with multiple transmitted iid WGN waveforms for a square PEC box .....	60

3.3.5 Tomographic image with multiple transmitted iid WGN waveforms for an equilateral triangular PEC prism .....	62
3.3.6 Tomographic image with multiple transmitted iid WGN waveforms for a circular dielectric cylinder.....	64
3.3.7 Tomographic image with multiple transmitted iid WGN waveforms for a square dielectric box.....	66
3.4 Summary .....	67
3.5 References.....	68
 Chapter 4 Design and Implementation of UWB Noise Radar Tomographic System.....	71
4.1 Overview .....	71
4.2 Implementation of the Hardware System.....	72
4.2.1 Experimental configuration of UWB noise radar.....	72
4.2.2 Transmitter and receiver.....	74
4.2.3 Turntable and linear scanner .....	75
4.2.4 Data acquisition and image processing .....	77
4.3 Experimental Results .....	80
4.2.1 Tomographic image for a circular metallic cylinder .....	80
4.2.2 Tomographic image for a square metallic box .....	82
4.2.3 Tomographic image for an equilateral triangular metallic prism .....	84
4.2.4 Tomographic image for a circular concrete cylinder .....	86
4.2.5 Tomographic Image for a square concrete block .....	88
4.4 Summary .....	90
4.5 References.....	91
 Chapter 5 Conclusions and Future Work.....	93
5.1 Conclusions.....	93
5.2 Suggestions for Future Work .....	94
5.2.1 UWB noise radar tomography for X-band .....	94
5.2.2 Moving average filter for noise suppression .....	95
5.2.3 Background subtraction method for image enhancement .....	98
5.3 References.....	99

## LIST OF FIGURES

Figure 2-1.	The Fourier diffraction theorem relates the Fourier transform of a diffracted projection to the Fourier transform of the object along a semicircular arc. An arbitrary object is illuminated by a plane wave propagating along the unit vector, and the coordinate system is rotated. ....	11
Figure 2-2.	Two-dimensional backward scattering geometry for a cylindrical conducting object. Red dots and green circle represent a linear receiving array and the PEC cylinder, respectively. ....	12
Figure 2-3.	Two-dimensional backward scattering simulation geometry for a cylindrical conducting object. A single PEC cylinder with a radius of 15 cm is located at (0 cm, 0 cm), and a linear receiving array is located 90 cm away from the origin in $-x$ direction. ....	16
Figure 2-4.	(a) The first UWB WGN waveform generated with 500 amplitude samples ( $l=500$ ) drawn from $N(0, \sigma^2)$ . Pulse duration is 2.4 ns. (b) The frequency spectrum after 8–10 GHz bandpass filtering operation. The frequency ranges are shown from DC to 12 GHz only. ....	17
Figure 2-5.	(a) The second UWB WGN waveform generated with 500 amplitude samples ( $l=500$ ) drawn from $N(0, \sigma^2)$ . Pulse duration is 2.4 ns. (b) The frequency spectrum after 8–10 GHz bandpass filtering operation. The frequency ranges are shown from DC to 12 GHz only. ....	17
Figure 2-6.	The image reconstruction method using diffraction tomography. ....	18
Figure 2-7.	(a) The normalized magnitude of Fourier space data of the single cylindrical conducting object, and (b) the normalized tomographic image using the first UWB WGN waveform shown in Figure 2-4(a). ....	18
Figure 2-8.	(a) The normalized magnitude of Fourier space data of the single cylindrical conducting object, and (b) the normalized tomographic image using the first UWB WGN waveform shown in Figure 2-5(a). ....	19
Figure 2-9.	The image reconstruction method with $K$ multiple iid WGN transmitted waveforms using diffraction tomography. ....	20
Figure 2-10.	The final tomographic image of a single PEC cylinder located at (0,0) after summing and averaging process with the (a) one transmitted WGN waveform image, (b) three transmitted WGN waveform images, (c) seven transmitted WGN waveform images, and (d) all ten transmitted WGN waveform images. The colorbar indicates the normalized magnitude of scattering object function, $\sigma(x, y)$ . ....	21
Figure 2-11.	Two-dimensional backward scattering simulation geometry for two symmetrically distributed cylindrical conducting objects. Two PEC cylinders with radii of 15 cm are located at (0 cm, -40 cm) and (0 cm, 40 cm), and a linear receiving array is located 90 cm away from the origin in $-x$ direction. ....	22

Figure 2-12. The final tomographic image of two symmetrically distributed PEC cylinders located at (0 cm, -40 cm) and (0 cm, 40 cm) after summing and averaging process with the (a) one transmitted WGN waveform image, (b) three transmitted WGN waveform images, (c) seven transmitted WGN waveform images, and (d) all ten transmitted WGN waveform images.....	23
Figure 2-13. Two-dimensional backward scattering simulation geometry for two randomly distributed cylindrical conducting objects. PEC cylinders with radii of 15 cm are located at (-7.5 cm, 22.5 cm) and (35 cm, -55 cm).....	24
Figure 2-14. The final tomographic image of two randomly distributed PEC cylinders located at (-7.5 cm, 22.5 cm) and (35 cm, -55 cm) after summing and averaging process with the (a) one transmitted WGN waveform image, (b) three transmitted WGN waveform images, (c) seven transmitted WGN waveform images, and (d) all ten transmitted WGN waveform images.....	25
Figure 2-15. Two-dimensional backward scattering simulation geometry for three randomly distributed cylindrical conducting objects in different sizes. Three PEC cylinders with radii of 7.5 cm, 10 cm, and 15 cm are located at (-22.5 cm, -20 cm), (10 cm, 50 cm), and (25 cm, -40 cm), respectively. ....	26
Figure 2-16. The final tomographic image of three randomly distributed PEC cylinders in different sizes after summing and averaging process with the (a) one transmitted WGN waveform image, (b) three transmitted WGN waveform images, (c) seven transmitted WGN waveform images, and (d) all ten transmitted WGN waveform images. ....	27
Figure 2-17. (a) The first derivative Gaussian input waveform with a pulse width of 0.1 ns. (b) The frequency spectrum of the first derivative Gaussian input waveform shown in Figure 2-17(a). The frequency spectrum ranges are displayed from DC to 12 GHz only. ....	29
Figure 2-18. (a) The normalized magnitude of Fourier space data based on the transmission of the first derivative Gaussian waveform shown in Figure 2-17(a) for the single cylindrical PEC object shown in Figure 2-3. (b) The tomographic image of the single cylindrical conducting object located at (0 cm, 0 cm). The colorbar indicates the normalized magnitude of scattering object function, $o(x, y)$ . ....	29
Figure 2-19. (a) The magnitude of Fourier space data based on the transmission of the first derivative Gaussian waveform shown in Figure 2-17(a) for two symmetrically distributed cylindrical PEC objects shown in Figure 2-11. (b) The tomographic image of two symmetrically distributed cylindrical conducting objects located at (0 cm, -40 cm) and (0 cm, 40 cm).....	30
Figure 2-20. (a) The magnitude of Fourier space data based on the transmission of the first derivative Gaussian waveform shown in Figure 2-17(a) for two randomly distributed cylindrical PEC objects shown in Figure 2-13. (b) The tomographic image of two randomly distributed cylindrical conducting objects located at (-7.5 cm, 22.5 cm) and (35 cm, -55 cm). ....	30

Figure 2-21. (a) The magnitude of Fourier space data based on the transmission of the first derivative Gaussian waveform shown in Figure 2-17(a) for three randomly distributed cylindrical PEC objects in different sizes shown in Figure 2-15. (b) The tomographic image of three randomly distributed cylindrical conducting objects in different sizes located at (-22.5 cm, -20 cm), (10 cm, 50 cm), and (25 cm, -40 cm). ....	31
Figure 2-22. MSE versus number of reconstructed images after normalization. MSE decreases as the number of reconstructed images is overlapped.....	32
Figure 2-23. MSE versus number of reconstructed images after normalization with 4 different SNR values for (a) single cylindrical PEC object, (b) two symmetrically distributed cylindrical PEC objects, (c) two randomly distributed cylindrical PEC objects, and (d) three randomly distributed cylindrical PEC objects in different sizes. For all cases, MSE decreases as the number of reconstructed images is overlapped regardless of SNRs.....	34
Figure 2-24. The final tomographic images after summing and averaging process with the 10 iid noise waveforms with various SNRs for a single PEC cylinder: (a) SNR = -20 dB, (b) SNR = -10 dB, (c) SNR = 0 dB, and (d) SNR = +10 dB.....	35
Figure 2-25. The final tomographic images after summing and averaging process with the 10 iid noise waveforms with various SNRs for two symmetrically distributed PEC cylinders: (a) SNR = -20 dB, (b) SNR = -10 dB, (c) SNR = 0 dB, and (d) SNR = +10 dB.....	36
Figure 2-26. The final tomographic images after summing and averaging process with the 10 iid noise waveforms with various SNRs for two randomly distributed PEC cylinders: (a) SNR = -20 dB, (b) SNR = -10 dB, (c) SNR = 0 dB, and (d) SNR = +10 dB.....	37
Figure 2-27. The final tomographic images after summing and averaging process with the 10 iid noise waveforms with various SNRs for three randomly distributed PEC cylinders in different sizes: (a) SNR = -20 dB, (b) SNR = -10 dB, (c) SNR = 0 dB, and (d) SNR = +10 dB. ....	38
Figure 2-28. MSE versus SNR values for all final tomographic images shown in Figure 2-24(d) through Figure 2-27(d). MSE decreases as the level of SNR increases.....	39
Figure 3-1. Two-dimensional backward scattering geometry for a cylindrical object. Red dots and green circle represent a linear receiving array and the target object, respectively. ....	48
Figure 3-2. The image reconstruction method with $K$ multiple iid WGN transmitted waveforms for a sequentially rotated object using diffraction tomography.....	51
Figure 3-3. Two-dimensional backward scattering simulation geometry for a cylindrical conducting object. The PEC cylinder with a radius of 8 cm is located at (0 cm, 0 cm), and a linear receiving array is located 68 cm away from the center of the object... ..	52

Figure 3-4. (a) The first derivative Gaussian input waveform with a pulse width of 0.225 ns. (b) The frequency spectrum of the first derivative Gaussian input waveform shown in Figure 3-4(a). The frequency spectrum range is displayed from DC to 8 GHz only .....	54
Figure 3-5. The reference tomographic image of the circular PEC cylinder shown in Figure 3-3 for $\theta = 1.8^\circ$ . ....	54
Figure 3-6. Tomographic images of the circular PEC cylinder with 6 different rotational angles: (a) $\theta = 3.6^\circ$ , (b) $\theta = 9^\circ$ , (c) $\theta = 18^\circ$ , (d) $\theta = 36^\circ$ , (e) $\theta = 45^\circ$ , and (f) $\theta = 54^\circ$ . ....	55
Figure 3-7. MSE vs. rotational angle for the circular PEC cylinder simulation. MSE increases as the value of the rotational angle $\theta$ increases.....	56
Figure 3-8. Two-dimensional backward scattering simulation geometry for a circular PEC cylinder. The cylinder with a radius of 10 cm is located at (0 cm, 0 cm), and a linear receiving array is located 68 cm away from the center of the object.....	58
Figure 3-9. Two-dimensional tomographic image of a single PEC cylinder with a radius of 10 cm located at (0 cm, 0 cm) after summing and averaging process based on (a) one transmitted WGN waveform, (b) three transmitted WGN waveforms, (c) seven transmitted WGN waveforms, and (d) all ten transmitted WGN waveforms. The rotational angle is $9^\circ$ .....	59
Figure 3-10. Two-dimensional backward scattering simulation geometry for a square PEC box with a length of 20 cm. The box is located at (0 cm, 0 cm), and a linear receiving array is located 68 cm away from the center of the object.....	60
Figure 3-11. Two-dimensional tomographic image of a square PEC box with a length of 20 cm located at (0 cm, 0 cm) after summing and averaging process based on (a) one transmitted WGN waveform, (b) three transmitted WGN waveforms, (c) seven transmitted WGN waveforms, and (d) all ten transmitted WGN waveforms. The rotational angle is $9^\circ$ .....	61
Figure 3-12. Two-dimensional backward scattering simulation geometry for an equilateral triangular PEC prism with a length of 20 cm. The prism is located at (0 cm, 0 cm), and a linear receiving array is located 68 cm away from the center of the object.....	62
Figure 3-13. Two-dimensional tomographic image of an equilateral triangular PEC prism with a length of 20 cm located at (0 cm, 0 cm) after summing and averaging process based on (a) one transmitted WGN waveform, (b) three transmitted WGN waveforms, (c) seven transmitted WGN waveforms, and (d) all ten transmitted WGN waveforms. The rotational angle is $9^\circ$ .....	63
Figure 3-14. Two-dimensional backward scattering simulation geometry for a circular dielectric cylinder with a radius of 8 cm. The cylinder is located at (0 cm, 0 cm), and a linear receiving array is located 68 cm away from the center of the object .....	64

Figure 3-15. Two-dimensional tomographic image of a single circular dielectric cylinder with a radius of 8 cm located at (0 cm, 0 cm) after summing and averaging process based on (a) one transmitted WGN waveform, (b) three transmitted WGN waveforms, (c) seven transmitted WGN waveforms, and (d) all ten transmitted WGN waveforms. The rotational angle is 9°.....	65
Figure 3-16. Two-dimensional backward scattering simulation geometry for a square dielectric box with a length of 20 cm is located at (0 cm, 0 cm), and a linear receiving array is located 68 cm away from the center of the object.....	66
Figure 3-17. Two-dimensional tomographic image of a square dielectric box with a length of 20 cm located at (0 cm, 0 cm) after summing and averaging process based on (a) one transmitted WGN waveform, (b) three transmitted WGN waveforms, (c) seven transmitted WGN waveforms, and (d) all ten transmitted WGN waveforms. The rotational angle is 9°.....	67
Figure 4-1. Automated UWB noise radar tomographic system.....	73
Figure 4-2. Block diagram of transmitter and receiver.....	74
Figure 4-3. The gain vs. frequency plot of Mini-circuit ZVE-8G+.....	75
Figure 4-4. A metal cylinder placed on the turntable. Also shown are the transmitting and receiving antenna and microwave absorber behind the target to minimize reflections from the back.....	78
Figure 4-5. (a) The measured scattering data when both Tx and Rx are located at the center of the cylinder, and (b) the frequency spectrum of the measured data. The frequency spectrum ranges are shown from DC to 8 GHz only. ....	79
Figure 4-6. (a) The first segment of the measured scattering data shown in Figure 4-5(a), and (b) the frequency spectrum from DC to 8 GHz only.....	80
Figure 4-7. Top and side view of experiment configuration for a circular metallic cylinder. The cylinder is placed on the turntable for rotation. Also the microwave absorber behind the target is shown to minimize reflections from the back.....	81
Figure 4-8. The metallic cylinder used for the experiment. The dimensions of the cylinder are measured in inches.....	81
Figure 4-9. The final tomographic image of the metallic cylinder based on the measured data.....	82
Figure 4-10. Top and side view of experiment configuration for a square metallic box. The box is placed on the turntable for rotation. Also the microwave absorber behind the target is shown to minimize reflections from the back. ....	83
Figure 4-11. The metallic box used for the experiment. The dimensions of the box are measured in inches.....	83

Figure 4-12. The final tomographic image of the metallic box based on the measured data.....	84
Figure 4-13. Top and side view of experiment configuration for an equilateral triangular metallic prism. The prism is placed on the turntable for rotation. Also the microwave absorber behind the target is shown to minimize reflections from the back.....	85
Figure 4-14. The metallic prism used for the experiment. The dimensions of the prism are measured in inches.....	85
Figure 4-15. The final tomographic image of the metallic prism based on the measured data.....	86
Figure 4-16. Top and side view of experiment configuration for a circular concrete cylinder. The cylinder is placed on the turntable for rotation. Also the microwave absorber behind the target is shown to minimize reflections from the back.....	87
Figure 4-17. The concrete cylinder used for the experiment. The dimensions of the cylinder are measured in inches.....	87
Figure 4-18. The final tomographic image of the concrete cylinder based on the measured data.....	88
Figure 4-19. Top and side view of experiment configuration for a square concrete block. The box is placed on the turntable for rotation. Also the microwave absorber behind the target is shown to minimize reflections from the back.....	89
Figure 4-20. The concrete block used for the experiment. The dimensions of the concrete block are measured in inches.....	89
Figure 4-21. The final tomographic image of the concrete block based on the measured data.....	90
Figure 5-1. The proposed design of transmitter and receiver for X-band operation.....	95
Figure 5-2. Top and side view of experiment configuration for a circular metallic cylinder. The cylinder is not rotated. Also the microwave absorber behind the target is shown to minimize reflections from the back.....	96
Figure 5-3. Frequency responses of the collected scattering data with (a) 1-pt (no MAF), (b) 3-pt, (c) 5-pt, and (d) 7-pt MAF applied. ....	97
Figure 5-4. Tomographic images based on measured scattering data when (a) no MAF, (b) 3-pt MAF, (c) 5-pt MAF, and (d) 7-pt MAF applied. ....	98
Figure 5-5. Tomographic images based on measured scattering data when (a) no background subtraction, and (b) background subtraction is implemented.....	99

**LIST OF TABLES**

Table 3-1. Target objects imaged by the numerical simulations. ....	57
Table 4-1. Target objects imaged by the tomographic noise radar system. ....	76

## **ACKNOWLEDGEMENTS**

I would like to show my sincere appreciation for the many individuals, both friends and collaborators, who have provided me with support and knowledge. First, I would like to thank my advisor Dr. Ram M. Narayanan for his guidance, advice and support throughout my career as a graduate student. My thanks also go out to my thesis committee members Professors Kenneth Jenkins, Douglas Werner, and Karl Reichard for their valuable comments. In addition, I would like to thank Dr. Muralidhar Rangaswamy of the US Air Force Research Laboratory (AFRL) for providing assistance in all aspects of the research. The support of the US Air Force Office of Scientific Research (AFOSR) through Grant # FA9550-12-1-0164 is gratefully acknowledged. Finally, I would like to thank my family, especially Yunyoung and Daniel, for supporting my decision to pursue a Ph.D. and then backing me up with encouragement to continue at times when I became frustrating. Without all the moral support of you and countless others, it would have been impossible for me to accomplish this lofty goal. Gloria in Excelsis Deo.

# Chapter 1

## Introduction

### 1.1 Motivation and Background

Advances in signal and imaging processing techniques of radar systems have progressed so that multi-dimensional representations of the target object can be obtained from electromagnetic (EM) scattering. One such imaging technique is tomography [1]. The fundamental idea of tomography is to solve an inverse scattering problem governed by wave equations [2]. While prominently found in the medical and industrial scanning areas, tomography has more recently found applications in radar systems. For example, tomography has proven to be a vital technique for the imaging of target objects via microwave interaction with ground penetrating radar (GPR) [3].

In radar imaging systems, images of a target are reconstructed based on range profiles of the distributed sensor elements. When a transmitter radiates a waveform, spatially distributed receivers collect samples of the scattered field due to the material properties of the target. In the next iteration, a different transmitter is activated, and the scattered field collecting process is repeated. Finally all collected scattered field data is relayed for signal processing and subsequent imaging. The optimal waveform and bandwidth enhance the performance of the radar system [4].

While most prior research has been accomplished using coherent electromagnetic waves in the microwave and millimeter-wave regimes, random field cross-correlation is a new promising technique which bypasses shortcomings of usual active methods. While coherent source environments can generate anomalies in the correlation function, random uniformly distributed sources can cause such ghosts in the image to disappear. The idea is to use time

correlations of noise for recovering the Green's function and from it, the impulse response. In the case of a completely random waveform, the cross-correlation of signals recorded between two points converges to the complete Green's function of the medium, including all reflection, scattering and propagation modes. Using an array of probes located around the region to be imaged, the detected noise correlation can be shown to be a function of the spatial overlap of the electromagnetic fields at the probes and the spatial distribution of the dielectric constant and/or conductivity of the sample. A three-dimensional conductivity map has been successfully generated using passive thermal noise emissions to image breast tumors and buried isolated scatterers [5].

In this dissertation, the main research is focused on tomographic imaging for UWB noise radar, which is considered as a promising technique for high-resolution imaging without alerting the presence of the radar system. Theoretical analysis, numerical simulations and practical hardware implementation of UWB noise radar tomography are presented in detail.

## **1.2 Contributions of the Dissertation**

The research that I have performed during my Ph.D. studies at the Pennsylvania State University has led to several developments in the field of UWB noise radar tomography.

- White Gaussian noise waveform modeling and the practical implementation of bandlimited UWB noise waveforms for tomographic imaging application are proposed. More specifically, multiple transmissions of independent and identically distributed (iid) WGN noise waveforms are suggested to bypass the shortcomings of using UWB random noise waveform.

- The principle of tomography based noise radar imaging is proposed. The tomographic image of the target object is successfully reconstructed using the Fourier diffraction theorem.
- Numerical simulations are performed to validate the theory of Fourier diffraction for various target scenarios. More specifically, multiple cylindrical targets in different sizes are correctly imaged with a linearly positioned receiver array under various SNR settings.
- The image quality of the reconstructed tomographic images is quantitatively analyzed. Furthermore, the image quality measure for various SNR settings can be used as a guideline for the practical implementation of UWB noise radar system for tomographic imaging applications.
- Theoretical analysis of noise radar tomography is proposed for sequentially rotated target objects. The numerical simulations of a bistatic imaging radar system are performed to obtain the complete cross-sectional images of various shaped target objects.
- Hardware implementation of UWB noise radar system for tomography application is proposed. The reconstructed tomographic images based on experimental results can be compared with those obtained based on numerical simulation results, showing a good agreement between simulation and experiment results for both metallic and dielectric target object cases.

### 1.3 Overview

Chapter 2 presents the theoretical foundations of diffraction tomography using a white Gaussian noise (WGN) waveform as a transmitted signal for the cross-section images of multiple

metallic target objects inside a rectangular geometry for the region of interest. The empirical solution to bypass the shortcomings of using UWB random noise waveform and the image quality measures of the reconstructed images under various SNR environments are discussed as well.

Chapter 3 focuses on the principle and numerical simulation results of tomographic imaging of various target scenarios using UWB noise radar. Theoretical analysis of the image reconstruction for a bistatic imaging radar system with a two-dimensional rotating cylinder using the Fourier diffraction theorem under the assumption of plane wave illumination is presented. Also, the numerical simulation results of diffraction tomography for UWB noise radar are presented.

Chapter 4 shows the hardware implementation and experimental investigation of UWB noise radar. Design considerations and performance for UWB noise radar using WGN waveforms are presented. The effective tomographic image processing technique for large sets of collected data samples is proposed as well. The reconstructed tomographic images based on experiments can be compared with those obtained based on numerical simulation results for various target objects.

Chapter 5 discusses about conclusions and suggestions for future research work regarding UWB noise radar tomography.

### 1.3 References

- [1] H. D. Griffiths, and C. J. Baker, "Fundamentals of tomography and radar," *Advances in Sensing With Security Applications*, vol. 2, pp. 171-187, 2006.
- [2] A. C. Kak, "Computerized Tomography with X-Ray, Emission, and Ultrasound Sources," *Proceedings of the IEEE*, vol. 67, pp. 1245-1272, 1979.

- [3] N. C. Wicks, "RF Tomography with application to ground penetrating radar," *Conference Record of the Forty-First Asilomar Conference on Signals, Systems & Computers*, pp. 2017-2022, 2007.
- [4] M. R. Bell, "Information-Theory and Radar Wave-Form Design," *IEEE Transactions on Information Theory*, vol. 39, pp. 1578-1597, 1993.
- [5] S. Reza, G. Bosman, G. R. Duensing et al., "Image guided noise tomography for increased specificity of magnetic resonance imaging," *Fluctuations and Noise in Biological, Biophysical, and Biomedical Systems III*, vol. 5841, pp. 125-132, 2005.

## Chapter 2

### Diffraction Tomography using UWB Random Noise Waveforms

#### 2.1 Overview

Research on the use of random or pseudorandom noise transmit signals in radar has been conducted since the 1950s [1, 2]. Noise radar has been considered a promising technique for the covert identification of target objects due to several advantages, such as excellent electronic countermeasure (ECM), low probability of detection (LPD), low probability of interception (LPI) features, and relatively simple hardware architectures [3-5]. Also, advances in signal and imaging processing techniques in radar systems have progressed so that multidimensional representations of the target object can be obtained [6].

In general, radar imaging tends to be formulated in the time domain to exploit efficient back-projection algorithms, generate accurate shape features of the target object, and provide location data [7]. For multistatic radar systems, the images of a target are reconstructed based on range profiles obtained from the distributed sensor elements. When a transmitter radiates a waveform, spatially distributed receivers collect samples of the scattered field which are related to the electrical parameters of the target object. For the next iteration, a different transmitter is activated, and the scattered field collection process is repeated. Finally, all collected scattered field data are relayed for signal processing and subsequent image formation algorithms.

Tomography-based radar imaging algorithms have been developed based on the microwave image reconstruction method [9], characterizing the material property profiles of the target object in the frequency domain and reconstructing specific scattering features inside the interrogation medium by solving the inverse scattering problem. The capability of microwave

imaging techniques has been found attractive in malignant breast cancer detection [10-13], civil infrastructure assessment [14-16], and homeland security [17-19]. The quality of the reconstructed image for different values of the electrical contrast for a UWB imaging system was investigated and published for both low-contrast and high-contrast object cases. For low-contrast objects, the obtained target image using a single frequency achieves a good reconstruction of the electrical contrast that is almost equivalent to the one obtained with the entire UWB frequency range. For the high-contrast case, while the formation of a Moiré pattern affects the single frequency reconstruction, this artifact does not appear in the UWB frequency image [20]. Thus, UWB radar tomography is expected to provide advantages over the single or narrow band frequency operation in terms of resolution and accuracy for any target object.

This chapter is organized as follows. First, the characteristics of UWB random noise signal and the shortcomings of using such noise signal as a radar transmit waveform in tomographic image reconstruction process are discussed in section 2.2. The empirical solution to bypass the shortcoming of using UWB random noise waveform is also proposed. In section 2.3, the formulations of the image reconstruction of two-dimensional scattering geometry using the Fourier diffraction theorem under the assumption of plane wave illumination is presented. The numerical simulation results of diffraction tomography imaging for various arrangements of circular PEC cylindrical objects are presented in section 2.4. The image quality measures of the reconstructed images and SNR effects for multiple transmissions of UWB random noise waveforms are discussed in section 2.5. Conclusions are presented in section 2.6.

## 2.2 Analysis of White Gaussian Noise Model

The main advantage of transmitting a random noise waveform is to covertly detect and image a target without alerting others about the presence of the radar system. Such LPI characteristics of the noise radar are guaranteed because the transmitted random noise waveform is constantly varying and never repeats itself exactly [20]. The random noise waveform can be experimentally generated simply by amplifying the thermal noise generated in resistors or noise diodes while maintaining relatively flat spectral density versus frequency [21]. Hence, relatively simple hardware designs can be achieved for noise radars compared to the conventional radar systems using complicated signal modulation schemes.

For a random noise waveform model, let  $x[n]$  be a discrete time WSS and ergodic random process and a sequence of independent and identically distributed (iid) random variable drawn from a Gaussian distribution,  $N(0, \sigma^2)$ .  $x[n]$  defined herein as white Gaussian noise, that is, its probability density function follows a Gaussian distribution and its power spectral density is ideally a non-zero constant for all frequencies. However, the finite number of random noise amplitude samples must be chosen for waveform generation for any numerical simulations and practical experiments.

Assume that a sequence of only  $l$  samples of  $x[n]$  is selected for generating a white Gaussian noise. In this case, the estimate for the power spectral density,  $\hat{S}_l(\omega)$ , is given by [22]

$$I_l(\omega) = \hat{S}_l(\omega) = \sum_{m=-(l-1)}^{l-1} \hat{r}_l[m] e^{-j\omega m} \quad (2.1)$$

where  $\hat{r}_l[m]$  is the estimate for the autocorrelation sequence.  $I_l(\omega)$  is defined as the periodogram estimate, and the rigorous analysis of the expected value and variance of the periodogram estimate for any arbitrary  $\omega$  is described in [22-24]. The expected value of the periodogram estimate is [22, 23]

$$\begin{aligned} \mathbb{E}[I_l(\omega)] &= \sum_{m=-(l-1)}^{l-1} \mathbb{E}[\hat{r}_l[m]] e^{-j\omega m} \\ &= \sum_{m=-(l-1)}^{l-1} \left(1 - \frac{|m|}{l}\right) r_l[m] e^{-j\omega m}, \end{aligned} \quad (2.2)$$

which suggests that  $I_l(\omega)$  is a biased estimator. However, it is considered to be asymptotically unbiased as  $l$  approaches infinity. In this case, the expected value of  $I_l(\omega)$  becomes a constant such that

$$\mathbb{E}[I_l(\omega)] \square S_x(\omega) = \sigma_x^2 \text{ as } l \rightarrow \infty. \quad (2.3)$$

The variance of the periodogram estimate of the white Gaussian noise waveform formed by a sequence of  $l$  samples is given by [22, 23]

$$\text{VAR}[I_l(\omega)] = S_x(\omega)^2 \left(1 + \left(\frac{\sin(\omega l)}{l \sin(\omega)}\right)^2\right) \quad (2.4)$$

which is proportional to the square of the power spectrum density and does not approach zero as  $l$  increases. In order to decrease the variance of  $I_l(\omega)$ , the periodogram averaging method has been proposed by Bartlett [25]. The average of  $K$  independent and identically distributed periodograms on samples of size  $l$  is given by

$$\bar{I}_{l,K}(\omega) = \frac{1}{K} \sum_{i=0}^{K-1} I_{l,i}(\omega), \quad (2.5)$$

and the expected value of the average with  $K$  iid periodogram estimate is written as [22]

$$\begin{aligned} \mathbb{E}[\bar{I}_{l,K}(\omega)] &= \mathbb{E}[I_l(\omega)] \\ &= \sum_{m=-(l-1)}^{l-1} \left(1 - \frac{|m|}{l}\right) r_l[m] e^{-j\omega m}, \end{aligned} \quad (2.6)$$

which is considered to be asymptotically unbiased as  $l$  approaches infinity. Also the variance of the averaged periodogram estimate is given by [22]

$$\begin{aligned} \text{VAR}[\bar{I}_{l,K}(\omega)] &= \frac{1}{K} \text{VAR}[I_l(\omega)] \\ &\square \frac{1}{K} S_x(\omega)^2. \end{aligned} \quad (2.7)$$

The variance of the averaged periodogram estimate is inversely proportional to the number of iid periodograms  $K$ , and consequently the variance approaches zero as  $K$  approaches infinity. Equations (2.6) and (2.7) are used to conclude that the expected value remains unchanged, but only the variance of white Gaussian noise decreases for averaging  $K$  iid periodogram estimates. Increasing the number of  $K$  in averaging periodogram estimate truly flattens the spectral density, and the successful tomographic image can be achieved by transmitting  $K$  multiple random noise waveforms with a large sequence size  $l$ . For the numerical simulations performed in this chapter, a total of 10 iid random noise waveforms are transmitted, and each iid noise waveform is generated with 500 random amplitude samples drawn from  $N(0, \sigma^2)$ . The tomographic image is formed based on the dataset from 41 discrete frequencies chosen uniformly within X-band from 8 GHz to 10 GHz in steps of 50 MHz.

### 2.3 Formulation of the Scattering Properties for Cylindrical PEC Object

In this section, the scattering properties for two-dimensional cylindrical impenetrable conducting object in the bistatic scattering arrangement are discussed, and the Fourier diffraction tomography algorithm is applied to reconstruct the image of the object based on the bistatic scattering properties. The Fourier diffraction theorem has been extensively applied in the area of acoustical imaging [26-28]. The goal of diffraction tomography is to reconstruct the properties of a slice of an object from the scattered field. For planar geometry, an object is illuminated with a plane wave, and the scattered fields are calculated or measured over a straight line parallel to the incident plane wave. The mathematical formulation and proof of validity of the Fourier

diffraction theorem shown in Figure 2-1 are not presented in this section since they were already stated and published [29].

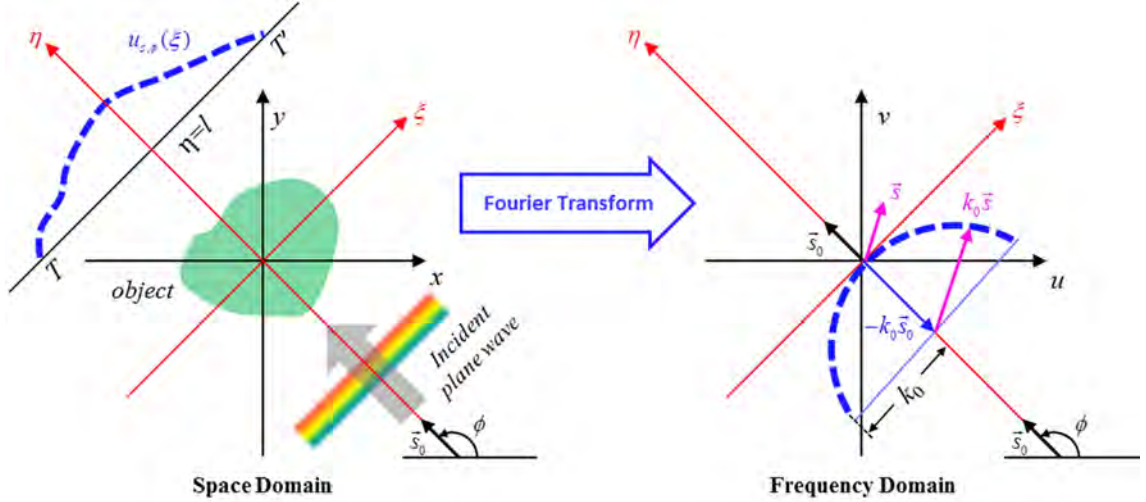


Figure 2-1. The Fourier diffraction theorem relates the Fourier transform of a diffracted projection to the Fourier transform of the object along a semicircular arc. An arbitrary object is illuminated by a plane wave propagating along the unit vector, and the coordinate system is rotated.

Two-dimensional backward scattering geometry for a cylindrical conducting object is shown in Figure 2-2. Prior research on microwave imaging has already proven that the image reconstructed in the backward scattering case is better than that obtained in the forward scattering case, based on numerical results [30].

As shown in Figure 2-2, a single cylindrical perfect electric conductor (PEC) object is located at the center of the simulation scene. The height of the cylindrical object is assumed to be infinitely long along the  $z$ -axis and the incident  $z$ -polarized plane wave is illuminated from  $-x$  direction. The receiver spacing,  $\Delta y$ , is calculated to avoid aliasing effect, and is given by

$$\Delta y \leq \frac{\lambda_{\min}}{2} \quad (2.8)$$

where  $\lambda_{\min}$  is the minimum wavelength. A linear receiving array is located at  $x = -d$  from the center of the cylinder object, collecting scattered field for reconstruction of the object image. The frequency sampling interval,  $\Delta f$ , is also considered to ensure an image that is free of false aliases, and is given by

$$\Delta f \leq \frac{c}{2 \cdot r} \quad (2.9)$$

where  $c$  is the speed of wave propagation in free space, and  $r$  is the radius of the cylindrical PEC object.

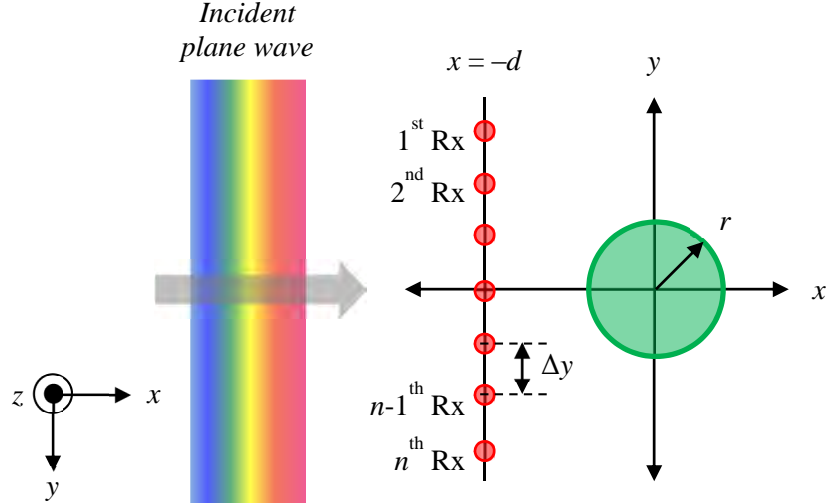


Figure 2-2. Two-dimensional backward scattering geometry for a cylindrical conducting object. Red dots and green circle represent a linear receiving array and the PEC cylinder, respectively.

As shown in the previous section, the frequency response of the transmitted white Gaussian noise waveform shows that the field amplitude is a constant non-zero amplitude value for all possible frequencies. Thus, the  $z$ -polarized incident plane wave of a single transmitted white Gaussian noise waveform for  $N$  discrete frequencies takes the form

$$\begin{aligned} E_{inc}(\vec{r}) &= \hat{z} \cdot \left( E_1 e^{-jk_1 \hat{x} \cdot \vec{r}} + E_2 e^{-jk_2 \hat{x} \cdot \vec{r}} + \dots + E_N e^{-jk_N \hat{x} \cdot \vec{r}} \right) \\ &= \hat{z} \cdot \sum_{n=1}^N E_n e^{-jk_n \hat{x} \cdot \vec{r}}, \end{aligned} \quad (2.10)$$

where  $k_n = \omega_n / c$  is the wavenumber, and  $E_n$  is the field amplitude of the transmitted white Gaussian noise waveform at each discrete frequency of interest. The field amplitude of the noise waveform  $E_n$  becomes the non-zero constant value as the sequence of the noise waveform approaches infinity.

The analysis is started from a single frequency, and the process for  $N$  multiple frequencies are developed by summing up the analysis results for  $N$ . Also the entire analysis must be repeated for  $K$  times when  $K$  multiple iid noise waveforms are transmitted. The  $z$ -polarized incident waveform is defined as

$$\begin{aligned} E_{inc}(\vec{r}) &= \hat{z} \cdot E_n e^{-jk_n \hat{x} \cdot \vec{r}} \\ H_{inc}(\vec{r}) &= -\hat{y} \cdot \frac{1}{\eta} \cdot E_n e^{-jk_n \hat{x} \cdot \vec{r}} \end{aligned} \quad (2.11)$$

where  $\eta = \sqrt{\mu_0 / \epsilon_0}$  is the intrinsic impedance in free space. If the object consists of a material having a certain dielectric constant value, the equivalent electric current distribution,  $J_{eq}$ , is calculated for the scattered field. The object is defined as PEC so that the scattered field observed at the linear receiving array in the  $y$ -direction located at  $x = -d$  is calculated by applying the physical optics approximation, and given by

$$\begin{aligned} E_{scat,single}(k_n, x = -d, y) &= -j\omega\mu_0 \int_S J_{eq} \cdot G(\vec{r} - \vec{r}') d\vec{r}' \\ &= -jk_n \eta \int_S (2\hat{n}(\vec{r}') \times H_{inc}(\vec{r}')) \cdot G(\vec{r} - \vec{r}') d\vec{r}' \end{aligned} \quad (2.12)$$

where  $S$  is the boundary of scatterer,  $\hat{n}(\vec{r}')$  is the outward unit normal vector to  $S$ , and  $G(\vec{r} - \vec{r}')$

is the Green's function for two-dimensional geometry defined as

$$G(\vec{r} - \vec{r}') = -\frac{j}{4} H_0^{(2)}(k_n(\vec{r} - \vec{r}')) \quad (2.13)$$

where  $H_0^{(2)}$  is the zeroth-order Hankel function of the second kind.

Similarly, for the case of discrete scattering objects, the scattered field of  $p$  objects over a linear array in the  $y$ -direction located at  $x = -d$  is expressed as

$$E_{scat,multiple}(k_n, x = -d, y) = \sum_p E_{scat,single}(p). \quad (2.14)$$

On assuming the polarization in the  $z$ -direction, the general form of scattered field,  $u_{scat}$ , obtained by the receivers at  $x = -d$  becomes

$$\begin{aligned} u_{scat}(k_n, x = -d, y) &= \hat{z} \cdot E_{scat}(k_n, x = -d, y) \\ &= -jk_n E_n \iint o_{scat}(\vec{r}') e^{-jk_n \hat{x} \cdot \vec{r}'} G(\vec{r} - \vec{r}') d^2 \vec{r}' \end{aligned} \quad (2.15)$$

where

$$o_{scat,single}(\vec{r}') = -2\hat{n}(\vec{r}') \cdot \hat{x} \delta(S(\vec{r}')) \quad (2.16)$$

is defined as the scattering object function of a single PEC object which is related to the object shape, and  $\delta(S(\vec{r}'))$  is a Dirac delta function defined as

$$\delta(S(\vec{r}')) \begin{cases} = 0 & \text{as } \vec{r}' \in S \\ \neq 0 & \text{elsewhere} \end{cases}. \quad (2.17)$$

Similarly, the scattering function shown in (2.16) for discrete scattering objects can be written as

$$o_{scat,multiple}(\vec{r}') = \sum_p o_{scat,single}(p). \quad (2.18)$$

By using the plane wave expansion of the Green's function [31], the one-dimensional Fourier transform of  $u_{scat}$ , defined in (2.15), in  $y$ -direction can be written as

$$\tilde{U}_{scat}(k_n, x = -d, k_y) = \frac{k_n^2 E_n}{j2\gamma} e^{-j\gamma d} \tilde{o}_{scat}(-\gamma - k_n, k_y) \quad (2.19)$$

where

$$\gamma = \begin{cases} \sqrt{k_n^2 - k_y^2} & \text{as } |k_y| \leq k_n \\ -j\sqrt{k_y^2 - k_n^2} & \text{as } |k_y| > k_n \end{cases}. \quad (2.20)$$

If  $k_x$  is defined as

$$k_x = -\gamma - k_n, \quad (2.21)$$

the Fourier transform of the two-dimensional scattering object function,  $\tilde{O}_{scat}(k_x, k_y)$ , defined in (2.19) is given by

$$\tilde{O}_{scat}(k_x, k_y) = \iint o_{scat}(x, y) e^{-j(k_x x + k_y y)} dx dy. \quad (2.22)$$

In this case, the arguments of  $\tilde{O}_{scat}(k_x, k_y)$  are related by

$$(k_x + k_n)^2 + k_y^2 = k_n^2. \quad (2.23)$$

Equations (2.19) and (2.23) show that as a two-dimensional scattering object is illuminated by a plane wave at the frequency  $\omega_n$ , the one-dimensional Fourier transform of the scattered field yields a semicircle centered at  $(0, -k_n)$  with radius  $k_n$  in the two-dimensional Fourier space, which relates to the Fourier diffraction theorem depicted in Figure 2-1. By using  $N$  number of frequencies, the radius in the two-dimensional Fourier space changes, which enhances the resolution and accuracy of the image. Also the variance of the frequency response is reduced by taking average of the frequency responses of  $K$  multiple transmissions of iid UWB noise waveforms [32, 33].

## 2.4 Numerical Simulation Results

### 2.4.1 Diffraction tomography with a single transmitted WGN waveform for a single scattering object

As shown in Figure 2-3, two-dimensional backward scattering geometry with a single cylindrical conducting object is simulated with two band-limited iid UWB WGN waveforms. The cylindrical PEC object with a radius of 15 cm is located at the origin, and the cylinder is assumed to be infinitely long along the  $z$ -axis. The scattered field is uniformly sampled at

receiving array Rx1 through Rx101 with frequency swept within X-band from 8 GHz to 10 GHz in 41 steps of 50 MHz. The locations of Rx1 and Rx101 are at (-90 cm, -75 cm) and (-90 cm, 75 cm), respectively, and the receiver spacing,  $\Delta y$ , is set to 1.5 cm based on (2.8) when  $f_{\max}$  is 10 GHz. The maximum frequency stepping interval,  $\Delta f$ , is also calculated using (2.9), which yields a value of 1 GHz; however, 50-MHz frequency stepping interval enhances the quality of tomographic image compared to the maximum frequency stepping interval of 1 GHz.

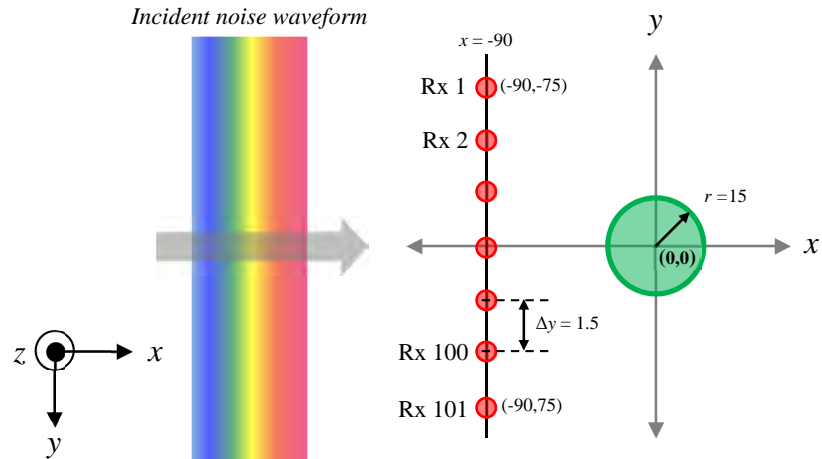


Figure 2-3. Two-dimensional backward scattering simulation geometry for a cylindrical conducting object. A single PEC cylinder with a radius of 15 cm is located at (0 cm, 0 cm), and a linear receiving array is located 90 cm away from the origin in  $-x$  direction.

Figure 2-4(a) and Figure 2-5(a) show the two iid UWB WGN waveforms. Each waveform is generated with 500 random amplitude samples drawn from  $N(0, \sigma^2)$ , and they are transmitted after 8–10 GHz bandpass filtering operation to reconstruct tomographic images of the cylindrical PEC object based on the scattered field observed at Rx1 through Rx101.

A block diagram shown in Figure 2-6 displays the tomographic image reconstruction method using diffraction tomography. The one-dimensional Fourier transformed scattered field data collected at the receiving array Rx1 through Rx101 is Fourier transformed into two-

dimensional object Fourier space data,  $\tilde{O}(k_x, k_y)$ , by using (2.19). Such Fourier space data is two-dimensional inverse Fourier transformed to obtain the scattering object function,  $o(x, y)$ .

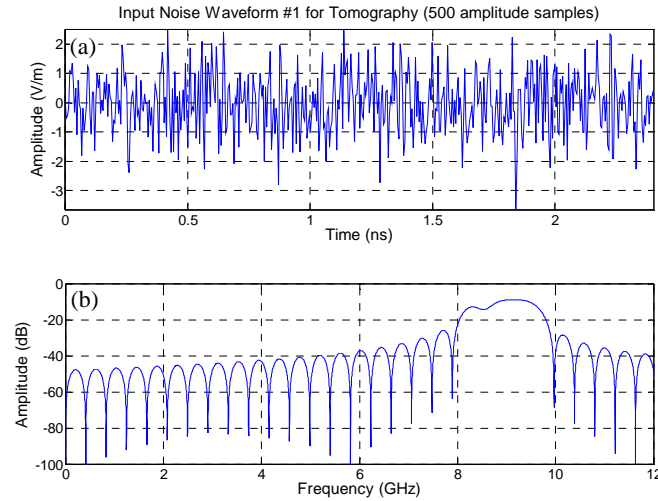


Figure 2-4. (a) The first UWB WGN waveform generated with 500 amplitude samples ( $l=500$ ) drawn from  $N(0, \sigma^2)$ . Pulse duration is 2.4 ns. (b) The frequency spectrum after 8–10 GHz bandpass filtering operation. The frequency ranges are shown from DC to 12 GHz only.

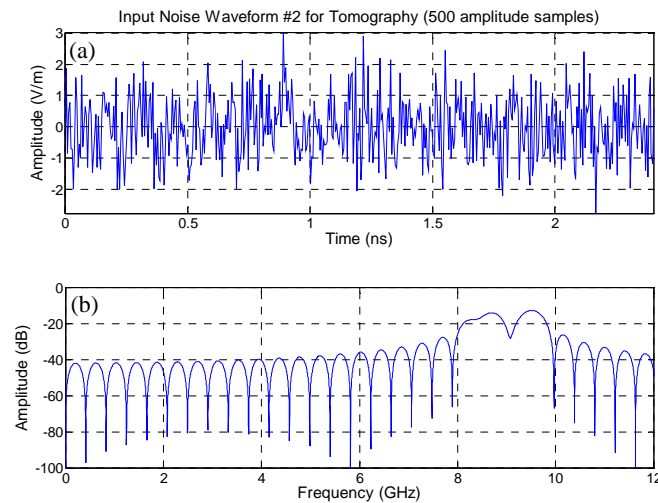


Figure 2-5. (a) The second UWB WGN waveform generated with 500 amplitude samples ( $l=500$ ) drawn from  $N(0, \sigma^2)$ . Pulse duration is 2.4 ns. (b) The frequency spectrum after 8–10 GHz bandpass filtering operation. The frequency ranges are shown from DC to 12 GHz only.

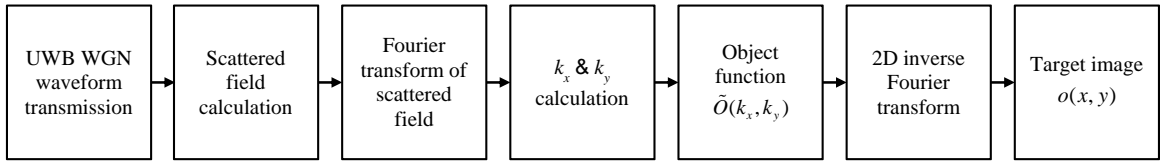


Figure 2-6. The image reconstruction method using diffraction tomography.

Fourier space data and the tomographic images of the single cylindrical conducting object using the first UWB WGN waveform shown in Figure 2-4(a), are calculated and displayed in Figure 2-7(a) and Figure 2-7, respectively. The tomographic image of the single PEC cylinder appears to be successfully reconstructed using the first UWB WGN transmitted waveform.

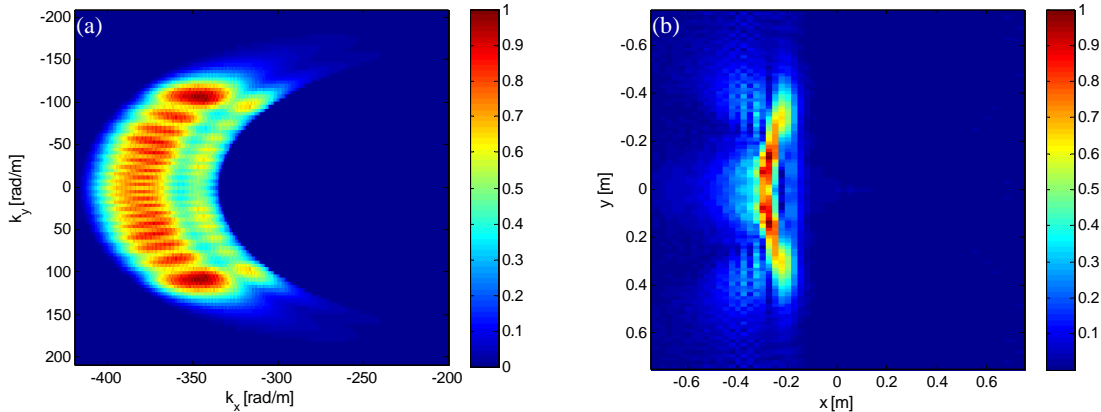


Figure 2-7. (a) The normalized magnitude of Fourier space data of the single cylindrical conducting object, and (b) the normalized tomographic image using the first UWB WGN waveform shown in Figure 2-4(a).

Similarly, both Fourier space data and the tomographic images of the single PEC cylinder using the second UWB WGN waveform shown in Figure 2-5(a) are also shown in Figure 2-8(a) and Figure 2-8(b), respectively. In this case, the tomographic image is significantly affected by the unexpected notch observed in the frequency spectrum at 9.1 GHz in Figure 2-5(b), so that the tomographic image of the object cannot be achieved correctly compared to the previous case

where the first WGN waveform is transmitted. Based on the simulation results with two band-limited iid UWB WGN waveforms, a single transmission of WGN waveform may or may not be sufficient to reconstruct a successful tomographic image of the object with diffraction tomography algorithm due to the undesired and unexpected notches in the spectral density of the practical UWB WGN transmitted waveforms.

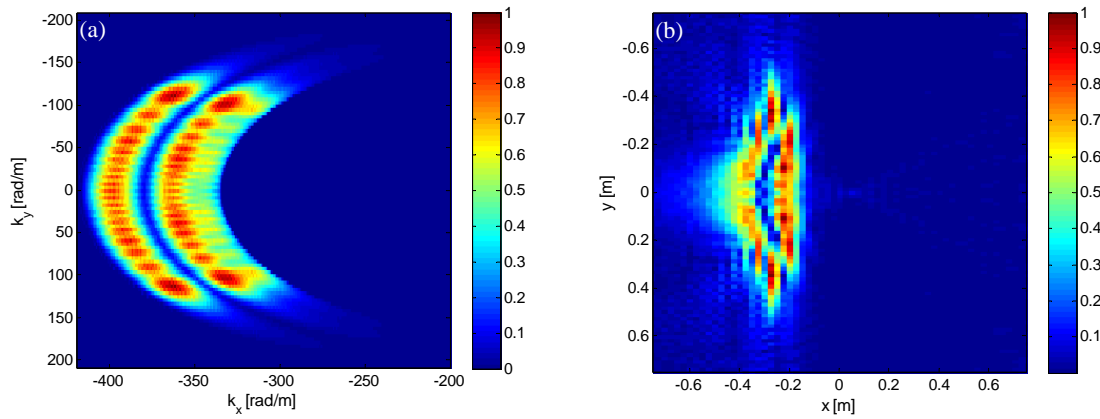


Figure 2-8. (a) The normalized magnitude of Fourier space data of the single cylindrical conducting object, and (b) the normalized tomographic image using the first UWB WGN waveform shown in Figure 2-5(a).

#### 2.4.2 Diffraction tomography with multiple transmitted iid WGN waveforms for a single scattering object

Figure 2-9 shows  $K$  iid UWB WGN waveforms being transmitted to reconstruct a final image of the object in order to bypass a shortcoming of the single transmission of WGN waveform displayed in Figure 2-8(b). The proposed imaging method with multiple iid WGN transmitted waveforms is established based on the method of the WGN periodogram averaging described in section 2.2.

As shown in Figure 2-9, the final tomographic image of the scattered object is reconstructed via sum and average of all  $K$  discrete images for  $K$ -th band-limited iid UWB WGN

transmitted waveforms. For scattered field and diffraction tomography simulations with multiple iid WGN waveforms, 10 iid UWB WGN waveforms over a frequency range from 8 GHz to 10 GHz are generated with 500 random amplitude samples drawn from  $N(0, \sigma^2)$ , and transmitted for backward scattering field data.

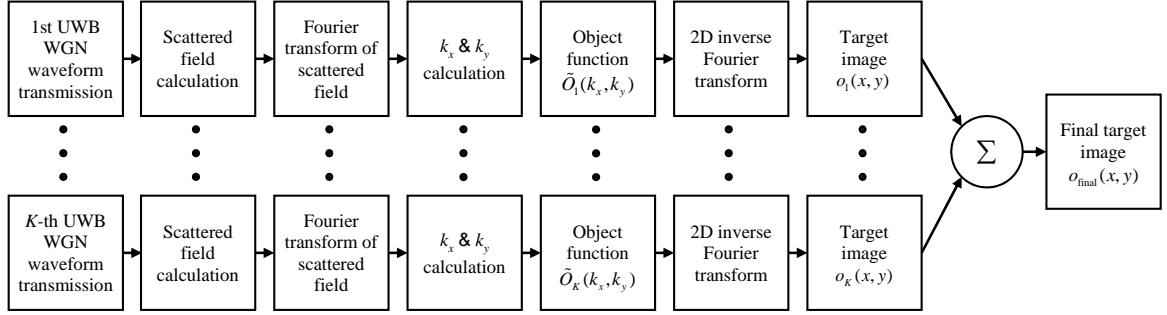


Figure 2-9. The image reconstruction method with  $K$  multiple iid WGN transmitted waveforms using diffraction tomography.

Figure 2-10(a), Figure 2-10(b), Figure 2-10(c), and Figure 2-10(d) display the four final tomographic images when one, three, seven and all ten discrete images are summed and averaged, respectively. Successful tomographic imaging of the target is achieved after averaging all ten images by visual inspection of the formed images as shown in Figure 2-10(d), and increasing the number of transmissions of the iid UWB WGN waveform tends to enhance the quality of final tomographic image of the object by reducing the variance of the spectral response of WGN.

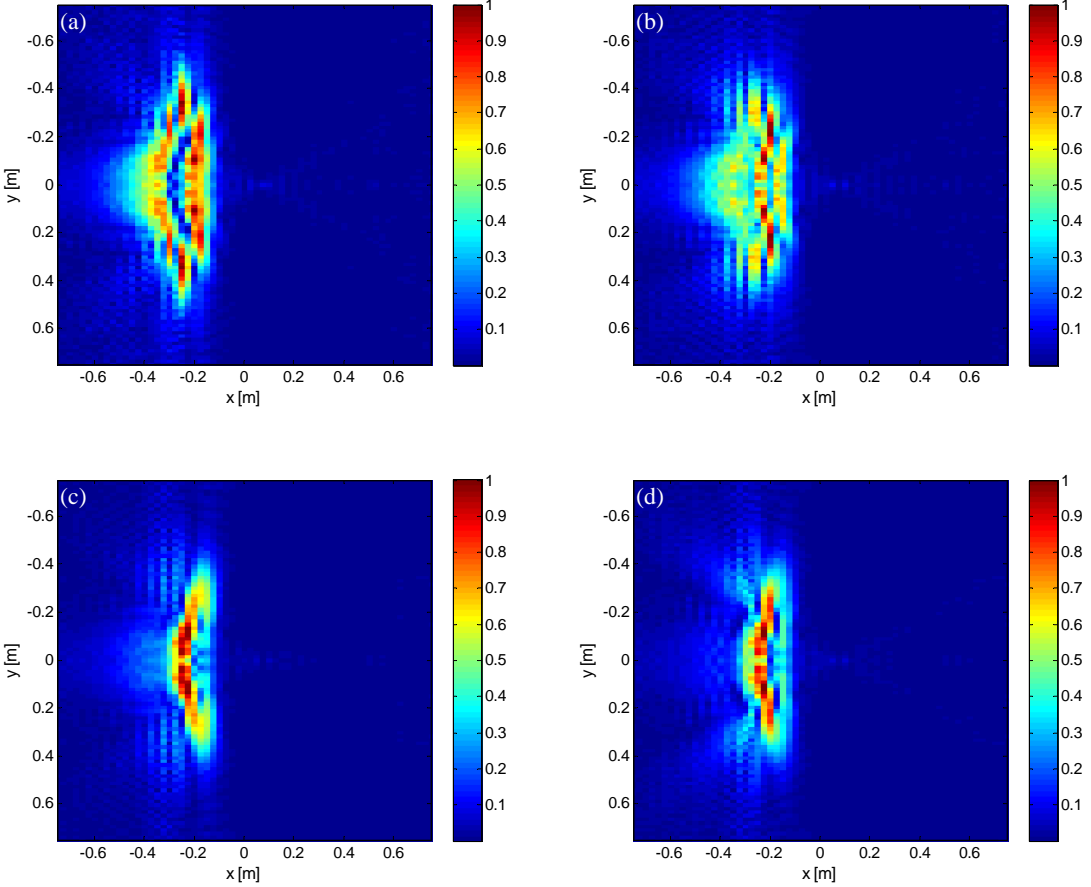


Figure 2-10. The final tomographic image of a single PEC cylinder located at  $(0,0)$  after summing and averaging process with the (a) one transmitted WGN waveform image, (b) three transmitted WGN waveform images, (c) seven transmitted WGN waveform images, and (d) all ten transmitted WGN waveform images. The colorbar indicates the normalized magnitude of scattering object function,  $o(x, y)$ .

#### 2.4.3 Diffraction tomography with multiple transmitted iid WGN waveforms for two symmetrically distributed scattering objects

Based on the simulation result of the single PEC cylinder case with multiple transmitted noise waveforms, transmitting multiple iid UWB WGN waveforms delivers the acceptable quality of image of the object for diffraction tomography.

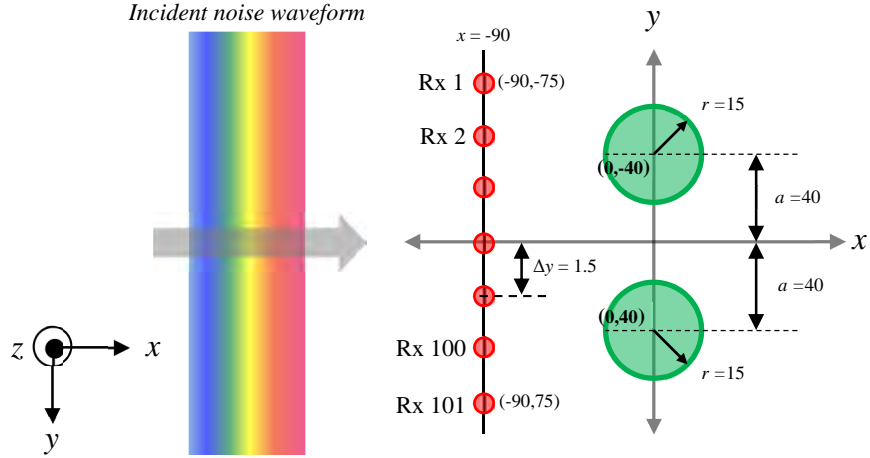


Figure 2-11. Two-dimensional backward scattering simulation geometry for two symmetrically distributed cylindrical conducting objects. Two PEC cylinders with radii of 15 cm are located at (0 cm, -40 cm) and (0 cm, 40 cm), and a linear receiving array is located 90 cm away from the origin in  $-x$  direction.

Two-dimensional backward scattering geometry for two cylindrical conducting objects, which is shown in Figure 2-11, is also simulated with 10 iid UWB WGN waveforms. Two cylindrical PEC objects with radii of 15 cm are located at (0 cm, -40 cm) and (0 cm, 40 cm) such that they are symmetrically positioned with respect to the  $x$ -axis. The distance from the center of each PEC cylinder to the  $x$ -axis,  $a$ , is 40 cm, and they are also assumed to be infinitely long along the  $z$ -axis. The coordinates of all 101 receivers, and the receiver spacing,  $\Delta y$ , remained the same as shown in Figure 2-3. The scattered field is uniformly sampled at Rx1 through Rx101 with same frequency swept within X-band over 8 GHz to 10 GHz in 41 steps as well.

For scattered field and diffraction tomography simulations for multiple scattering objects with multiple iid WGN waveforms, the same 10 iid UWB WGN waveforms, which are used for the simulation with a single PEC object in the previous section, are transmitted in the same sequence. The scattered field due to two symmetrically positioned PEC objects is calculated based on the equations derived in section 2.3, and the final tomographic image of objects is formed via the proposed image reconstruction method shown in Figure 2-9.

Figure 2-12(a), Figure 2-12(b), Figure 2-12(c), and Figure 2-12(d) display four final tomographic images for two symmetrically distributed PEC cylinders case when one, three, seven and all ten discrete images are summed and averaged, respectively. As shown in Figure 2-12(d), tomographic image of the two PEC cylinders is successfully reconstructed with multiple transmitted noise waveforms as expected. However, the mutual coupling effects due to the multiple PEC objects are also imaged in all tomographic images.

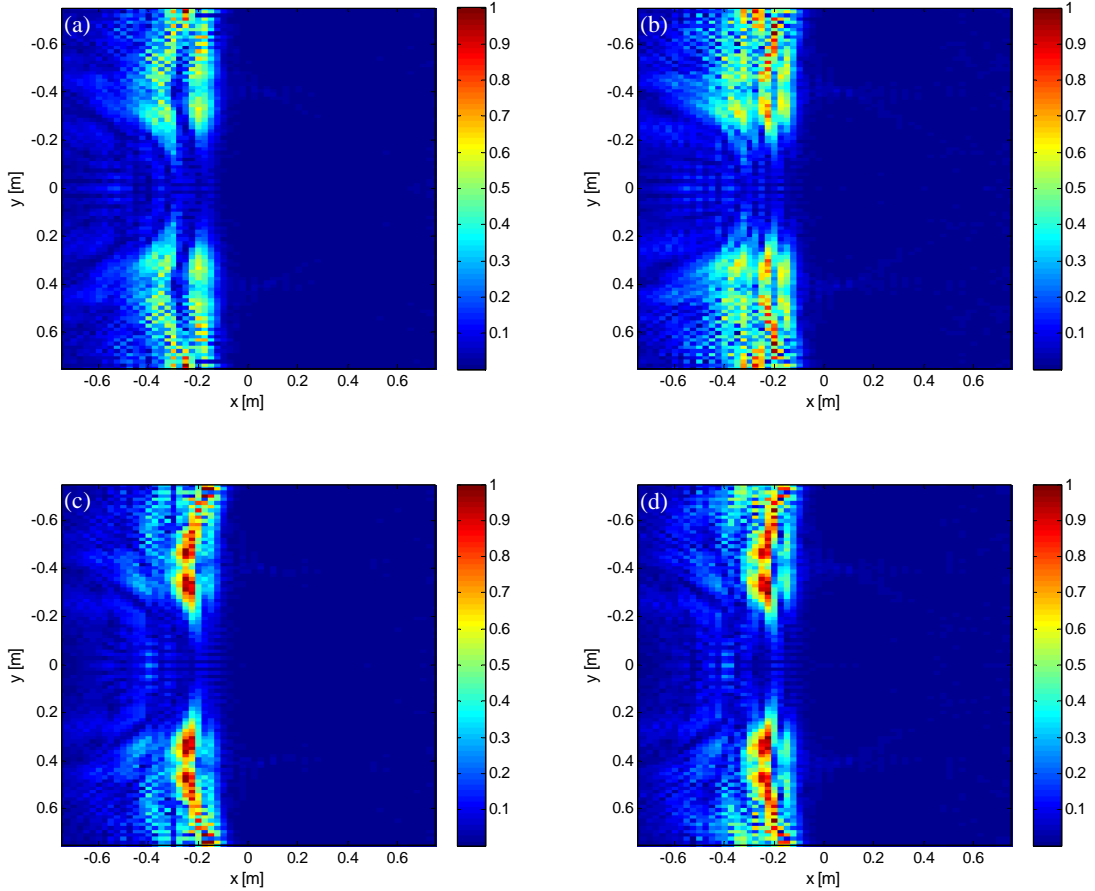


Figure 2-12. The final tomographic image of two symmetrically distributed PEC cylinders located at (0 cm, -40 cm) and (0 cm, 40 cm) after summing and averaging process with the (a) one transmitted WGN waveform image, (b) three transmitted WGN waveform images, (c) seven transmitted WGN waveform images, and (d) all ten transmitted WGN waveform images.

#### 2.4.4 Diffraction tomography with multiple transmitted iid WGN waveforms for two randomly distributed scattering objects

Two-dimensional backward scattering geometry for two randomly distributed cylindrical conducting objects is shown in Figure 2-13. The radii of both cylinders are 15 cm, and the positions of two cylinders are (-7.5 cm, 22.5 cm) and (35 cm, -55 cm). The general configuration of simulation geometry, such as number of transmitted UWB WGN waveforms, frequency swept ranges, coordinates of the linear receiving array, and the receiver spacing, is identical to the previous cases.

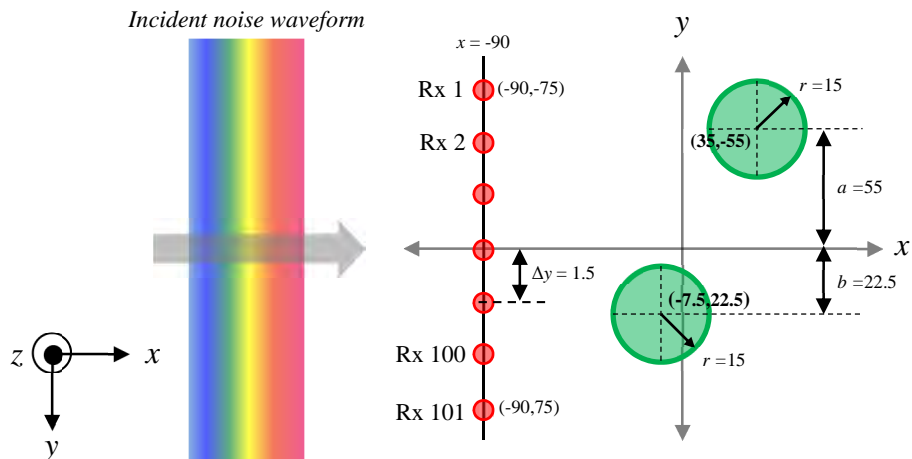


Figure 2-13. Two-dimensional backward scattering simulation geometry for two randomly distributed cylindrical conducting objects. PEC cylinders with radii of 15 cm are located at (-7.5 cm, 22.5 cm) and (35 cm, -55 cm).

Four final tomographic images for two randomly distributed PEC cylinders are displayed in Figure 2-14(a), Figure 2-14(b), Figure 2-14(c), and Figure 2-14(d) when one, three, seven and all ten discrete images are summed and averaged, respectively. Again, the mutual coupling effects are shown in the tomographic images as expected. The reconstructed images are shown to be in good agreement with the simulation geometry given in Figure 2-13.

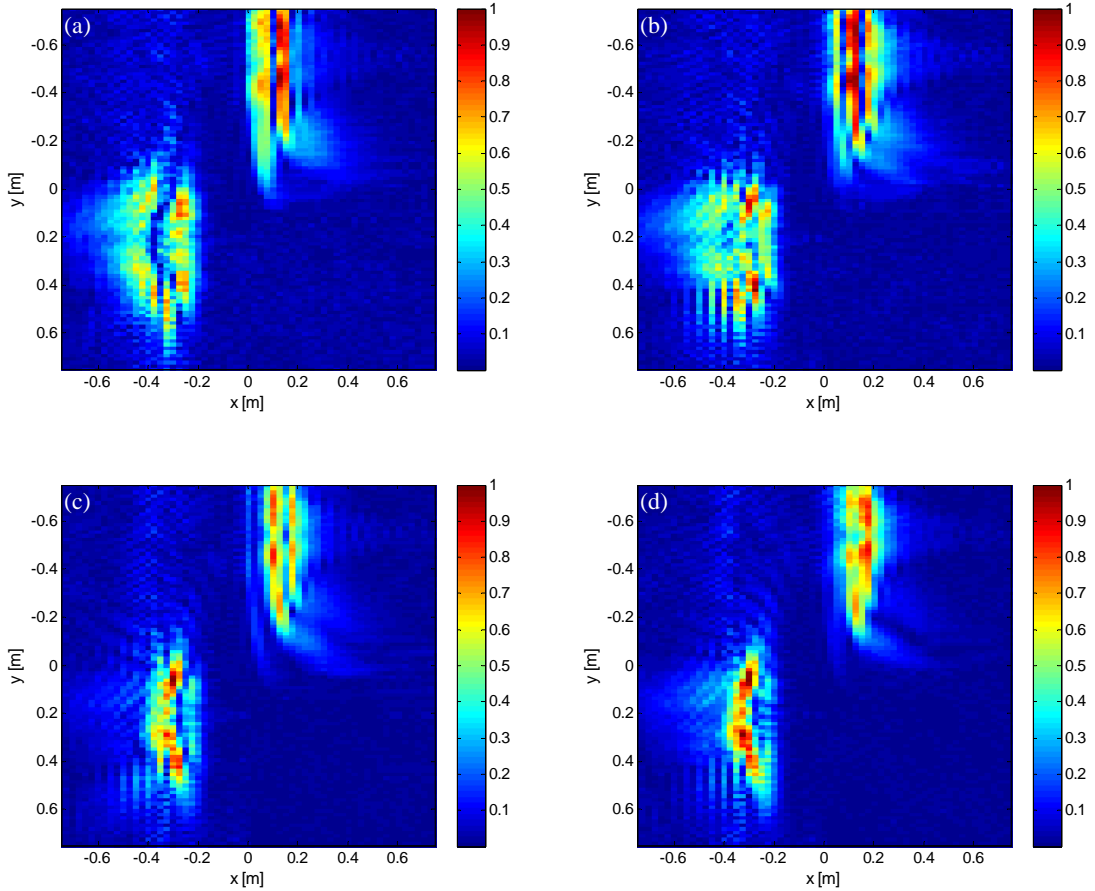


Figure 2-14. The final tomographic image of two randomly distributed PEC cylinders located at  $(-7.5 \text{ cm}, 22.5 \text{ cm})$  and  $(35 \text{ cm}, -55 \text{ cm})$  after summing and averaging process with the (a) one transmitted WGN waveform image, (b) three transmitted WGN waveform images, (c) seven transmitted WGN waveform images, and (d) all ten transmitted WGN waveform images.

#### 2.4.5 Diffraction tomography with multiple transmitted iid WGN waveforms for three randomly distributed scattering objects in different sizes

As shown in Figure 2-15, three PEC cylinders with radii of 7.5 cm, 10 cm, and 15 cm are located at  $(-22.5 \text{ cm}, -20 \text{ cm})$ ,  $(10 \text{ cm}, 50 \text{ cm})$ , and  $(25 \text{ cm}, -40 \text{ cm})$ , respectively. Again, the general configurations of simulation geometry remain unchanged as defined in previous cases.

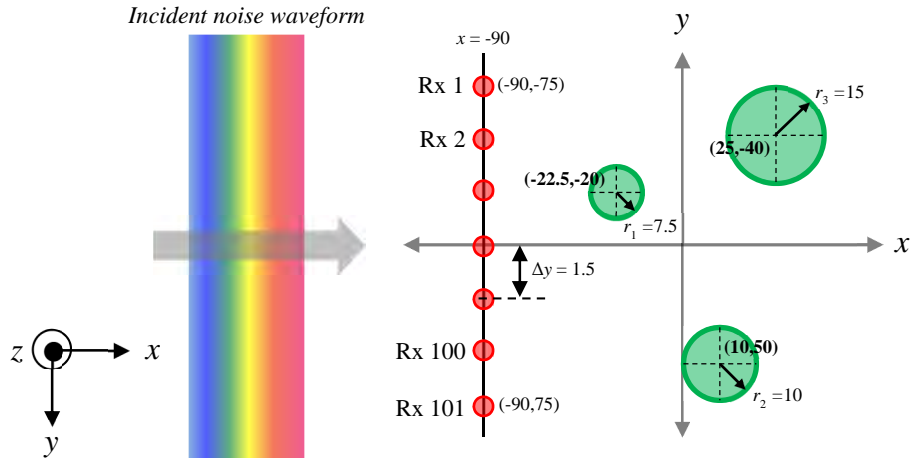


Figure 2-15. Two-dimensional backward scattering simulation geometry for three randomly distributed cylindrical conducting objects in different sizes. Three PEC cylinders with radii of 7.5 cm, 10 cm, and 15 cm are located at ( $-22.5$  cm,  $-20$  cm), ( $10$  cm,  $50$  cm), and ( $25$  cm,  $-40$  cm), respectively.

Figure 2-16(a), Figure 2-16(b), Figure 2-16(c), and Figure 2-16(d) show four final tomographic images for the scattering geometry given in Figure 2-15 when one, three, seven and all ten discrete images are summed and averaged, respectively. As shown in the previous cases, the image quality of reconstructed tomographic images for unevenly distributed multiple scattering objects is affected by the mutual coupling effects. Successful tomographic image of the target is reconstructed based on multiple transmitted noise waveforms as shown in Figure 2-16(d).

Based on the numerical simulation results of various scattering target geometries using multiple band-limited iid UWB WGN waveforms, increasing the number of transmissions of the iid UWB WGN waveform improves the quality of tomographic image by reducing the variance of the spectral response of WGN as stated in section 2.2.

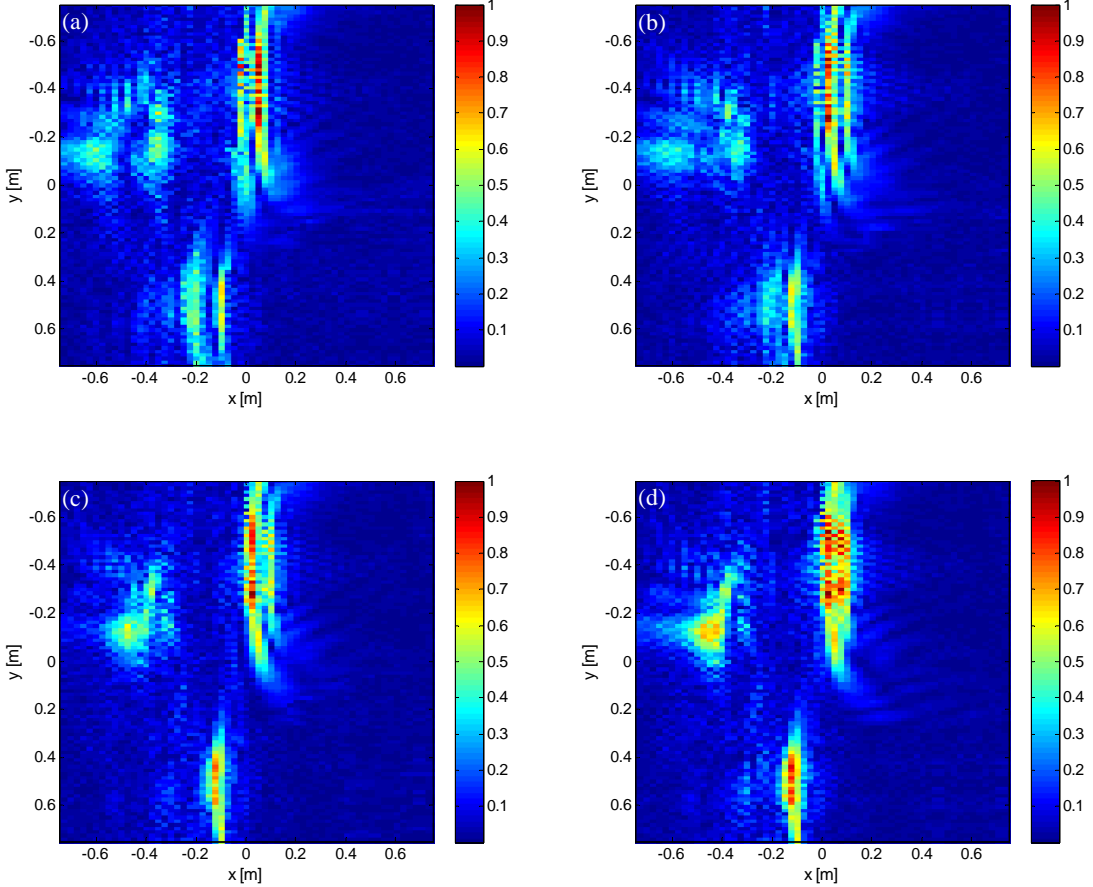


Figure 2-16. The final tomographic image of three randomly distributed PEC cylinders in different sizes after summing and averaging process with the (a) one transmitted WGN waveform image, (b) three transmitted WGN waveform images, (c) seven transmitted WGN waveform images, and (d) all ten transmitted WGN waveform images.

## 2.5 Image Quality Measure

As concluded in section 2.4, increasing the number of transmissions of the iid WGN waveform tends to enhance the formed tomographic image. The image quality measures (IQMs) are discussed to determine the quality of tomographic images based on quantitative analysis. A good subjective assessment is required to evaluate the image quality and the performance of imaging systems. Various methods to measure the image quality and investigate their statistical performance have been studied [34, 35]. The most frequently used measures are deviations

between the reference and reconstructed image with varieties of the mean square error (MSE) [36, 37]. The reasons for the widespread popularity of the analysis based on MSE calculations are their mathematical tractability and the fact that it is often straightforward to design systems that minimize the MSE.

### 2.5.1 Reference image generation

Prior to measuring the image quality of reconstructed tomographic images shown in the previous section, a “reference” image is obtained via diffraction tomography proposed in Figure 2-6 using the first derivative Gaussian waveform. The first derivative Gaussian waveform possesses the desirable property in that it has zero average value. Since it has no DC component, the first derivative Gaussian waveform is the most popular pulse shape for various UWB applications [38, 39]; thus, it can be considered to be an appropriate waveform for generating reference images to compare with our reconstructed images. Figure 2-17(a) displays the first derivative Gaussian input waveform with a pulse width of 0.1 ns, and the frequency spectrum of the pulse is relatively flat in the range of 8 GHz –10 GHz as shown in Figure 2-17(b).

The Fourier space data and the tomographic image of four scattering target geometries in section 2.4 are generated with the first derivative Gaussian input waveform shown in Figure 2-17(a), and they are displayed in Figure 2-18, Figure 2-19, Figure 2-20, and Figure 2-21. These tomographic images are considered to be the reference images for IQM analysis.

The Fourier space data and the tomographic image of four scattering target geometries in section 2.4 are generated with the first derivative Gaussian input waveform shown in Figure 2-17(a), and they are displayed in Figure 2-18, Figure 2-19, Figure 2-20, and Figure 2-21. These tomographic images are considered to be the reference images for IQM analysis.

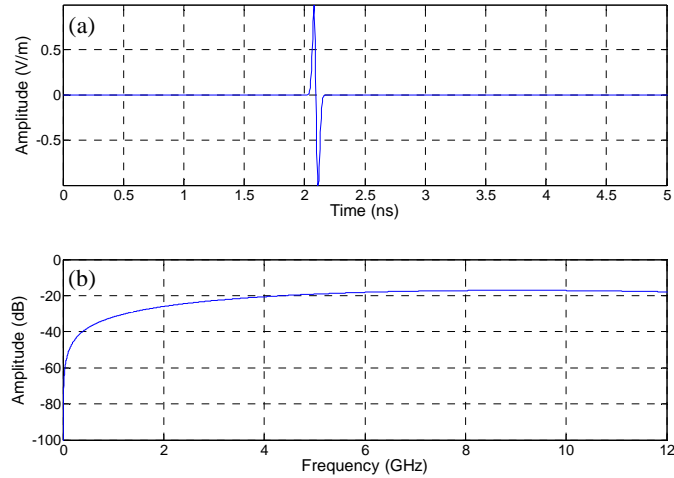


Figure 2-17. (a) The first derivative Gaussian input waveform with a pulse width of 0.1 ns. (b) The frequency spectrum of the first derivative Gaussian input waveform shown in Figure 2-17(a). The frequency spectrum ranges are displayed from DC to 12 GHz only.

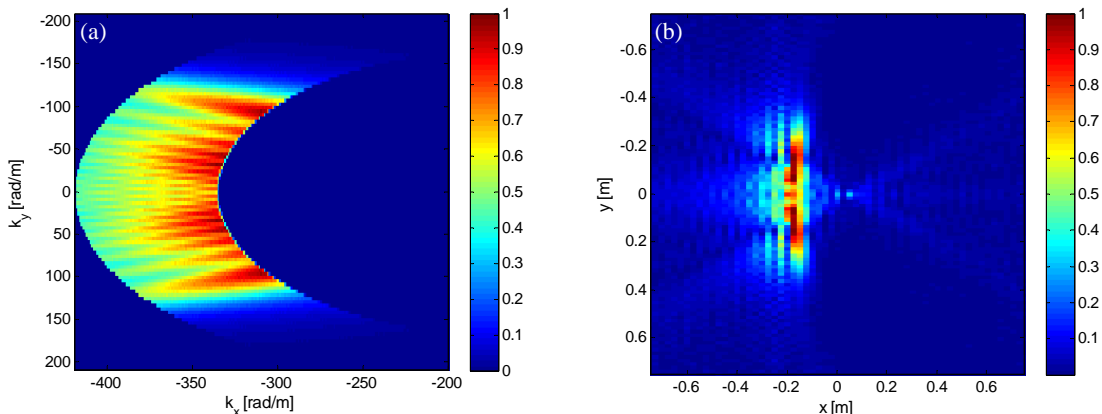


Figure 2-18. (a) The normalized magnitude of Fourier space data based on the transmission of the first derivative Gaussian waveform shown in Figure 2-17(a) for the single cylindrical PEC object shown in Figure 2-3. (b) The tomographic image of the single cylindrical conducting object located at (0 cm, 0 cm). The colorbar indicates the normalized magnitude of scattering object function,  $o(x, y)$ .

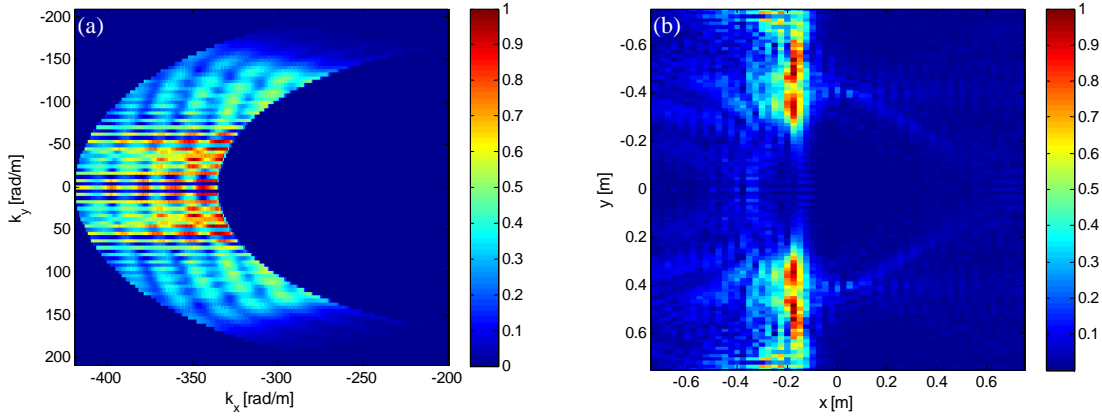


Figure 2-19. (a) The magnitude of Fourier space data based on the transmission of the first derivative Gaussian waveform shown in Figure 2-17(a) for two symmetrically distributed cylindrical PEC objects shown in Figure 2-11. (b) The tomographic image of two symmetrically distributed cylindrical conducting objects located at (0 cm, -40 cm) and (0 cm, 40 cm).

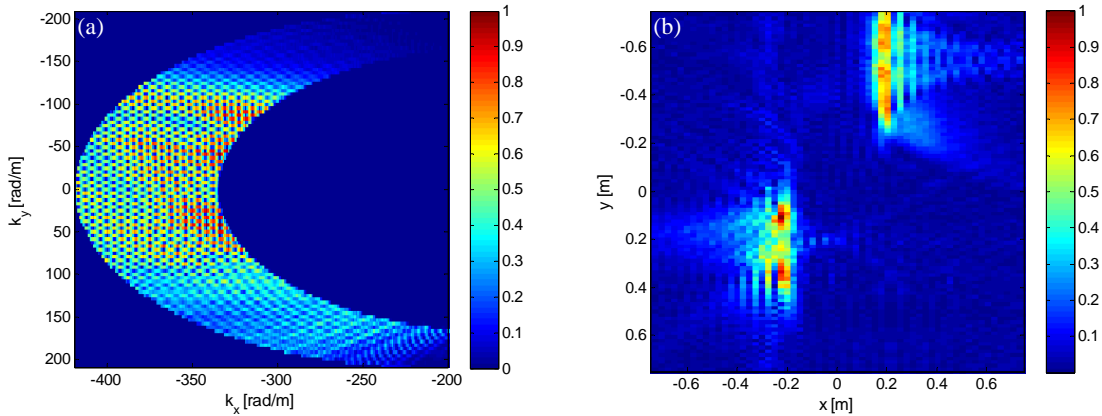


Figure 2-20. (a) The magnitude of Fourier space data based on the transmission of the first derivative Gaussian waveform shown in Figure 2-17(a) for two randomly distributed cylindrical PEC objects shown in Figure 2-13. (b) The tomographic image of two randomly distributed cylindrical conducting objects located at (-7.5 cm, 22.5 cm) and (35 cm, -55 cm).

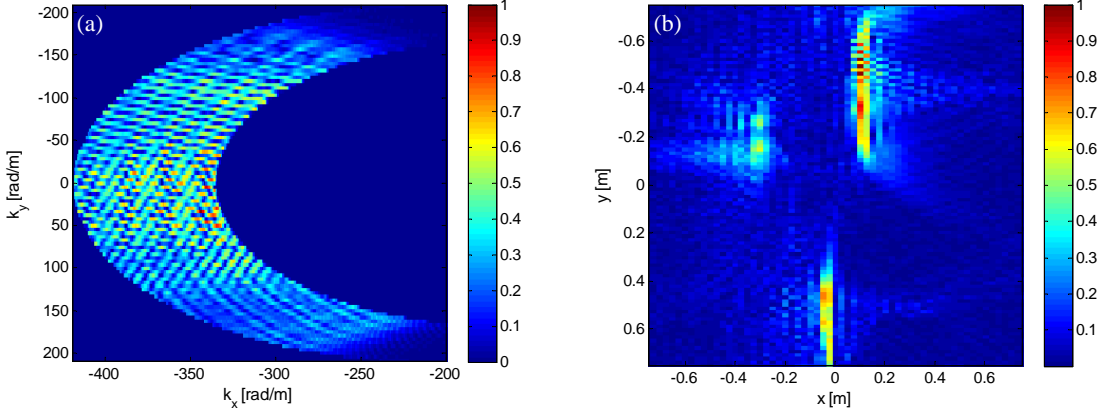


Figure 2-21. (a) The magnitude of Fourier space data based on the transmission of the first derivative Gaussian waveform shown in Figure 2-17(a) for three randomly distributed cylindrical PEC objects in different sizes shown in Figure 2-15. (b) The tomographic image of three randomly distributed cylindrical conducting objects in different sizes located at (-22.5 cm, -20 cm), (10 cm, 50 cm), and (25 cm, -40 cm).

### 2.5.2 Pixel difference-based measure

The tomographic images shown in section 2.4 are obtained based on 10 iid UWB WGN transmitted waveforms, and the image enhancement technique is not implemented in diffraction tomography algorithm. Every pixel in all images is generated based on the scattering object function defined in (2.22). MSE is the cumulative mean squared error between the corresponding pixels of the reference images and the reconstructed images based on multiple iid UWB WGN transmitted waveforms. MSE is defined as

$$\text{MSE} = \frac{1}{MN} \sum_{y=0}^{M-1} \sum_{x=0}^{N-1} [R(x_m, y_n) - S(x_m, y_n)]^2 \quad (2.24)$$

where  $R(x_m, y_n)$  and  $S(x_m, y_n)$  represent the value of each pixel of the reference image and reconstructed tomographic images with multiple iid UWB WGN transmitted waveforms, respectively, and  $M$  and  $N$  are the dimensions of the images.

Each pixel of tomographic images represents the normalized magnitude of scattering object function,  $o(x, y)$ , and the dimensions of images are equivalent to the number of pixels across the  $x$ -axis and  $y$ -axis. By using (2.24), MSE values are calculated to evaluate the deviation of the pixel values from those of the corresponding reference image, as the iid noise images are summed, averaged, and normalized.

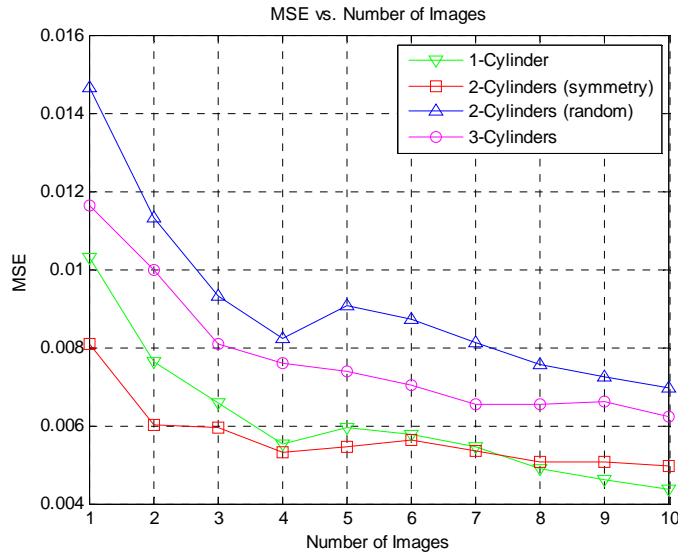


Figure 2-22. MSE versus number of reconstructed images after normalization. MSE decreases as the number of reconstructed images is overlapped.

Figure 2-22 displays the MSE versus number of overlapping reconstructed images. Such quantitative analysis shows that the tomographic images of the objects become clear and distinctive as the number of reconstructed images based on iid WGN waveforms increases. To be more specific, as shown in Figure 2-22, MSE decreases as the number of overlapped reconstructed images based on iid UWB WGN transmitted waveforms increases.

### 2.5.3 Signal-to-noise ratio effects on image quality

All tomographic images shown above are formed in the absence of noise in the system; that is, signal-to-noise ratio (SNR) is equal to infinity. In practical situations, the received signal shows unpredictable perturbations due to the contributions of various noise sources in communication and imaging systems [40, 41]. For example, thermal noise is present in all electronic devices and transmission media and is uniformly distributed across the frequency spectrum. When backscattering data acquisition is performed with a signal analyzer, the recorded data consists of scattered field information with some thermal noise from the equipment and cables. However, the collected data can be viewed as the sum of the scattered field and the additive white Gaussian noise since they are uncorrelated.

In this section, the white Gaussian noise is added accordingly to the collected scattered field dataset, establishing simulation environment with 4 different SNR values: -20 dB, -10 dB, 0 dB, and +10 dB. Prior to measuring the quality of the final tomographic images with various SNRs, MSE values are calculated to determine the deviation of the pixel values from that of the corresponding reference image, as the iid noise images generated with the corresponding SNR values are summed, averaged, and normalized. Based on the previous quantitative analysis results shown in Figure 2-22, the image quality of the tomographic image is expected to be enhanced as the number of reconstructed images increases regardless of SNR values. Figure 2-23 displays the MSE versus number of overlapping reconstructed images with 4 different SNRs for four scattering target geometries shown in section 2.4.

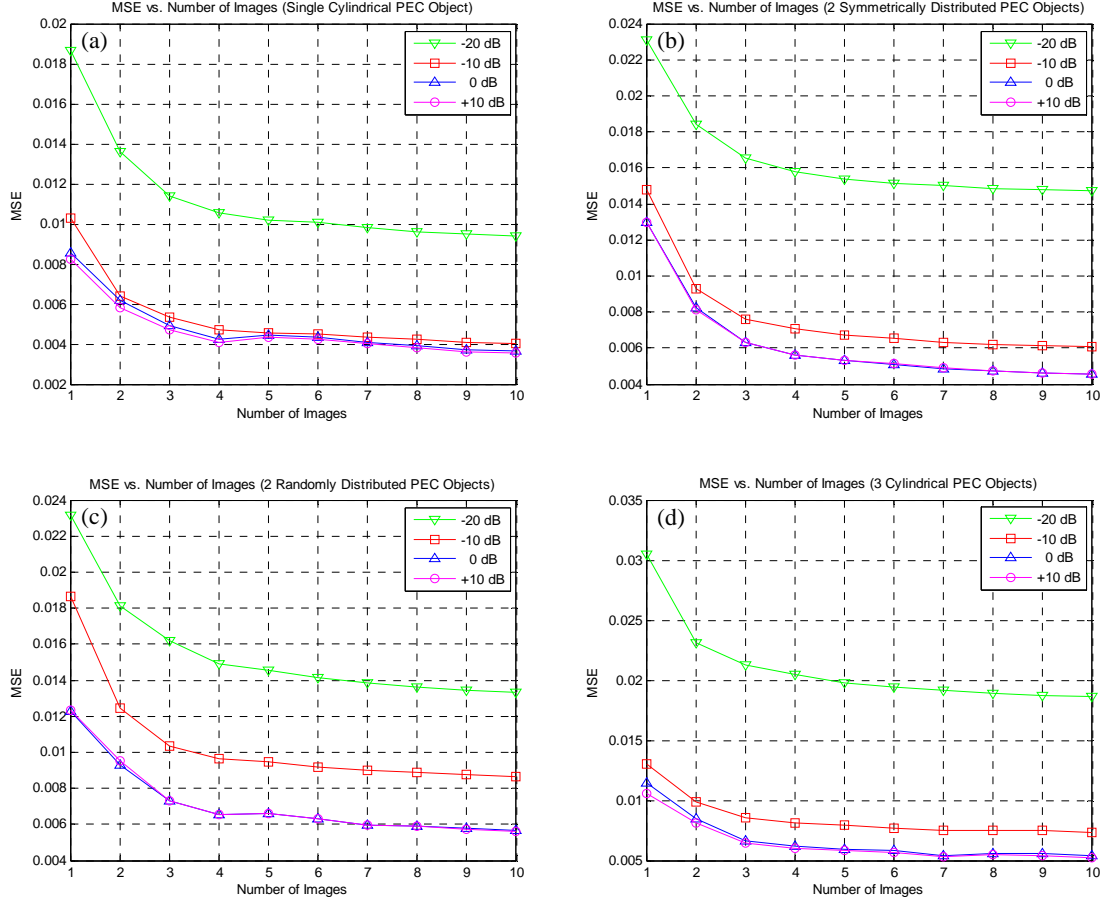


Figure 2-23. MSE versus number of reconstructed images after normalization with 4 different SNR values for (a) single cylindrical PEC object, (b) two symmetrically distributed cylindrical PEC objects, (c) two randomly distributed cylindrical PEC objects, and (d) three randomly distributed cylindrical PEC objects in different sizes. For all cases, MSE decreases as the number of reconstructed images is overlapped regardless of SNRs.

After completion of total 10 transmissions of iid noise waveforms for 4 different SNR values defined above, the final tomographic images of all four scattering geometries are achieved and displayed in Figure 2-24 through Figure 2-27.

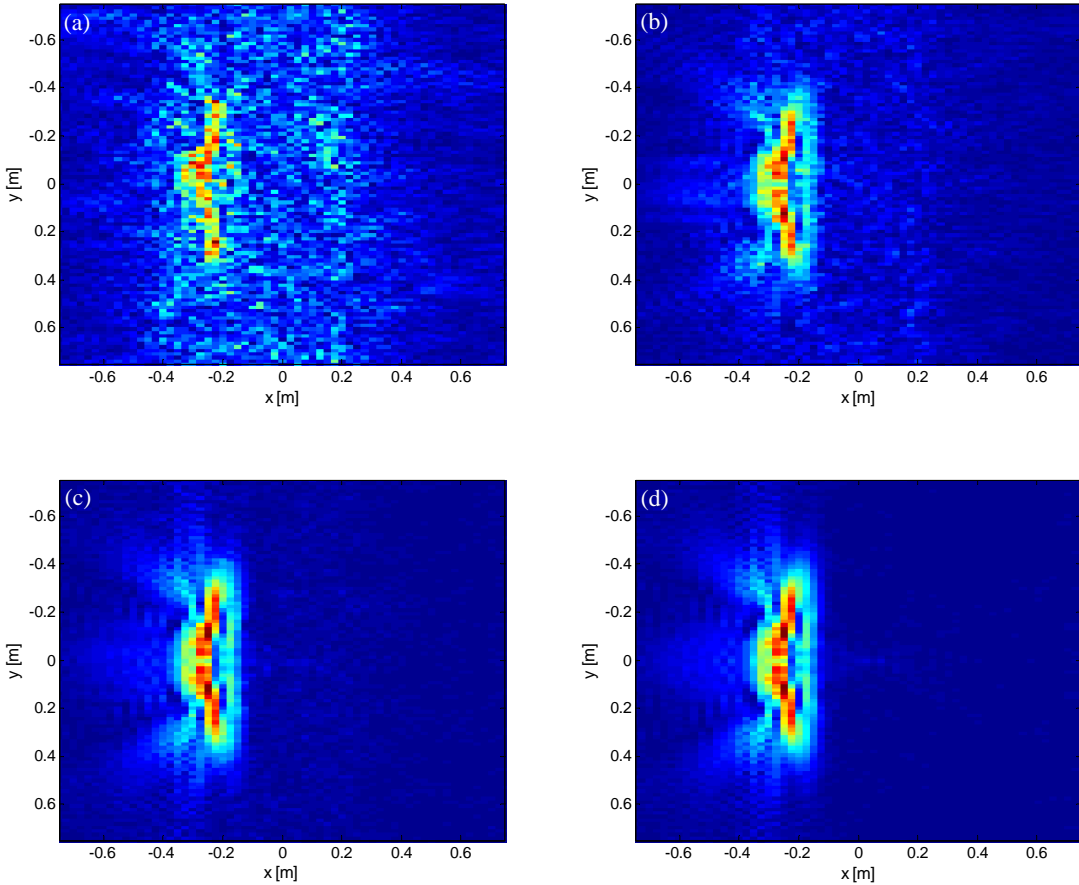


Figure 2-24. The final tomographic images after summing and averaging process with the 10 iid noise waveforms with various SNRs for a single PEC cylinder: (a) SNR = -20 dB, (b) SNR = -10 dB, (c) SNR = 0 dB, and (d) SNR = +10 dB.

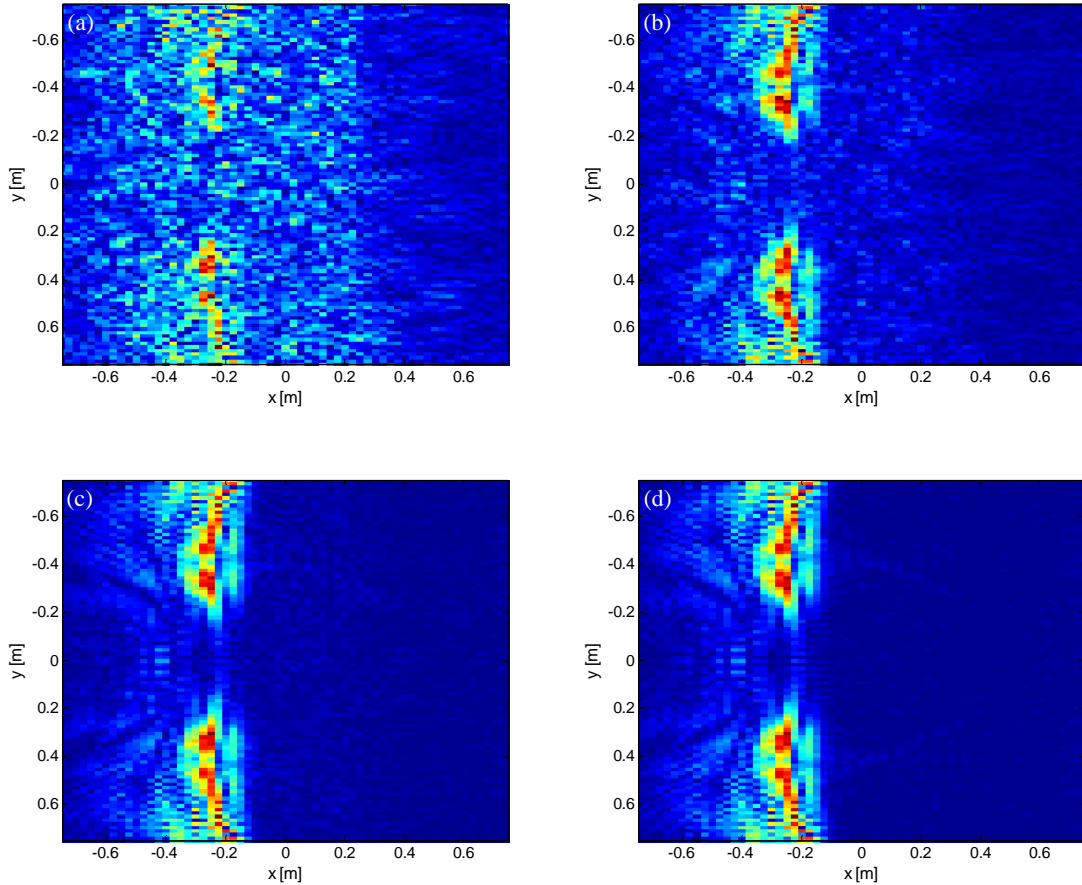


Figure 2-25. The final tomographic images after summing and averaging process with the 10 iid noise waveforms with various SNRs for two symmetrically distributed PEC cylinders: (a) SNR =  $-20$  dB, (b) SNR =  $-10$  dB, (c) SNR =  $0$  dB, and (d) SNR =  $+10$  dB.

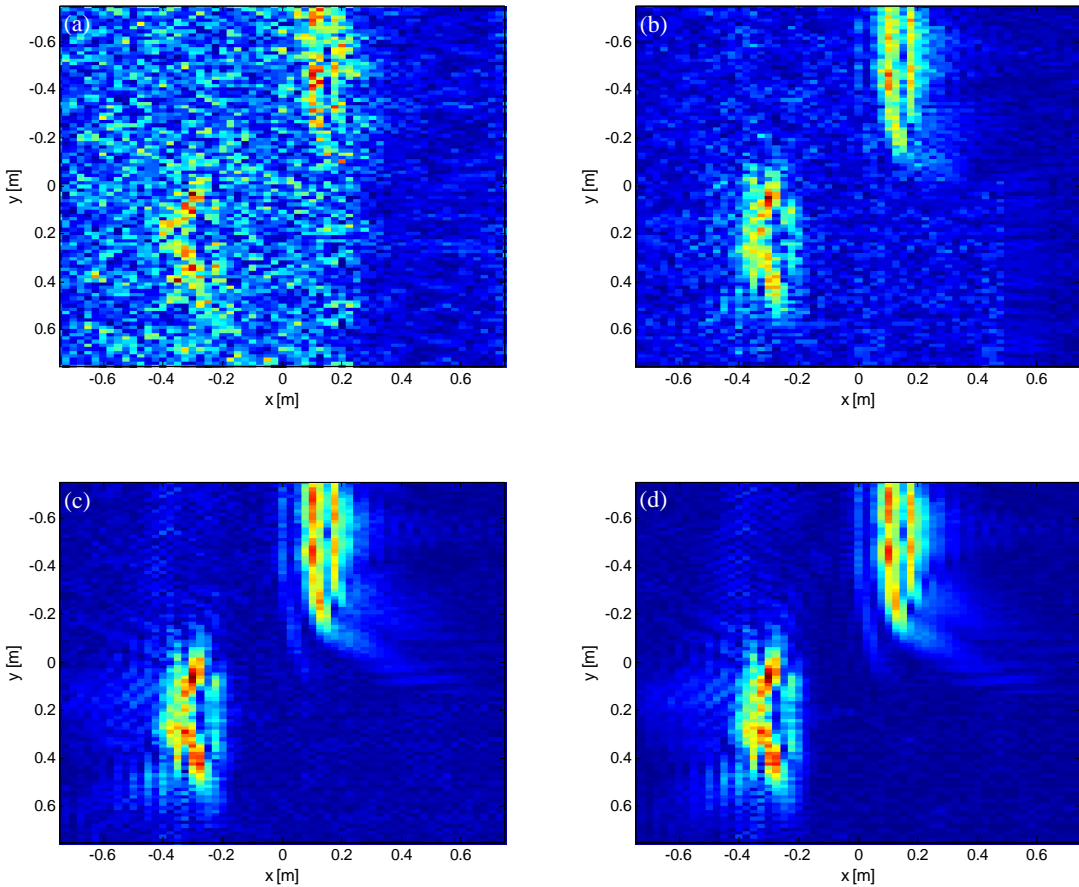


Figure 2-26. The final tomographic images after summing and averaging process with the 10 iid noise waveforms with various SNRs for two randomly distributed PEC cylinders: (a) SNR =  $-20$  dB, (b) SNR =  $-10$  dB, (c) SNR =  $0$  dB, and (d) SNR =  $+10$  dB.

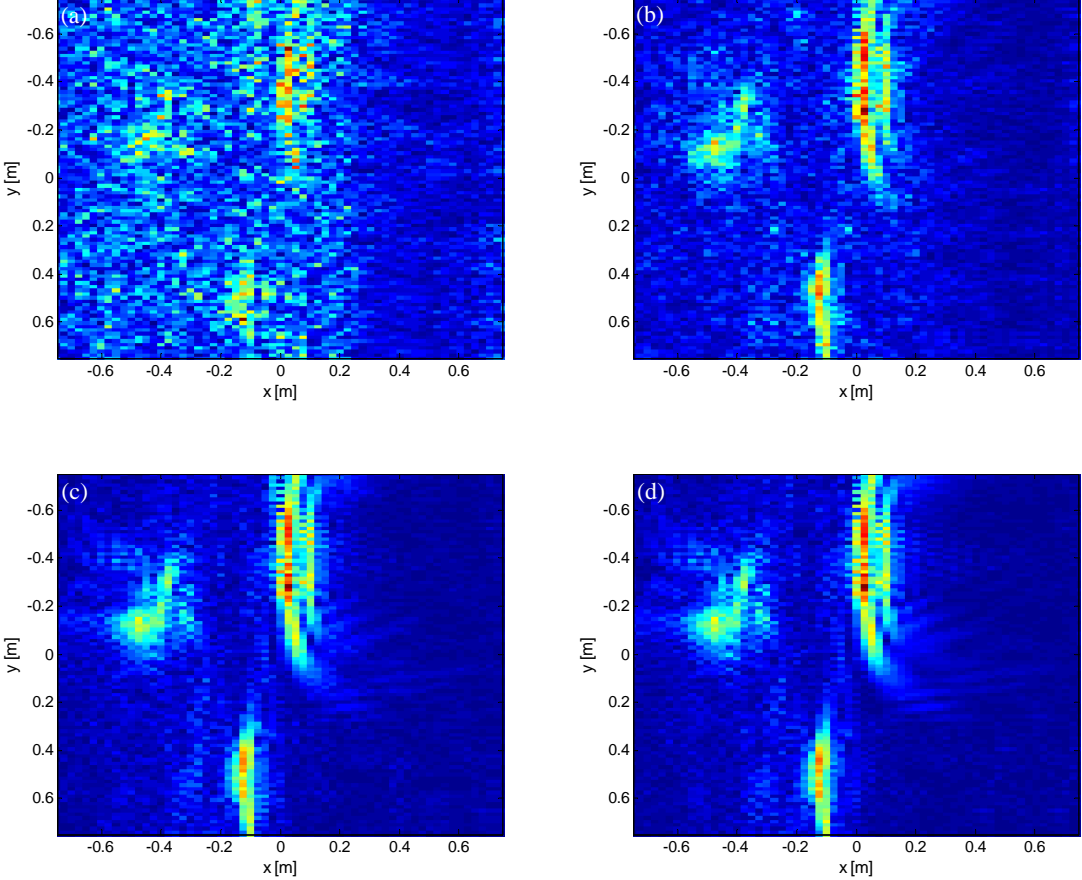


Figure 2-27. The final tomographic images after summing and averaging process with the 10 iid noise waveforms with various SNRs for three randomly distributed PEC cylinders in different sizes: (a) SNR =  $-20$  dB, (b) SNR =  $-10$  dB, (c) SNR =  $0$  dB, and (d) SNR =  $+10$  dB.

As shown in Figure 2-24 through Figure 2-27, the image quality of the final tomographic image after summing, averaging, and normalizing process with transmitting 10 iid noise waveforms is truly affected by the additive white Gaussian noise. By visual inspection of the formed images, the image degradation due to the additive Gaussian noise is clearly displayed when SNR is set to  $-20$  dB. In contrast, no such image degradation is observed at relatively higher SNRs, that is, SNR of  $+10$  dB.

In order to evaluate the overall impact of noise effect on the formed tomographic images, MSE is calculated at the SNR range from  $-20$  dB to  $+10$  dB. Figure 2-28 explains the

relationship between the image quality degradation after 10 images and SNR. The rate of change in MSE is the maximum at the SNR range between  $-20$  dB and  $-10$  dB, and this is the SNR range where the final tomographic image is severely degraded by unwanted noise. However, the rate of change in MSE starts falling as SNR increases, which indicates that the tomographic image is less affected by the noise contributions at high SNR. The results shown in Figure 2-28 are the rough measure to estimate the image quality on the final tomographic images in practical implementation of the imaging system and designs for actual experiment.

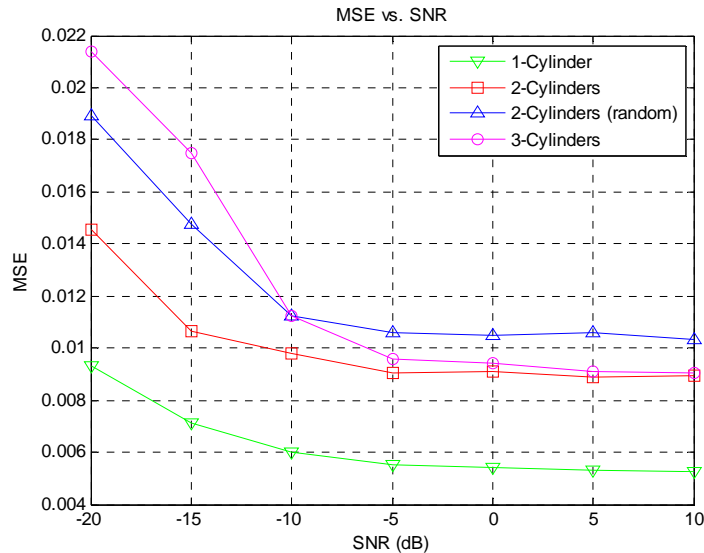


Figure 2-28. MSE versus SNR values for all final tomographic images shown in Figure 2-24(d) through Figure 2-27(d). MSE decreases as the level of SNR increases.

## 2.6 Summary

This chapter shows that tomographic images of scattering objects are successfully achieved with multiple transmissions of random noise waveforms. From the simulation results, a single transmitted UWB WGN may not be sufficient to generate the correct tomographic image due to the practical implementation of a transmitted random noise waveform. However, multiple

iid UWB WGN transmitted waveforms can bypass the shortcoming of a single transmission of UWB WGN waveform, forming a correct image of target objects by summing and averaging discrete object images based on each iid WGN waveform.

Also the image quality of the tomographic image after completion of multiple transmissions of iid noise waveforms is analyzed. MSE is used to measure the image quality of all tomographic images in this chapter. Image quality of the tomographic images based on the random noise waveform is enhanced as the number of iid noise waveform transmissions increases. The presence of white Gaussian noise degrades the image quality; however, the suppression of unwanted noise contributions by controlling SNR can help to achieve successful tomographic images in practical radar imaging systems.

## 2.7 References

- [1] B.M. Horton, "Noise-modulated distance measuring systems," *Proceedings of the IRE*, vol. 47, pp. 821–828, 1959.
- [2] M.P. Grant, G.R. Cooper, and A.K. Kamal, "A class of noise radar systems," *Proceedings of the IEEE*, vol. 51, pp. 1060–1061, 1963.
- [3] M. Dawood and R.M. Narayanan, "Multipath and ground clutter analysis for a UWB noise radar," *IEEE Transactions on Aerospace and Electronic Systems*, vol. 38, pp. 838–853, 2002.
- [4] K. Kulpa, J. Misiurewicz, Z. Gajo, and M. Malanowski, "A simple robust detection of weak target in noise radars," in *Proceedings of the 2007 European Radar Conference (EuRAD 2007)*, Munich, Germany, October 2007, pp. 275–278.

- [5] Y. Zhang and R.M. Narayanan, "Design considerations for a real-time random-noise tracking radar," *IEEE Transactions on Aerospace and Electronic Systems*, vol. 40, pp. 434–445, 2004.
- [6] D.A. Ausherman, A. Kozma, J.L. Walker, H.M. Jones, and E.C. Poggio, "Developments in radar imaging," *IEEE Transactions on Aerospace and Electronic Systems*, vol. 20, pp. 363–400, 1984.
- [7] H.J. Shin, R.M. Narayanan, and M. Rangaswamy, "Tomographic imaging with ultra-wideband noise radar using time-domain data," in *Proceedings of the SPIE Conference on Radar Sensor Technology XVII*, Baltimore, MD, April 2013, pp. 87140R-1–87140R-9.
- [8] L. Jofre, A. Broquetas, J. Romeu, S. Blanch, A. P. Toda, X. Fabregas, and A. Cardama, "UWB tomographic radar imaging of penetrable and impenetrable objects," *Proceedings of the IEEE*, vol. 97, pp. 451–464, 2009.
- [9] X. Li, E.J. Bond, B.D. Van Veen, and S.C. Hagness, "An overview of ultra-wideband microwave imaging via space-time beamforming for early-stage breast-cancer detection," *IEEE Antennas and Propagation Magazine*, vol. 47, pp. 19–34, 2005.
- [10] T.M. Grzegorczyk, P.M. Meaney, P.A. Kaufman, R.M. di Florio-Alexander, and K.D. Paulsen, "Fast 3-D tomographic microwave imaging for breast cancer detection," *IEEE Transactions on Medical Imaging*, vol. 31, pp. 1584–1592, 2012.
- [11] M.H. Khalil, W. Shahzad, and J.D. Xu, "In the medical field detection of breast cancer by microwave imaging is a robust tool," in *Proceedings of the 25<sup>th</sup> International Vacuum Nanoelectronics Conference (IVNC)*, Jeju, South Korea, July 2012, 2 pages, doi: 10.1109/IVNC.2012.6316913.
- [12] Z. Wang, E.G. Lim, Y.Tang, and M. Leach, "Medical applications of microwave imaging," *The Scientific World Journal*, Article ID 147016, vol. 2014, 7 pages, doi: 10.1155/2014/147016.

- [13] Y.J. Kim, L. Jofre, F. De Flaviis, and M.Q. Feng, "Microwave reflection tomographic array for damage detection of civil structures," *IEEE Transactions on Antennas and Propagation*, vol. 51, pp. 3022–3032, 2003.
- [14] S. Kharkovsky, J. Case, M. Ghasr, R. Zoughi, S. Bae, and A. Belarbi, "Application of microwave 3D SAR imaging technique for evaluation of corrosion in steel rebars embedded in cement-based structures," in *Review of Progress in Quantitative Nondestructive Evaluation*, vol. 31, 2012, pp. 1516–1523.
- [15] O. Güneş and O. Büyüköztürk, "Microwave imaging of plain and reinforced concrete for NDT using backpropagation algorithm," in *Nondestructive Testing of Materials and Structures* (Editors: O. Güneş and Y. Akkaya), Springer, 2013, pp. 703–709.
- [16] D. Zimdars and J.S. White, "Terahertz reflection imaging for package and personnel inspection," in *Proceedings of the SPIE Conference on Terahertz for Military and Security Applications II*, Orlando, FL, April 2004, pp. 78–83.
- [17] S. Almazroui and W. Wang, "Microwave tomography for security applications," in *Proceedings of the 2012 International Conference on Information Technology and e-Services (ICITEs)*, Sousse, Tunisia, March 2012, 3 pages, doi: 10.1109/ICITEs.2012.6216658.
- [18] O. Yurduseven, "Indirect microwave holographic imaging of concealed ordnance for airport security imaging systems," *Progress In Electromagnetics Research*, vol. 146, pp. 7–13, 2014.
- [19] L. Jofre, A.P. Toda, J. Montana, P. C. Carrascosa, J. Romeu, S. Blanch, and A. Cardama, "UWB short-range bifocusing tomographic imaging," *IEEE Transactions on Instrumentation and Measurement*, vol. 57, pp. 2414–2420, 2008.

- [20] C.-P. Lai and R.M. Narayanan, "Ultrawideband random noise radar design for through-wall surveillance," *IEEE Transactions on Aerospace and Electronic Systems*, vol. 46, pp. 1716–1730, 2010.
- [21] R. Vela, R.M. Narayanan, K.A. Gallagher, and M. Rangaswamy, "Noise radar tomography," in *Proceedings of the 2012 IEEE Radar Conference (RADAR)*, Atlanta, GA, May 2012, pp. 720–724.
- [22] A. Leon-Garcia, *Probability and Random Processes for Electrical Engineering*, 2nd ed. Reading, MA: Addison-Wesley, 1994.
- [23] G. Jenkins and D. Watts, *Spectral Analysis and its Applications*. San Francisco, CA: Holden-Day, 1968.
- [24] A.V. Oppenheim, R.W. Schafer, and J.R. Buck, *Discrete-Time Signal Processing*, 2nd ed. Upper Saddle River, NJ: Prentice Hall, 1999.
- [25] M. S. Bartlett, "Periodogram analysis and continuous spectra," *Biometrika*, vol. 37, pp. 1–16, 1950.
- [26] S. K. Kenne and J.F. Greenleaf, "Limited angle multifrequency diffraction tomography," *IEEE Transactions on Sonics and Ultrasonics*, vol. 29, pp. 213–216, 1982.
- [27] B. Roberts and A. Kak, "Reflection mode diffraction tomography," *Ultrasonic imaging*, vol. 7, pp. 300-320, 1985.
- [28] M. Soumekh, "Surface imaging via wave equation inversion," in *Acoustical Imaging* (Editor: L.W. Kessler), Springer, 1988, pp. 383–393.
- [29] S. Pan and A.C. Kak, "A computational study of reconstruction algorithms for diffraction tomography: Interpolation versus filtered-backpropagation," *IEEE Transactions on Acoustics, Speech and Signal Processing*, vol. 31, pp. 1262–1275, 1983.

- [30] T.-H. Chu and K. Lee, "Wide-band microwave diffraction tomography under Born approximation," *IEEE Transactions on Antennas and Propagation*, vol. 37, pp. 515–519, 1989.
- [31] J. C. Bolomey and C. Pichot, "Microwave tomography: from theory to practical imaging systems," *International Journal of Imaging Systems and Technology*, vol. 2, pp. 144–156, 1990.
- [32] H.J. Shin, R.M. Narayanan, and M. Rangaswamy, "Diffraction tomography for ultra-wideband noise radar and imaging quality measure of a cylindrical perfectly conducting object," in *Proceedings of the 2014 IEEE Radar Conference*, Cincinnati, OH, May 2014, pp. 702–707.
- [33] H. J. Shin, R. M. Narayanan and M. Rangaswamy, "Ultra-wideband noise radar imaging of cylindrical PEC objects using diffraction tomography," in Proceedings of the *SPIE Conference on Radar Sensor Technology XVIII*, Baltimore, MD, May 2014, pp. 90770J-1–90770J-10.
- [34] S. Valle, L. Zanzi and F. Rocca, "Radar tomography for NDT: comparison of techniques," *Journal of Applied Geophysics*, vol. 41, pp. 259–269, 1999.
- [35] K. Sayood, "Statistical evaluation of image quality measures," *Journal of Electronic imaging*, vol. 11, pp. 206–223, 2002.
- [36] A. M. Eskicioglu and P. S. Fisher, "Image quality measures and their performance," *IEEE Transactions on Communications*, vol. 43, pp. 2959–2965, 1995.
- [37] A. M. Eskicioglu, "Application of multidimensional quality measures to reconstructed medical images," *Optical Engineering*, vol. 35, pp. 778-785, 1996.
- [38] J. Hu, T. Jiang, Z. Cui, and Y. Hou, "Design of UWB pulses based on Gaussian pulse," in *Nano/Micro Engineered and Molecular Systems, 2008. NEMS 2008. 3rd IEEE International Conference on*, 2008, pp. 651-655.

- [39] A. Thakre and A. Dhenge, "Selection of pulse for ultra wide band communication (UWB) system," *International Journal of Advanced Research in Computer and Communication Engineering*, vol. 1, pp. 683-686, 2012.
- [40] C. E. Shannon, "Communication in the presence of noise," *Proceedings of the IRE*, vol. 37, pp. 10-21, 1949.
- [41] M. Bertero and P. Boccacci, *Introduction to Inverse Problems in Imaging*. Bristol, UK: Institute of Physics Publishing, 1998.

## Chapter 3

### Principle and Simulations of UWB Noise Radar Tomographic System

#### 3.1 Overview

Noise radar has been developed and refined for covert detection and imaging applications over the past few decades due to several advantages, such as low probability of interception (LPI) [1], electronic countermeasure (ECM) [2], and relatively simple hardware configurations [3]. Further, UWB noise radar has achieved high-resolution detection and imaging in foliage penetration (FOPEN) imaging [4-5], and through-wall imaging (TWI) [6-7] by employing an ultra-wide bandwidth.

The main advantage of transmitting a random noise waveform is to covertly detect and image a target without alerting the presence of radar system. Such LPI characteristic of the noise radar is achieved by using a random noise waveform, which is constantly varying and never repeats itself exactly [8]. The random noise waveform herein is mathematically defined as discrete time wide-sense stationary (WSS) and ergodic random process, and a sequence of independent and identically distributed random variable drawn from a normal distribution,  $N(0, \sigma^2)$ . Also, the power spectral density (PSD) of WGN waveform is ideally a nonzero constant for all frequencies. In practical situations, however, the PSD of the random noise waveform may not be uniform across the wide frequency ranges because a finite number of random noise amplitude samples must be chosen for WGN waveform generation. In order to bypass such a shortcoming, multiple sequences of iid noise waveforms are transmitted to flatten the spectral density without changing the mean and variance [9].

Radar tomography is emerging as a powerful imaging technique for obtaining high-resolution images of targets [10]. The principle of tomography is to characterize the material property profiles of the target objects in the frequency domain, reconstructing specific scatters within the interrogation medium by solving the inverse scattering problem [11]. Since the frequency behavior of the electrical parameters of the target object due to the illuminating electromagnetic fields depends on the frequency used in the system, UWB radar imaging clearly provides advantages over single or narrow band frequency operation in terms of resolution and accuracy. Furthermore, transmitting random noise waveform inherits the aforementioned advantages of noise radar.

This chapter focuses on the principle and numerical simulation results of tomographic imaging of various target scenarios using UWB noise radar. Multiple iid UWB noise waveforms over 3GHz to 5GHz frequency range are transmitted to obtain the tomographic images of rotating cylindrical objects. In section 3.2, theoretical analysis of the image reconstruction for a bistatic imaging radar system with a two-dimensional rotating cylinder using Fourier diffraction theorem under the assumption of plane wave illumination is presented. The numerical simulation results of diffraction tomography using UWB random noise waveforms are presented in section 3.3. Conclusions are presented in section 3.4.

### **3.2 Formulation of the Scattering Properties**

The top view of two-dimensional backward scattering geometry for a cylindrical object is shown in Figure 3-1. The incident  $z$ -polarized plane wave is illuminated from  $-x$  direction. The receiver spacing,  $\Delta y$ , and the frequency sampling intervals,  $\Delta f$ , are calculated accordingly to avoid aliasing using (2.8) and (2.9) from section 2.3. A linear receiving array is located at  $x = -d$  from the center of the object, collecting scattered field for reconstruction of the object image.

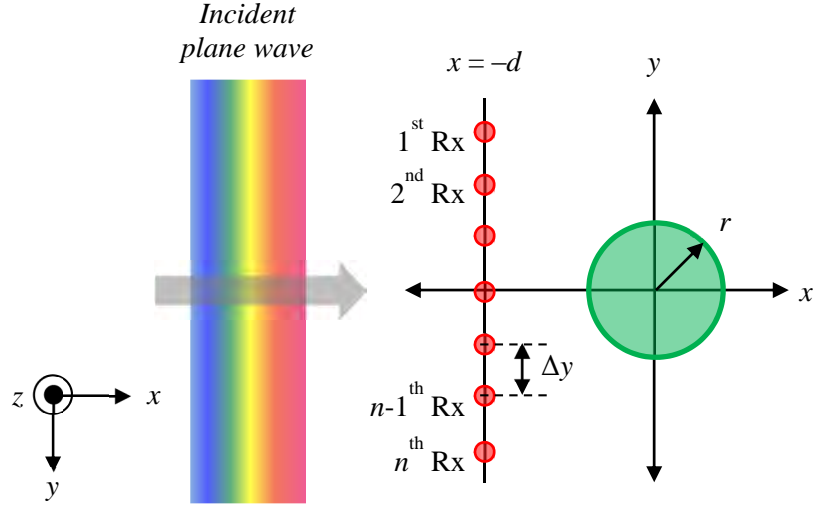


Figure 3-1. Two-dimensional backward scattering geometry for a cylindrical object. Red dots and green circle represent a linear receiving array and the target object, respectively.

The incident  $z$ -polarized plane wave of the white Gaussian noise waveform for  $N$  discrete frequencies takes the form

$$\begin{aligned} E_i(k_n, \vec{r}) &= \hat{z} \left( E_1 e^{-jk_1 \hat{x} \cdot \vec{r}} + E_2 e^{-jk_2 \hat{x} \cdot \vec{r}} + \dots + E_N e^{-jk_N \hat{x} \cdot \vec{r}} \right) \\ &= \hat{z} \sum_{n=1}^N E_n e^{-jk_n \hat{x} \cdot \vec{r}} \\ H_i(k_n, \vec{r}) &= -\hat{y} \cdot \frac{1}{\eta} \cdot E_n e^{-jk_n \hat{x} \cdot \vec{r}} \end{aligned} \quad (3.1)$$

where  $k_n = \omega_n / c$  is the wavenumber,  $\eta$  is the intrinsic impedance in free space, and  $E_n$  is the field amplitude of the transmitted white Gaussian noise waveform at each discrete frequency of interest. We start the analysis from a single frequency and develop the process for  $N$  multiple frequencies by summing up the analysis results for  $N$ . The entire analysis must be repeated for  $K$  times when  $K$  multiple sequences of iid noise waveforms are transmitted.

In this chapter, the target object is assumed to be a dielectric cylinder of the complex permittivity  $\varepsilon(\vec{r})$ , and the object is surrounded by free space. The incident plane wave denoted in (3.1) induces an equivalent electric current distribution, and is defined as

$$J_{eq,\text{dielectric}}(k_n, \vec{r}) = j\omega[\varepsilon(\vec{r}) - \varepsilon_0]E(k_n, \vec{r}). \quad (3.2)$$

$E(k_n, \vec{r})$  in (3.2) is the total field due to the presence of the dielectric object, and expressed as the sum of the incident field and the scattered field, that is,

$$E(k_n, \vec{r}) = E_i(k_n, \vec{r}) + E_s(k_n, \vec{r}). \quad (3.3)$$

The general form of the scattered field  $E_s(k_n, \vec{r})$  created by the equivalent induced current is expressed as

$$E_s(k_n, \vec{r}) = -j\omega\mu_0 \int_S J_{eq}(k_n, \vec{r}') \cdot G(\vec{r} - \vec{r}') d\vec{r}' \quad (3.4)$$

where  $S$  is the boundary of scatterer, and  $G(\vec{r} - \vec{r}')$  is the two-dimensional Green's function defined as

$$G(\vec{r} - \vec{r}') = \frac{1}{4j} H_0^{(2)}(k_n(\vec{r} - \vec{r}')) \quad (3.5)$$

where  $H_0^{(2)}$  is the zeroth-order Hankel function of the second kind.

For the dielectric cylinder, the first-order Born approximation is assumed to be valid [12]. In this case, the  $z$ -polarized scattered field,  $u_{s,\text{dielectric}}$ , at the receivers at  $x = -d$ , is given by

$$\begin{aligned} u_{s,\text{dielectric}}(k_n, x = -d, y) &= \hat{z} \cdot E_{s,\text{dielectric}}(k_n, x = -d, y) \\ &= k_n^2 E_n \iint [\varepsilon_r(\vec{r}') - 1] e^{-jk_n \hat{z} \cdot \vec{r}'} G(\vec{r} - \vec{r}') d^2 \vec{r}'. \end{aligned} \quad (3.6)$$

where  $\varepsilon_r$  is the complex relative dielectric constant ( $\varepsilon_r = \varepsilon / \varepsilon_0$ ). The general form of the  $z$ -polarized scattered field,  $u_s$ , is written for the simplicity, that is,

$$u_s(k_n, x = -d, y) = \psi \iint o(\vec{r}') e^{-jk_n \hat{z} \cdot \vec{r}'} G(\vec{r} - \vec{r}') d^2 \vec{r}' \quad (3.7)$$

where  $\psi$  and  $o(\vec{r}')$  represent the scaling factor outside the integral and the scattering object function of the target object, respectively. For a PEC object,  $\psi$  and  $o(\vec{r}')$  are  $jk_n E_n$  and  $[2\hat{n}(\vec{r}') \cdot \hat{x}\delta(S(\vec{r}'))]$ , respectively, as previously expressed in (2.15) and (2.16) from section 2.3. For a dielectric object,  $\psi$  and  $o(\vec{r}')$  are  $k_n^2 E_n$  and  $[\varepsilon_r(\vec{r}') - 1]$ , respectively, as given in (3.6). The scattering object function is considered to be the electrical contrast between the target object and free space.

By using the plane wave expansion of the Green's function [13], the one-dimensional Fourier transform of the scattered field,  $\tilde{U}_s$ , is given by

$$\tilde{U}_s(k_n, x = -d, k_y) = \frac{-j\psi}{2\gamma} e^{-j\gamma d} \tilde{O}(-\gamma - k_n, k_y) \quad (3.8)$$

where

$$\gamma = \begin{cases} \sqrt{k_n^2 - k_y^2} & \text{as } |k_y| \leq k_n \\ -j\sqrt{k_y^2 - k_n^2} & \text{as } |k_y| > k_n \end{cases}. \quad (3.9)$$

If we define  $k_x = -\gamma - k_n$ , the scattering object function in the Fourier-domain,  $\tilde{O}(k_x, k_y)$ , is a two-dimensional Fourier transform of the scattering function:

$$\tilde{O}(k_x, k_y) = \iint o(x, y) e^{-j(k_x x + k_y y)} dx dy. \quad (3.10)$$

From (3.9), the arguments of  $\tilde{O}(k_x, k_y)$  are related by

$$(k_x + k_n)^2 + k_y^2 = k_n^2. \quad (3.11)$$

Equations (3.8) and (3.11) show that as a two-dimensional scattering object is illuminated by a plane wave at the frequency  $\omega_n$ , the one-dimensional Fourier transform of the scattered field yields a semicircle centered at  $(0, -k_n)$  with radius  $k_n$  in the two-dimensional Fourier space, which relates to the Fourier diffraction theorem described in [14].

The scattering object function,  $o(x, y)$ , of the target is imaged in rectangular coordinates after performing the two-dimensional inverse Fourier transform of (3.10). With the multiple  $N$  frequency data stepped from  $k_1$  to  $k_N$ , the radius of  $\tilde{O}(k_x, k_y)$  in the Fourier-domain changes accordingly, and  $N$  sets of the scattering object function enhance the resolution and accuracy of the image [15-16].

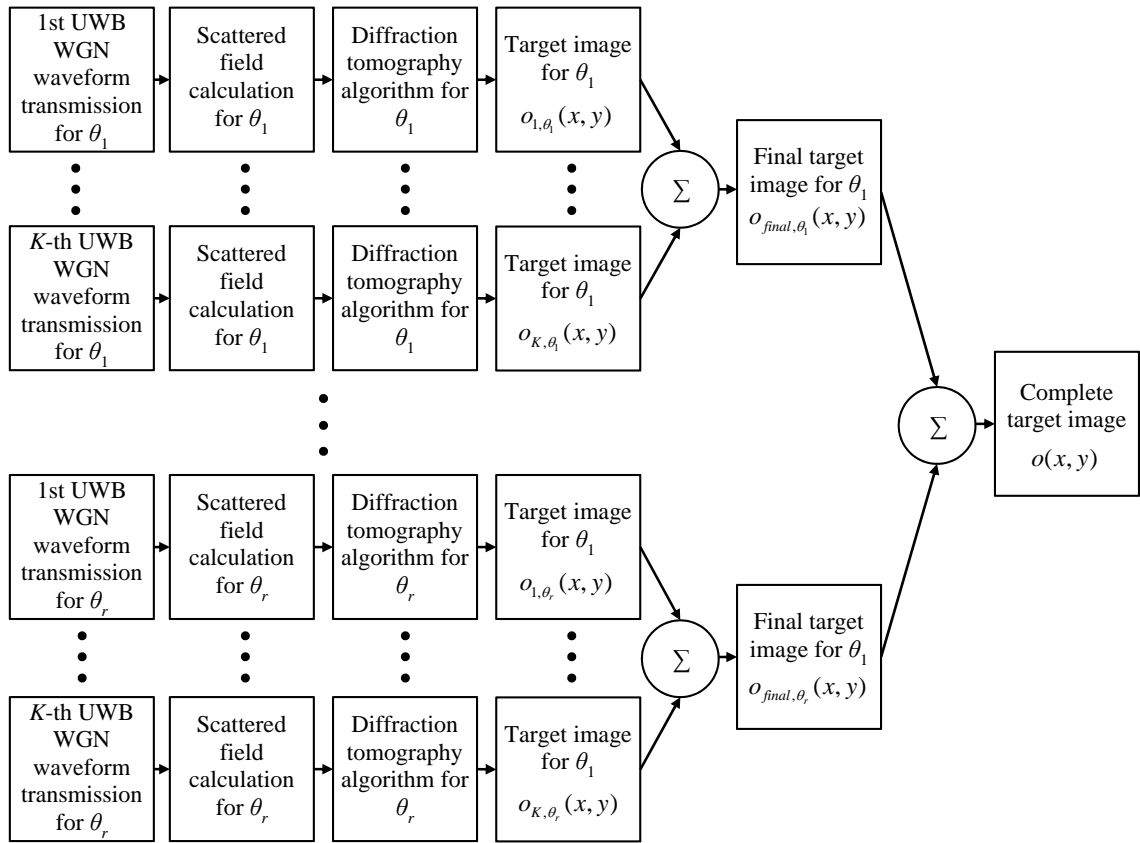


Figure 3-2. The image reconstruction method with  $K$  multiple iid WGN transmitted waveforms for a sequentially rotated object using diffraction tomography.

As the object is sequentially rotated with respect to the rotational axis for the value of rotational angle  $\theta$ , the corresponding scattering object function at the angle  $\theta$  is obtained. The complete two-dimensional tomographic image of the target is reconstructed via computing the

sum of all formed images at each rotational angle. A block diagram shown in Figure 3-2 displays the tomographic image reconstruction method for multiple transmitted iid noise waveforms for a sequentially rotated object using diffraction tomography.

### 3.3 Numerical Simulation Results

#### 3.3.1 Image quality measure

As discussed in chapter 2, the image quality is determined by various factors such as the number of transmissions of iid noise waveforms and the number of random amplitude samples of the transmitted noise waveform. In this chapter, the image quality of the complete tomographic image must be quantitatively analyzed for different values of the rotational angle since the complete tomographic image is achieved based on the rotation of the target object.

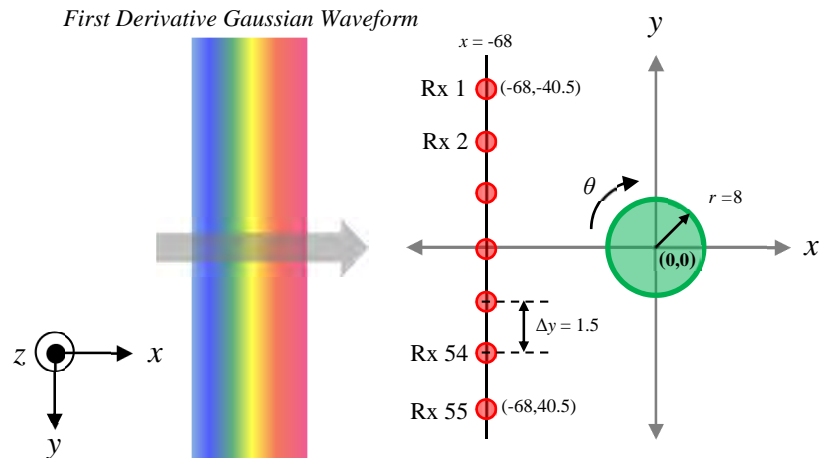


Figure 3-3. Two-dimensional backward scattering simulation geometry for a cylindrical conducting object. The PEC cylinder with a radius of 8 cm is located at (0 cm, 0 cm), and a linear receiving array is located 68 cm away from the center of the object.

Figure 3-3 shows the two-dimensional backward scattering geometry with a single cylindrical conducting object. The PEC cylinder with a radius of 8 cm is located at (0 cm, 0 cm), and the cylinder is assumed to be infinitely long along the  $z$ -axis. The scattered field is uniformly sampled at receiving array Rx1 through Rx55 with frequency swept within the frequency ranges from 3–5 GHz. The locations of Rx1 and Rx55 are at (-68 cm, -40.5 cm) and (-68 cm, 40.5 cm), respectively, and the receiver spacing is set to 1.5 cm.

After scattered field data are collected at all receiving array Rx1 through Rx55, the object is rotated with respect to the rotational axis (0 cm, 0 cm) for the value of rotational angle  $\theta$ . The simulation repeats until the object is fully rotated for 360°, and the complete scattering data for two-dimensional tomographic image of the target are obtained. The minimum rotational angle  $\theta$  is 1.8°, which is the controllable rotational angle of the turntable for the experiment. The value of  $\theta$  varies from 3.6° to 54° to determine the optimum rotational angle by calculating mean square error (MSE).

MSE is the cumulative mean squared error between the corresponding pixels of the reference images and the reconstructed images. MSE is defined as

$$\text{MSE} = \frac{1}{MN} \sum_{m=0}^{M-1} \sum_{n=0}^{N-1} [R(x_m, y_n) - S(x_m, y_n)]^2 \quad (3.12)$$

where  $R(x_m, y_n)$  and  $S(x_m, y_n)$  represent the value of each pixel of the reference image and reconstructed tomographic images based on the transmitted waveform, respectively, and  $M$  and  $N$  are the pixel dimensions of images. The first derivative Gaussian waveform with a pulse width of 0.225 ns is transmitted for all MSE calculations. As shown in Figure 3-4, the frequency response of the transmitted Gaussian waveform in the ranges of 3–5 GHz is relatively flat.

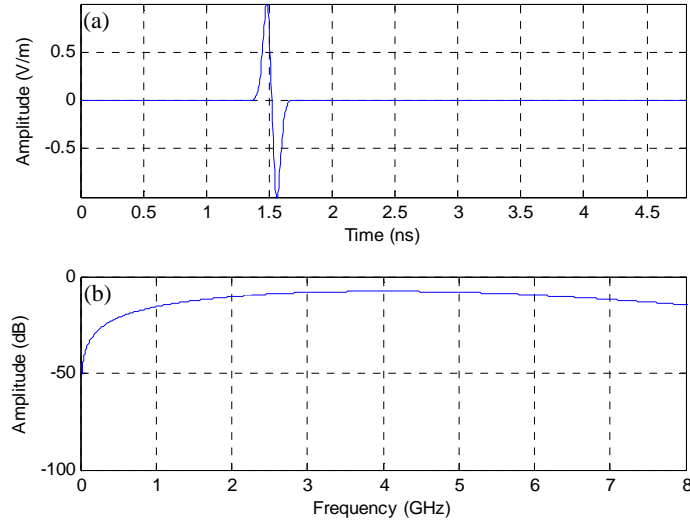


Figure 3-4. (a) The first derivative Gaussian input waveform with a pulse width of 0.225 ns. (b) The frequency spectrum of the first derivative Gaussian input waveform shown in Figure 3-4(a). The frequency spectrum range is displayed from DC to 8 GHz only

Figure 3-5 shows the tomographic image of the cylinder with a rotational angle of  $1.8^\circ$ , which can be considered as a reference image to measure the deviations of image quality when the value of the rotational angle changes.

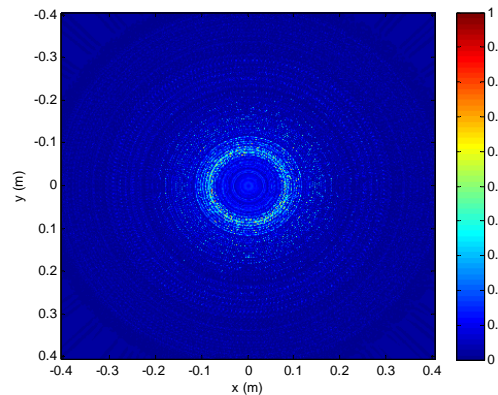


Figure 3-5. The reference tomographic image of the circular PEC cylinder shown in Figure 3-3 for  $\theta = 1.8^\circ$ .

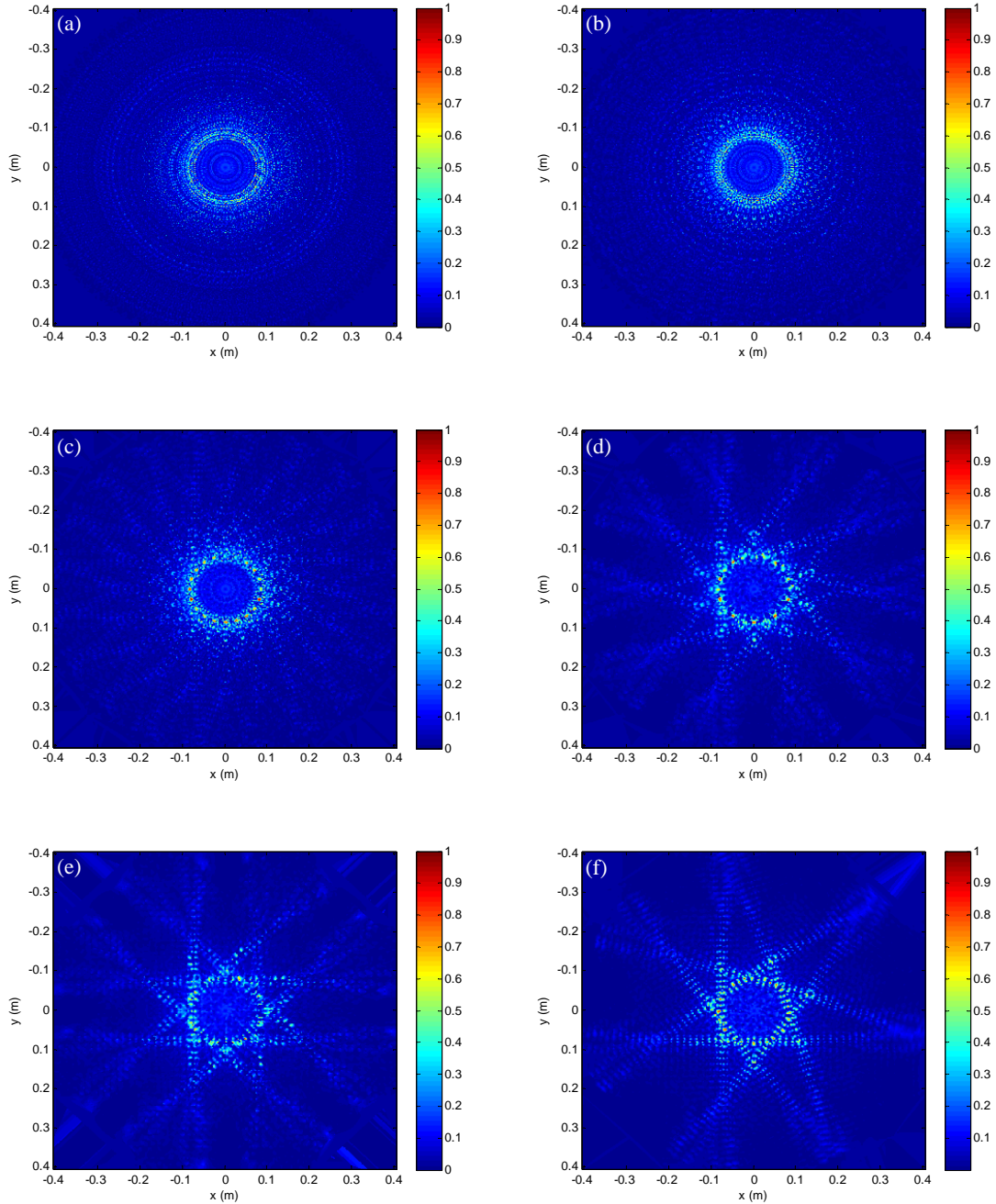


Figure 3-6. Tomographic images of the circular PEC cylinder with 6 different rotational angles: (a)  $\theta = 3.6^\circ$ , (b)  $\theta = 9^\circ$ , (c)  $\theta = 18^\circ$ , (d)  $\theta = 36^\circ$ , (e)  $\theta = 45^\circ$ , and (f)  $\theta = 54^\circ$ .

Figure 3-6 shows the set of 6 tomographic images when the rotational angle  $\theta$  varies from  $3.6^\circ$  to  $54^\circ$ . As shown in Figure 3-6, the successful tomographic images of the circular

cylindrical object for various rotational angles are achieved until the value of the rotational angle  $\theta$  is set to  $36^\circ$ . For large rotational angles, i.e.,  $\theta = 45^\circ$  and  $\theta = 54^\circ$ , the tomographic images of the object become blurry and slightly inaccurate by visual inspection because the arc of the cylinder cannot be precisely achieved due to the limited number of the linear receiving array and pixels of the formed images [17].

MSE vs. the rotational angle  $\theta$  is plotted in Figure 3-7. Such quantitative analysis concludes that the image quality decreases as the value of rotational angle  $\theta$  increases [18]. All images shown in Figure 3-5 and Figure 3-6 are reconstructed based on numerical simulations without any consideration of unwanted additive noise, that is, the signal-to-noise ratio (SNR) is equal to infinity. Thus, MSE purely depends on the value of rotational angle  $\theta$ .

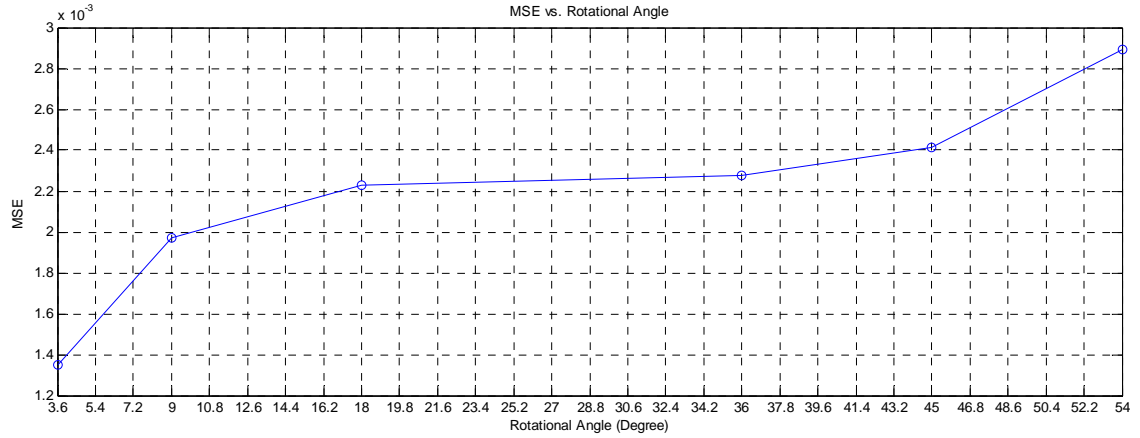


Figure 3-7. MSE vs. rotational angle for the circular PEC cylinder simulation. MSE increases as the value of the rotational angle  $\theta$  increases.

### 3.3.2 Multiple transmitted iid WGN waveforms and rotational angle

As discussed in the previous section, the tomographic image of the scattered object at each rotational angle  $\theta$  is reconstructed via sum of all  $K$  discrete images for  $K$ -th iid transmitted

UWB noise waveforms. The discrete image at the rotational angle  $\theta$  is obtained based on the corresponding scattering object function at the angle  $\theta$ , and the complete image of the target cylinder is achieved by plotting all discrete images in the single image plane as shown in Figure 3-2. For scattered field and diffraction tomography simulations with multiple iid WGN waveforms, 10 iid UWB WGN waveforms over a frequency range from 3 GHz to 5 GHz are generated with 500 random amplitude samples drawn from  $N(0, \sigma^2)$ , that is,  $K = 10$ , and they are sequentially transmitted for backward scattered field calculations. The rotational angle  $\theta$  is set to 9° based on the MSE analysis displayed in Figure 3-7 such that 40 discrete images are obtained after full 360° rotation. The complete tomographic image of the target is achieved by combining 40 discrete images into one single image. Table 3-1 shows the list of target objects for the numerical simulations.

Table 3-1. Target objects imaged by the numerical simulations.

Object Material	Object Description	Dimension	
PEC	Circular Cylinder	20 cm diameter (7.9" diameter)	Height of the objects are assumed to be infinitely long
	Square Box	20 cm × 20 cm (7.9" × 7.9")	
	Triangular Prism	20 cm side (7.9" side)	
Dielectric $\epsilon_r = 5.8 - j0.75$	Circular Cylinder	16 cm diameter (6.3" diameter)	
	Square Box	16 cm × 16 cm (6.3" × 6.3")	

### 3.3.3 Tomographic image with multiple transmitted iid WGN waveforms for a circular PEC cylinder

As shown in Figure 3-8, two-dimensional backward scattering geometry with a circular PEC cylindrical object is simulated with 10 iid UWB WGN waveforms. The cylinder with a radius of 10 cm is located at (0 cm, 0 cm), and the height of the cylinder is assumed to be infinitely long along the  $z$ -axis. The locations of Rx1 and Rx55 are at (-68 cm, -40.5 cm) and (-68 cm, 40.5 cm), respectively, and the receiver spacing is set to 1.5 cm in order to avoid any aliasing.

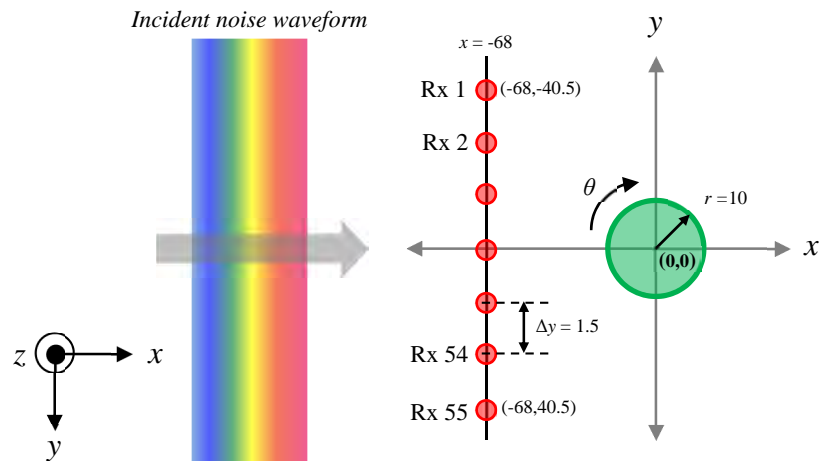


Figure 3-8. Two-dimensional backward scattering simulation geometry for a circular PEC cylinder. The cylinder with a radius of 10 cm is located at (0 cm, 0 cm), and a linear receiving array is located 68 cm away from the center of the object.

The scattered field is uniformly sampled at receiving array Rx1 through Rx55 with frequency swept within the frequency ranges from 3–5 GHz. When the data acquisition is completed for all receiving elements Rx1 through Rx55, the object is rotated at 9° with respect to the origin (0 cm, 0 cm). The simulation repeats until the object is fully rotated for 360°.

Four tomographic images of the circular PEC cylinder shown in Figure 3-8 with 10 transmitted iid WGN waveform are shown in Figure 3-9(a), Figure 3-9(b), Figure 3-9(c) and Figure 3-9(d) when 1, 3, 7 and 10 noise waveforms are transmitted, respectively.

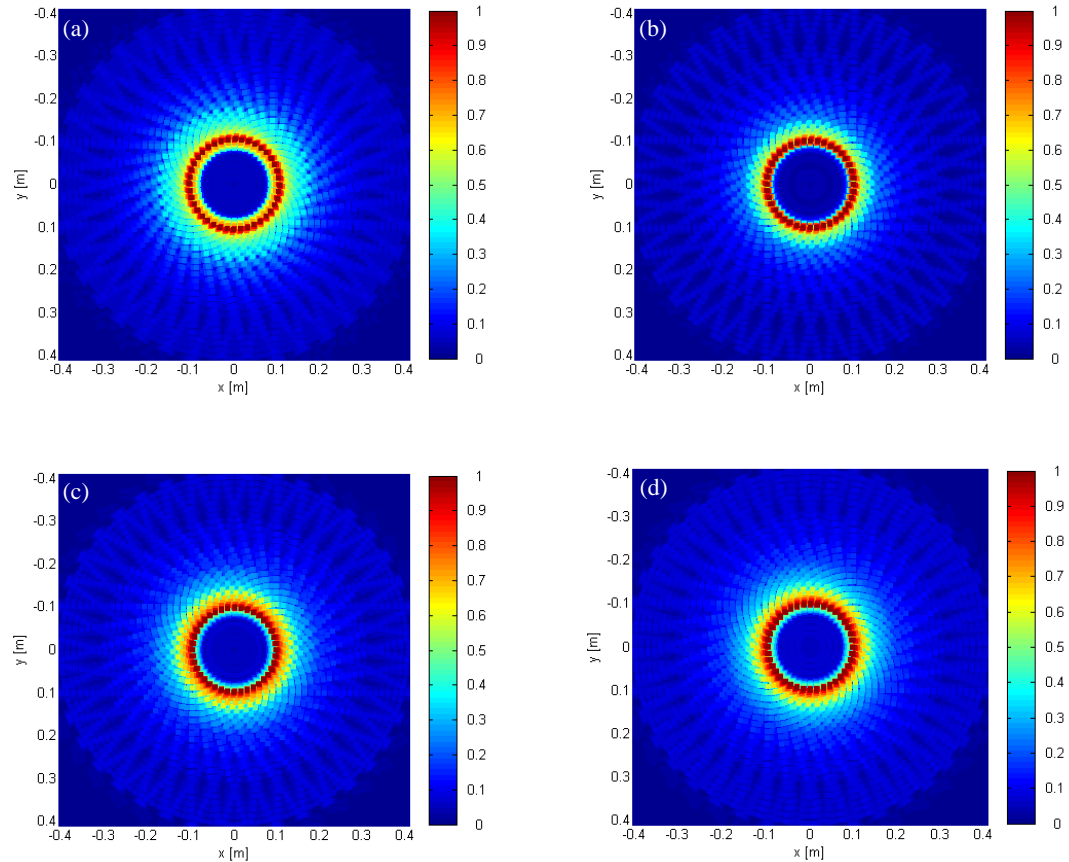


Figure 3-9. Two-dimensional tomographic image of a single PEC cylinder with a radius of 10 cm located at (0 cm, 0 cm) after summing and averaging process based on (a) one transmitted WGN waveform, (b) three transmitted WGN waveforms, (c) seven transmitted WGN waveforms, and (d) all ten transmitted WGN waveforms. The rotational angle is  $9^\circ$ .

### 3.3.4 Tomographic image with multiple transmitted iid WGN waveforms for a square PEC box

Figure 3-10 shows the two-dimensional backward scattering geometry with a square PEC box located at (0 cm, 0 cm). The length of each side of the square ( $a$ ) is 20 cm, and the height of the box is assumed to be infinitely long along the  $z$ -axis. The locations of all 55 receivers, the parameters for receiver spacing,  $\Delta y$ , and the rotational angle,  $\theta$ , are identical to the previous case.

In order to generate the complete tomographic image of the square PEC box shown in Figure 3-10, 10 iid random noise waveforms are sequentially transmitted. Figure 3-11(a), Figure 3-11(b), Figure 3-11(c) and Figure 3-11(d) display four tomographic images of the square PEC box when 1, 3, 7 and 10 noise waveforms are transmitted, respectively.

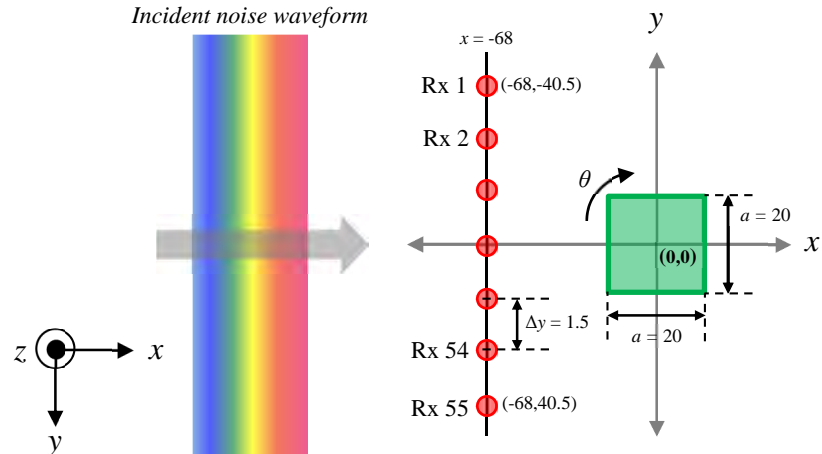


Figure 3-10. Two-dimensional backward scattering simulation geometry for a square PEC box with a length of 20 cm. The box is located at (0 cm, 0 cm), and a linear receiving array is located 68 cm away from the center of the object.

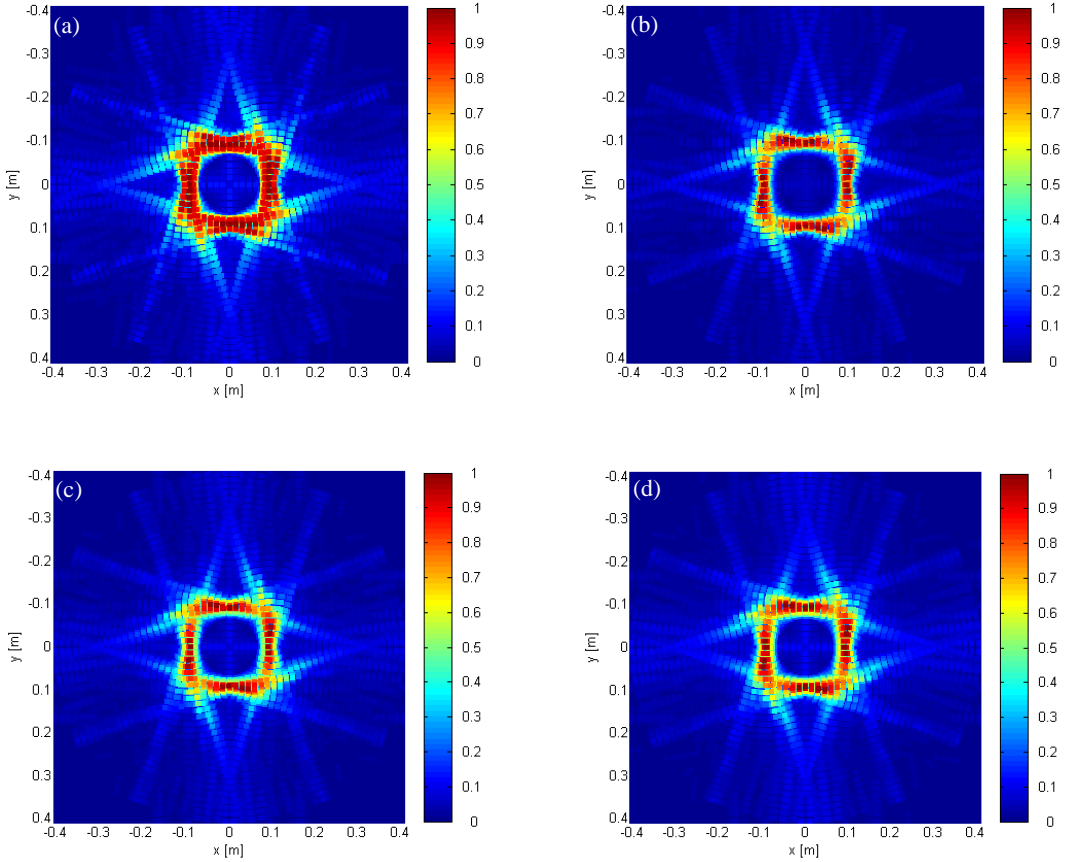


Figure 3-11. Two-dimensional tomographic image of a square PEC box with a length of 20 cm located at (0 cm, 0 cm) after summing and averaging process based on (a) one transmitted WGN waveform, (b) three transmitted WGN waveforms, (c) seven transmitted WGN waveforms, and (d) all ten transmitted WGN waveforms. The rotational angle is 9°.

### 3.3.5 Tomographic image with multiple transmitted iid WGN waveforms for an equilateral triangular PEC prism

Backward scattering simulation geometry with an equilateral triangular PEC prism is shown in Figure 3-12. The triangular prism is located at (0 cm, 0 cm), and the length of each side of the triangle ( $a$ ) is 20 cm. The target object is also considered as an infinitely long prism along the  $z$ -axis. Other simulation parameters, such as the position of receivers, the parameters for receiver spacing, and the rotational angle, remain unchanged. Also, four tomographic images of the equilateral triangular PEC prism with 1, 3, 7 and 10 transmitted iid noise waveforms are shown in Figure 3-13(a), Figure 3-13(b), Figure 3-13(c), and Figure 3-13(d), respectively.

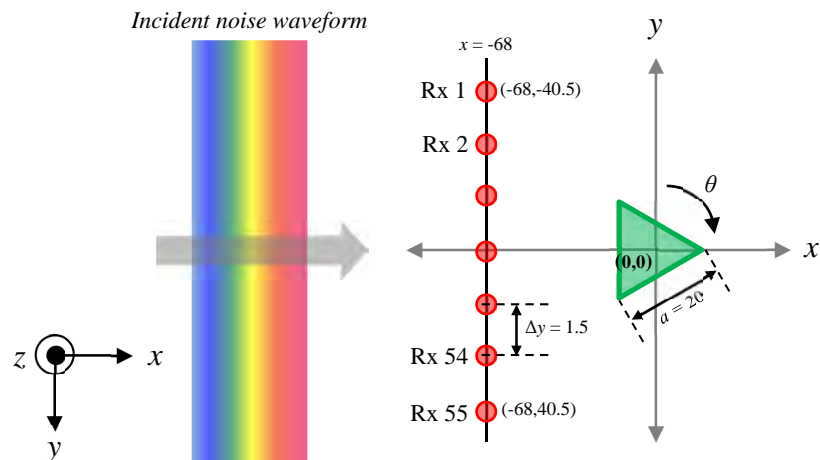


Figure 3-12. Two-dimensional backward scattering simulation geometry for an equilateral triangular PEC prism with a length of 20 cm. The prism is located at (0 cm, 0 cm), and a linear receiving array is located 68 cm away from the center of the object.

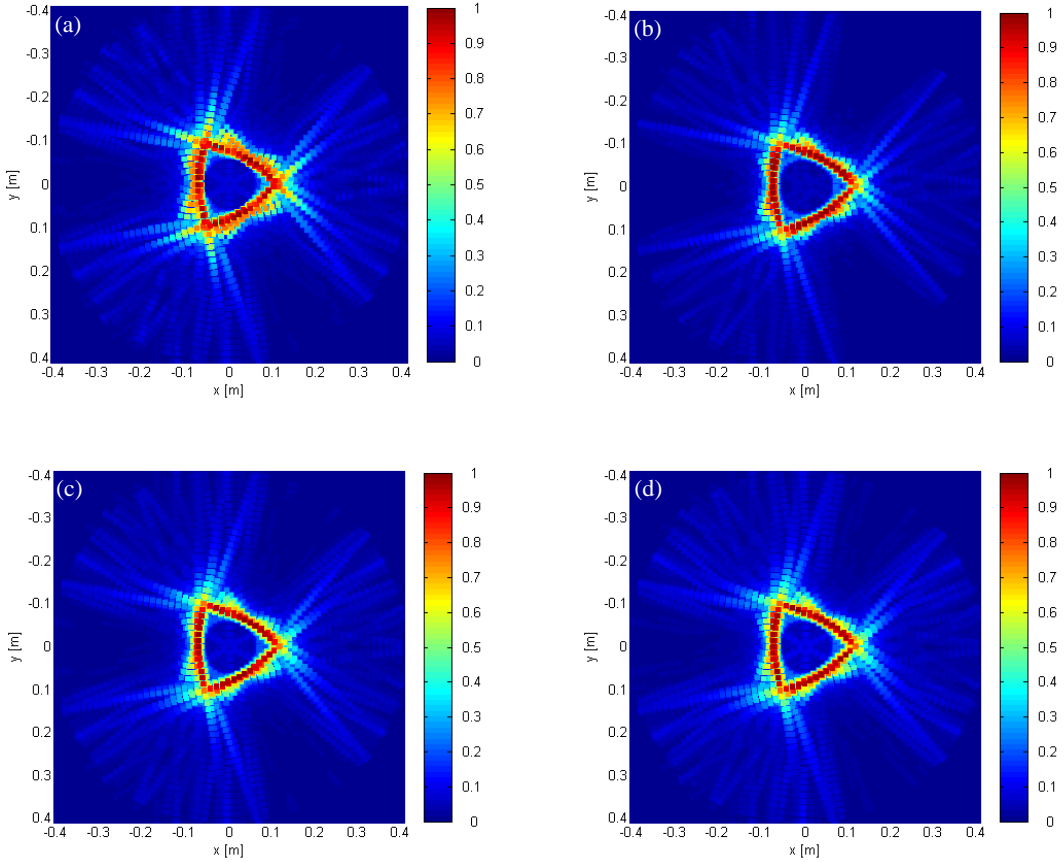


Figure 3-13. Two-dimensional tomographic image of an equilateral triangular PEC prism with a length of 20 cm located at (0 cm, 0 cm) after summing and averaging process based on (a) one transmitted WGN waveform, (b) three transmitted WGN waveforms, (c) seven transmitted WGN waveforms, and (d) all ten transmitted WGN waveforms. The rotational angle is  $9^\circ$ .

### 3.3.6 Tomographic image with multiple transmitted iid WGN waveforms for a circular dielectric cylinder

Figure 3-14 shows two-dimensional backward scattering geometry with a circular dielectric cylinder is simulated with 10 iid UWB WGN waveforms. The circular cylinder with a radius of 8 cm is located at (0 cm, 0 cm), and the height of the cylinder is assumed to be infinitely long along the  $z$ -axis. The locations of Rx1 and Rx55 are at (-68 cm, -40.5 cm) and (-68 cm, 40.5 cm), respectively, and the receiver spacing is set to 1.5 cm in order to avoid any aliasing effect.

The dielectric cylinder is assumed to be a homogeneous concrete block; the real and imaginary values of complex relative permittivity are 5.8 and 0.75, respectively, at the evaluation frequency of 3 GHz [19]. The moisture contents and surface roughness of the dielectric cylinder are not considered for the simulations.

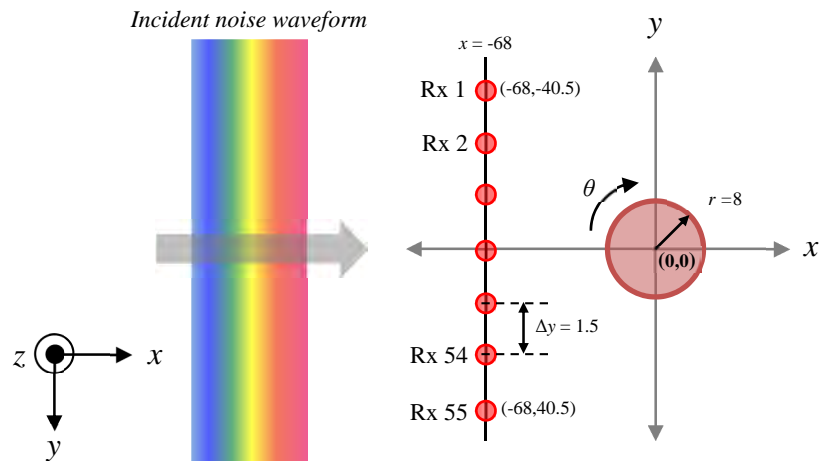


Figure 3-14. Two-dimensional backward scattering simulation geometry for a circular dielectric cylinder with a radius of 8 cm. The cylinder is located at (0 cm, 0 cm), and a linear receiving array is located 68 cm away from the center of the object.

The scattered field is uniformly sampled at receiving elements Rx1 through Rx55 with frequency swept within the frequency ranges from 3–5 GHz. When the data acquisition is completed for all receiving array Rx1 through Rx55, the object is rotated at 9° with respect to the rotational axis (0 cm, 0 cm). The simulation repeats until the object is fully rotated for 360°.

Four tomographic image of the dielectric circular cylinder based on 10 transmitted iid WGN waveform are shown in Figure 3-15(a), Figure 3-15(b), Figure 3-15(c) and Figure 3-15(d) when 1, 3, 7 and 10 noise waveforms are transmitted, respectively.

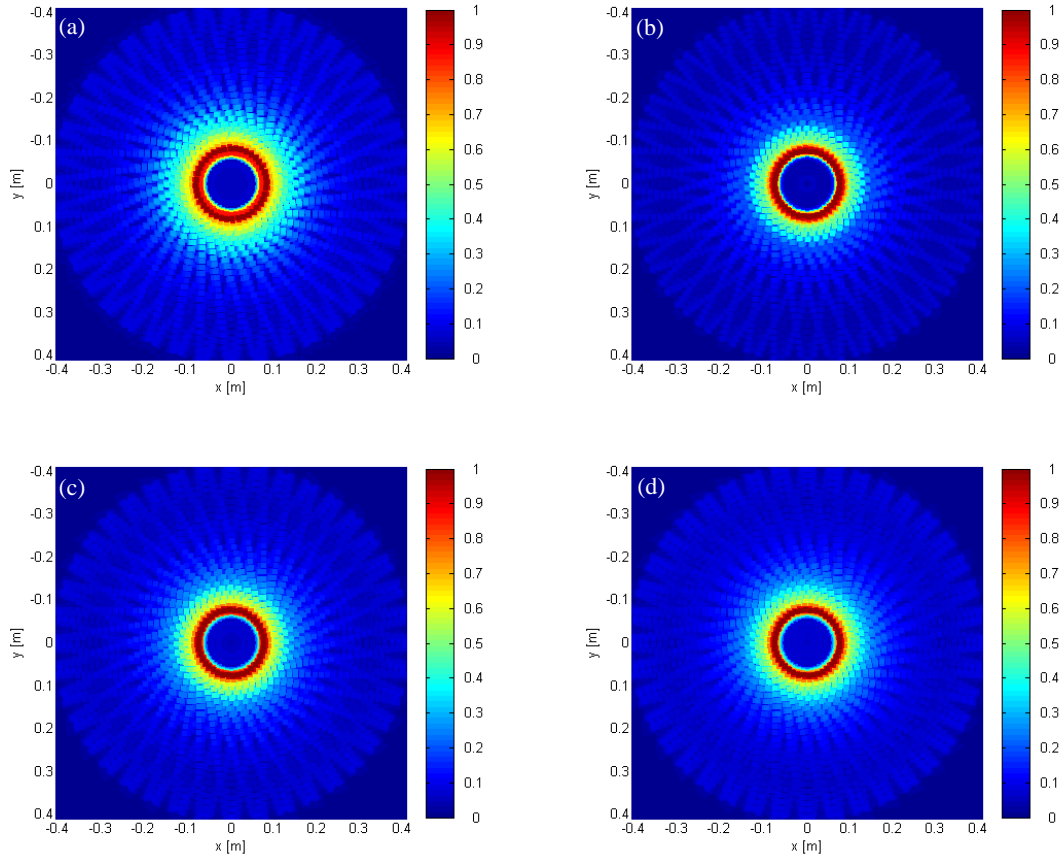


Figure 3-15. Two-dimensional tomographic image of a single circular dielectric cylinder with a radius of 8 cm located at (0 cm, 0 cm) after summing and averaging process based on (a) one transmitted WGN waveform, (b) three transmitted WGN waveforms, (c) seven transmitted WGN waveforms, and (d) all ten transmitted WGN waveforms. The rotational angle is 9°.

### 3.3.7 Tomographic image with multiple transmitted iid WGN waveforms for a square dielectric box

Figure 3-16 shows the two-dimensional backward scattering geometry with a square dielectric box located at (0 cm, 0 cm). The length of each side of the square is 16 cm, and the height of the box is assumed to be infinitely long along the  $z$ -axis. The material properties of the dielectric square box, i.e., the complex dielectric constant, are identical to the previous dielectric circular cylinder case.

In order to generate the complete tomographic image of the dielectric square box, 10 iid random noise waveforms are transmitted. Figure 3-17(a), Figure 3-17(b), Figure 3-17(c) and Figure 3-17(d) display four tomographic images of the square dielectric box when 1, 3, 7 and 10 noise waveforms are transmitted, respectively.

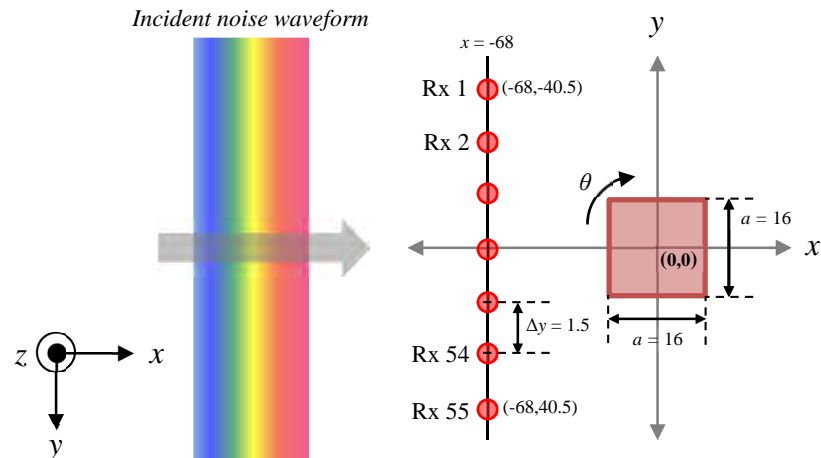


Figure 3-16. Two-dimensional backward scattering simulation geometry for a square dielectric box with a length of 20 cm is located at (0 cm, 0 cm), and a linear receiving array is located 68 cm away from the center of the object.

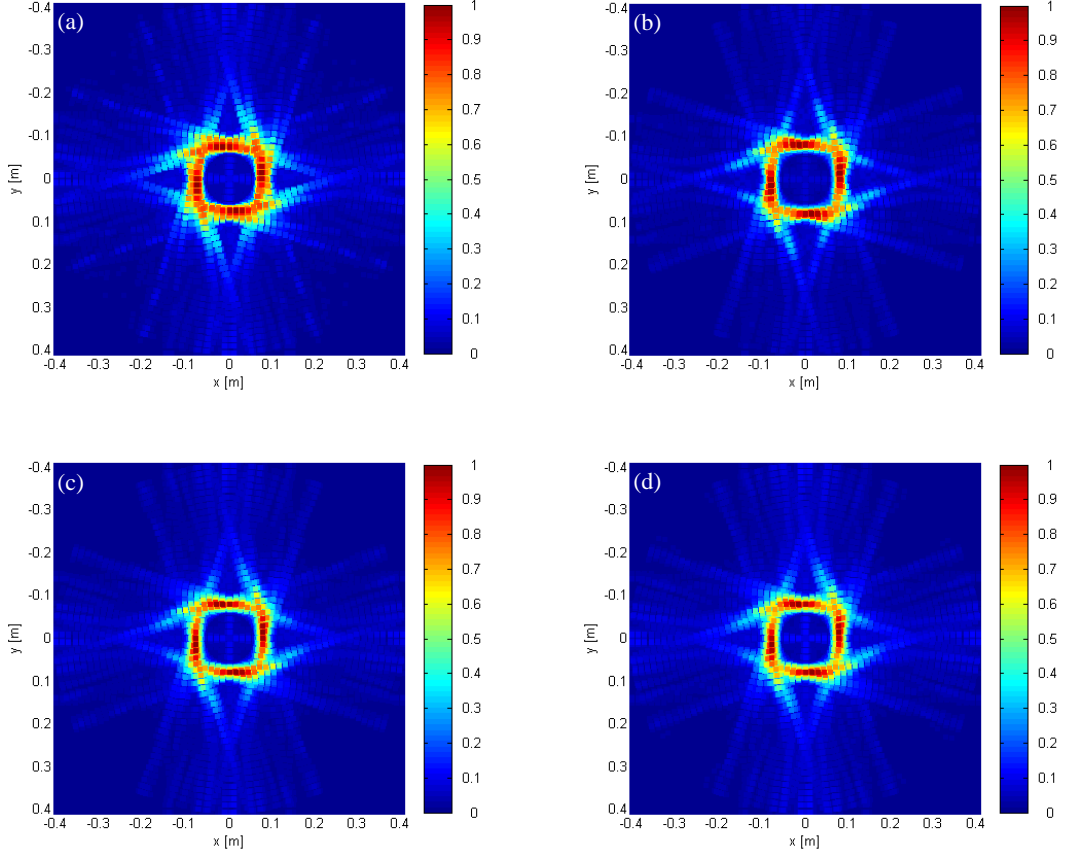


Figure 3-17. Two-dimensional tomographic image of a square dielectric box with a length of 20 cm located at (0 cm, 0 cm) after summing and averaging process based on (a) one transmitted WGN waveform, (b) three transmitted WGN waveforms, (c) seven transmitted WGN waveforms, and (d) all ten transmitted WGN waveforms. The rotational angle is 9°.

### 3.4 Summary

In this chapter, the complete tomographic images of the sequentially rotated objects are successfully achieved with multiple transmissions of iid UWB random noise waveforms. Based on the simulation results, the image of both PEC and dielectric objects are correctly reconstructed. The image quality of the reconstructed images for the rotated object cases depends on the rotational angle. MSE analysis quantitatively explains the relationship between the image quality and different rotational angles. Image quality is noticeably degraded as the value of the rotational

angle increases. Also the multiple transmissions of iid UWB WGN waveforms truly enhance the image quality for the rotated object cases herein. The numerical simulation results shown in this chapter will be compared to the experimental results, which will be presented in the following chapter.

### 3.5 References

- [1] R. M. Narayanan and X. J. Xu, "Principles and applications of coherent random noise radar technology," in *Proc. of SPIE Conf. on Noise in Devices and Circuits*, Santa Fe, NM, 2003, pp. 503-514.
- [2] D. S. Garmatyuk and R. M. Narayanan, "ECCM capabilities of an ultrawideband bandlimited random noise imaging radar," *IEEE Transactions on Aerospace and Electronic Systems*, vol. 38, no. 4, pp. 1243-1255, Oct 2002.
- [3] G. S. Liu, H. Gu, and W. M. Su, "Development of random signal radars," *IEEE Transactions on Aerospace and Electronic Systems*, vol. 35, no. 3, pp. 770-777, Jul 1999.
- [4] X. J. Xu and R. M. Narayanan, "FOPEN SAR imaging using UWB step-frequency and random noise waveforms," *IEEE Transactions on Aerospace and Electronic Systems*, vol. 37, no. 4, pp. 1287-1300, Oct 2001.
- [5] R. M. Narayanan, X. Xu, and J. A. Henning, "Radar penetration imaging using ultra-wideband (UWB) random noise waveforms," *IEE Proceedings-Radar Sonar and Navigation*, vol. 151, no. 3, pp. 143-148, Jun 2004.
- [6] J. Sachs, M. Aftanas, S. Crabbe, M. Drutarovsky, R. Klukas, D. Kocur, T. T. Nguyen, P. Peyerl, J. Rovnakova, and E. Zaikov, "Detection and tracking of moving or trapped people hidden by obstacles using ultra-wideband pseudo-noise radar," *2008 European Radar Conference*, pp. 408-411, 2008.

- [7] R. M. Narayanan, "Through-wall radar imaging using UWB noise waveforms," *Journal of the Franklin Institute-Engineering and Applied Mathematics*, vol. 345, no. 6, pp. 659-678, Sep 2008.
- [8] C. P. Lai and R. M. Narayanan, "Ultrawideband random noise radar design for through-wall surveillance," *IEEE Transactions on Aerospace and Electronic Systems*, vol. 46, no. 4, pp. 1716-1730, Oct 2010.
- [9] H. J. Shin, R. M. Narayanan, and M. Rangaswamy, "Ultrawideband Noise Radar Imaging of Impenetrable Cylindrical Objects Using Diffraction Tomography," *International Journal of Microwave Science and Technology*, vol. 2014, p. 22, 2014.
- [10] L. Jofre, A. Broquetas, J. Romeu, S. Blanch, A. P. Toda, X. Fabregas, and A. Cardama, "UWB tomographic radar imaging of penetrable and impenetrable objects," *Proceedings of the IEEE*, vol. 97, no. 2, pp. 451-464, Feb 2009.
- [11] A. C. Kak, "Computerized tomography with x-ray, emission, and ultrasound sources," *Proceedings of the IEEE*, vol. 67, no. 9, pp. 1245-1272, 1979.
- [12] V. Barthes and G. Vasseur, "An inverse problem for electromagnetic prospection," in *Applied Inverse Problems*. vol. 85, P. Sabatier, Ed., ed: Springer Berlin Heidelberg, 1978, pp. 325-329.
- [13] J.-C. Bolomey and C. Pichot, "Microwave tomography: From theory to practical imaging systems," *International Journal of Imaging Systems and Technology*, vol. 2, pp. 144-156, 1990.
- [14] S. X. Pan and A. C. Kak, "A Computational Study of Reconstruction Algorithms for Diffraction Tomography - Interpolation Versus Filtered Backpropagation," *IEEE Transactions on Acoustics Speech and Signal Processing*, vol. 31, no. 5, pp. 1262-1275, 1983.

- [15] H. J. Shin, R. M. Narayanan, and M. Rangaswamy, "Diffraction Tomography for Ultra-Wideband Noise Radar and Imaging Quality Measure of a Cylindrical Perfectly Conducting Object," in *Proceedings of the 2014 IEEE Radar Conference (RADAR)*, Cincinnati, OH, May 2014, pp. 702–707.
- [16] H. J. Shin, R. M. Narayanan, and M. Rangaswamy, "Ultra-wideband noise radar imaging of cylindrical PEC objects using diffraction tomography," in *Proceedings of the SPIE Conference on Radar Sensor Technology XVIII*, Baltimore, MD, May 2014, pp. 90770J-1–90770J-10.
- [17] H. J. Shin, M. A. Asmuth, R. M. Narayanan, and M. Rangaswamy, "Principle and experimental results of ultra-wideband noise radar imaging of a cylindrical conducting object using diffraction tomography," in *Proceedings of the SPIE Conference on Radar Sensor Technology XIX*, Baltimore, MD, April 2015, pp. 94610V-1–94610V-11.
- [18] H. J. Shin, M. A. Asmuth, R. M. Narayanan, and M. Rangaswamy, "Principle and experimental results of ultra-wideband noise radar imaging of a cylindrical conducting object using diffraction tomography," in *Proceedings of the SPIE Conference on Radar Sensor Technology XIX*, Baltimore, MD, April 2015, pp. 94610V-1–94610V-11.
- [18] M. G. Amin, *Through-the-Wall Radar Imaging*, 1st ed., CRC Press, 2010.

## Chapter 4

### Design and Implementation of UWB Noise Radar Tomographic System

#### 4.1 Overview

Microwave tomography has been developed and refined over the past few decades to obtain high-resolution images of metallic targets and dielectric contrasts embedded within a dielectric medium. The objective of active microwave tomography is to reconstruct the dielectric properties of a body illuminated with microwaves from a measurement of the scattered fields. Conventional microwave tomography systems are based on illuminating the body with a plane wave and measuring the scattering with a linear array of probes. A practical requirement when using this method is the need for mechanical rotation of either the body or the antenna in order to obtain measurements in different views [1]. Every object, when inserted into an electromagnetic field, causes a well-defined field change, and diffraction occurs when the wavelength of the microwave radiation is of the order of the dimension of the object. A one-to-one relationship relating the scattered field to the object complex permittivity can be obtained within the Born approximation, via a Fourier transform using the so-called Fourier Diffraction Theorem [2].

Several hardware systems have been developed and implemented over the years. A microwave tomographic system consisting of 64 circularly arranged electronically scanned antennas, divided into 32 transmitters and 32 receivers, operating at a frequency of 2.45 GHz was developed for biological tissue imaging [3]. A C-system operating at 7.5 GHz was developed for imaging weakly scattering objects, such as paper cylinders [4]. More recently, a two-dimensional UWB microwave imaging system for 3–6 GHz frequency range using 24 antenna elements connected to a vector network analyzer via a  $2 \times 24$  port matrix switch was able to quantitatively reconstruct dielectric objects [5]. Also a time-domain UWB tomographic imaging system

transmitting a differentiated cosine-modulated Gaussian pulse with a carrier frequency of 1 GHz was used to reconstruct plastic phantoms of different sizes and shapes immersed in a tank filled with pipe water [6].

In this chapter, the hardware design and experimental investigation of UWB noise radar tomographic system are discussed. First, implementation of UWB noise radar tomographic system is described in section 4.2. The data acquisition process in UWB noise radar for diffraction tomography and the effective tomographic image processing technique for large sets of collected data samples are proposed in section 4.3. In section 4.4, successful experimental results of various cross-sectional shapes of metallic and dielectric cylindrical targets are presented. Conclusions of the implementation and performance of UWB noise radar tomographic system are discussed in section 4.5.

## 4.2 Implementation of the Hardware System

### 4.2.1 Experimental configuration of UWB noise radar

The entire experiment is sequentially controlled by a desktop computer. The computer is directly connected to the electrical components: an arbitrary waveform generator (AWG) and a digital oscilloscope. Before the data acquisition process begins, the AWG at the transmitter side starts generating the random waveforms based on a given specification such as the number of amplitude samples, frequency bandwidth, and sampling rate. The AWG is designed to transmit the random noise waveform continuously for the duration of the measurement. The digital oscilloscope is configured to collect and save the scattering data at the receiver side.

Also two mechanical components, i.e., a turntable and a linear scanner, are controlled by the desktop computer. For data acquisition, the target object is placed on the turntable, and a

stepper motor of the turntable rotates the object a certain number of degrees. The receiving antenna is mounted on the linear scanner; the antenna moves along the linear scanner and stops at the designated coordinate to collect the data at that point. The receiving antenna is connected directly to the oscilloscope; thus, the oscilloscope acquires time-domain data and then passes the data back to the desktop computer. Figure 4-1 shows the proposed hardware implementation of UWB noise radar to measure the scattering data of the target object in a backward scattering arrangement.

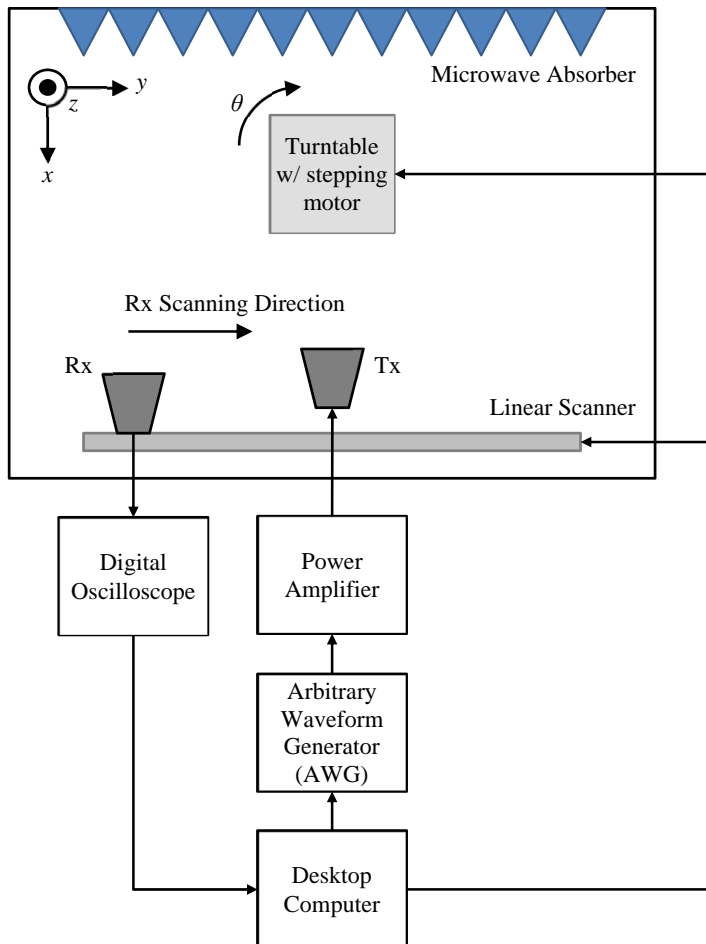


Figure 4-1. Automated UWB noise radar tomographic system.

#### 4.2.2 Transmitter and receiver

The block diagram for the transmitter and the receiver portions of the system are shown in Figure 4-2. The AWG is Agilent M8190A system mounted on a M9602A chassis. For transmit noise waveforms, the AWG generates a bandlimited random noise waveform from 3–5 GHz at an output power of 0 dBm. The gain of ZVE-8G+ with 12 V DC input power across the frequency range of 2–8GHz is plotted in Figure 4-3. The output power ranges of the transmitted bandlimited noise waveform after the amplifier is approximately  $35 \pm 0.5$  dBm because of the tolerance of the gain of ZVE-8G+.

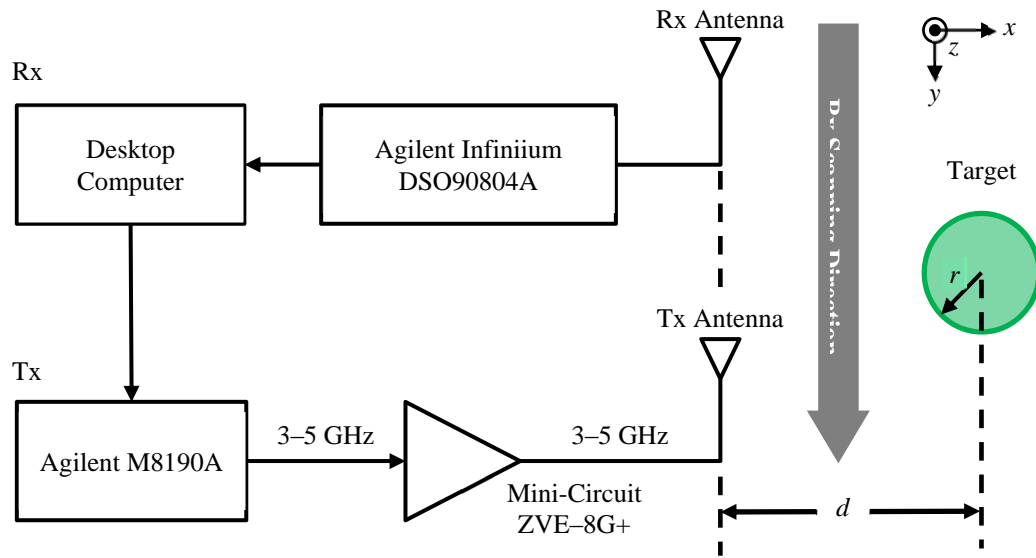


Figure 4-2. Block diagram of transmitter and receiver.

The amplified noise waveform is transmitted through an A-Info dual-polarization horn antenna. The dual-polarized horn antenna operates over the frequency range of 2–18 GHz, and the antenna has a gain of approximately 10 dB over 3–5 GHz operating range. The position of the transmitting antenna is fixed at the center of the backward scattering geometry, but the receiving antenna is designed to move along the linear scanner to collect the scattering data. The

receiving side of the system uses an identical antenna for collecting scattering data. Both transmitting and receiving antenna are installed to measure only vertically polarized scattering data. The receiving antenna is connected to an Agilent Infiniium DSO90804A oscilloscope which has a maximum sampling rate of 40 GSa/s. The oscilloscope then collects the scattering data and then sends it to the computer for tomographic image processing.

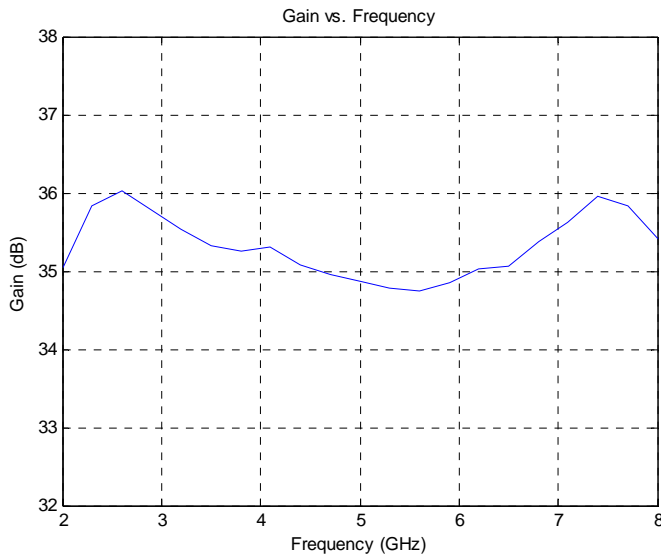


Figure 4-3. The gain vs. frequency plot of Mini-circuit ZVE-8G+.

#### 4.2.3 Turntable and linear scanner

The receiving antenna is placed on a linear scanner in place of an antenna array, as shown in Figure 4-2. The scanner stops at 55 locations to measure the vertically polarized scattering data. Since the length of the scanner is 81 cm, the receiver spacing,  $\Delta y$ , is calculated to be 1.5 cm, satisfying the equation (2.8). Also microwave absorber material is placed behind the target object in order to attenuate signal reflected off of the back wall, as well as to minimize the multipath reflections.

Both metallic and dielectric cylinders with different shapes are measured for tomographic image reconstructions. The metallic objects are constructed from sheets of aluminum. For the dielectric target objects, they are assumed to be homogeneous concrete blocks. The moisture contents and surface roughness of the concrete blocks are not considered for the experiments. The test objects are placed on the center of the turntable one at a time. Table 4-1 shows the target objects for which the tomographic images are presented herein.

Table 4-1. Target objects imaged by the tomographic noise radar system.

Object Material	Object Description	Dimension
Metal	Circular Cylinder	20.3 cm diameter × 40.6 cm height (8" diameter × 16" height)
	Square Box	20.3 cm × 20.3 cm × 61 cm height (8" × 8" × 24")
	Triangular Prism	20.3 cm side × 30.5 cm height (8" side × 12" height)
Concrete	Circular Cylinder	15.2 cm diameter × 30.5 cm height (6" diameter × 12" height)
	Square Block	15.2 cm × 15.2 cm × 28 cm height (6" × 6" × 11")

For the entire measurement process, the receiving antenna stops in order to ensure that the oscilloscope has sufficient amount of time to collect and save scattering data at that position. After data acquisition for all 55 points of data are complete, the linear scanner moves back to its initial position. As the linear scanner is moving back to the first point, the turntable rotates by 9 degrees. The linear scanner repeats the data acquisition for same 55 scanning points as before, and such measurement process are continued until the object has rotated by a full 360 degrees. The turntable is controlled by a stepper motor and is able to rotate in any multiple of 1.8°. Since the rotational angle is defined as 9° based on MSE analysis in Section 3.3, a total of 40 angular

measurement dataset are obtained. The number of scanning points and the angle of rotation were chosen as a tradeoff between data collection time as well as image quality.

#### **4.2.4 Data acquisition and image processing**

Figure 4-4 shows the actual metallic cylinder and the complete experimental hardware configuration with the cylinder. Both the transmitting and the receiving antennas point towards the foam wall. The target object is positioned in the main lobe for the transmitting and the receiving antenna. The data collection process starts with the Gaussian noise waveforms being transmitted to the target object. The transmitted noise waveforms are not identical between each measurement; however, the iid white Gaussian noise waveforms are transmitted for the experiments. Each time the linear scanner stops, the oscilloscope collects a total of 363,000 amplitude samples. As previously described, the turntable rotates 9° after a single line scan has been completed, and the process repeats until the object has fully rotated for 360°. The total data stored of a single target object with complete 360° rotation are in 40×363,000 matrix array for tomographic image processing at a later point in time.

As discussed in the previous chapter, the spectral response of the transmitted random noise waveform is directly related to the image quality. If the oscilloscope collects the insufficient amount of scattering data, an unrecognizable image of the target may be formed due to the fluctuation of the spectrum response. Although a long sample length or the averaging of multiple samples is necessary to achieve a flat frequency spectrum, the data size of 40×363,000 matrix array may not be processed at the same time due to the memory limitations of the desktop computer. For the computational efficiency, each 363,000 point sample is split into  $N$  segments for processing then summed and averaged to create an image. A total of  $N$  images are reconstructed for each rotational angle where the turntable stops, and the final tomographic image

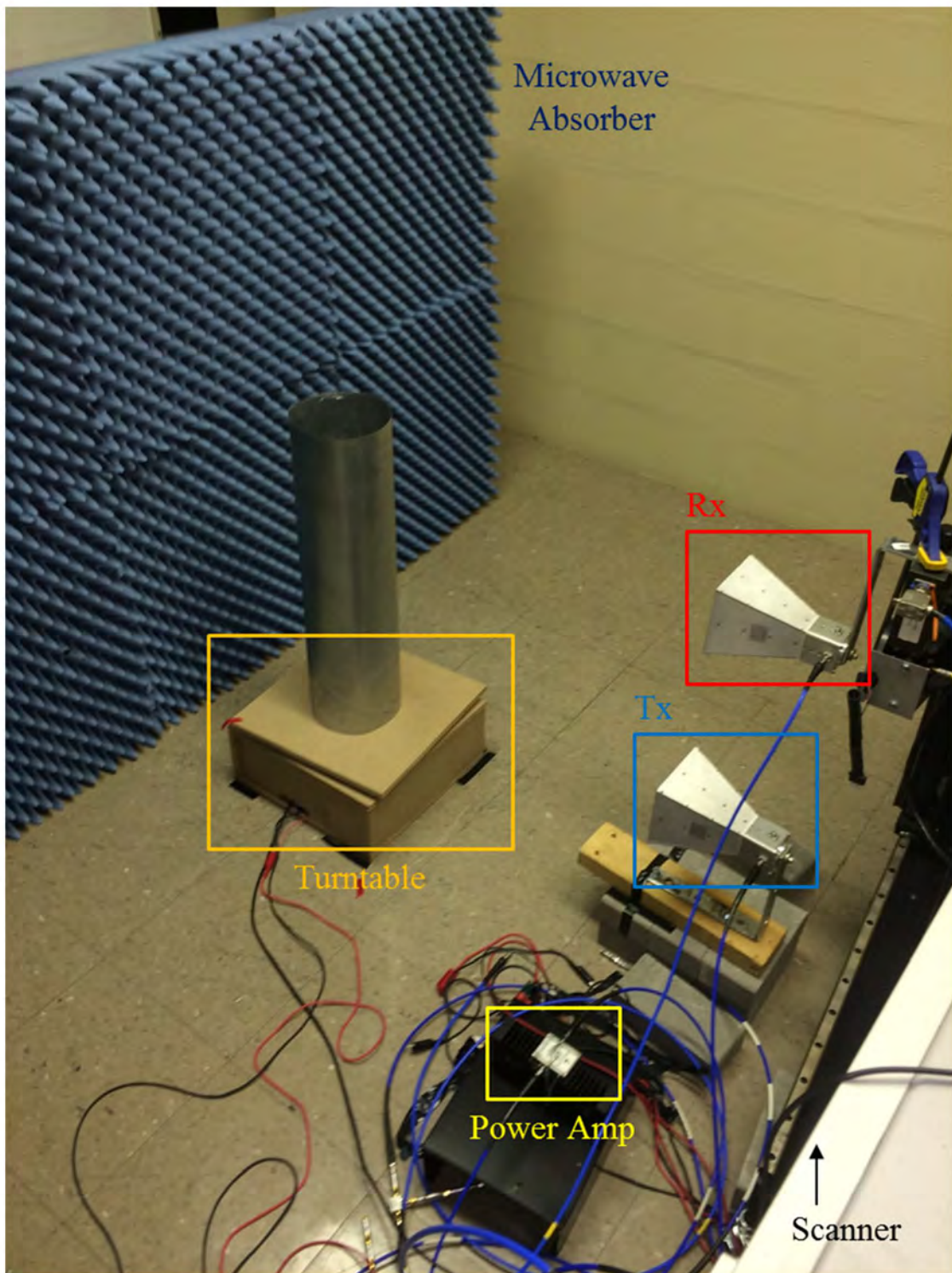


Figure 4-4. A metal cylinder placed on the turntable. Also shown are the transmitting and receiving antenna and microwave absorber behind the target to minimize reflections from the back.

is generated via sum and average of  $N$  images. After measurement with full  $360^\circ$  rotations, a total  $40 \times N$  final tomographic images are created, and they are combined into one complete image. The entire experiment process is identical to the Figure 3-2.

Figure 4-5 shows an example of 363,000 measured amplitude samples in time domain and the frequency response when both transmitting and receiving antennas are aligned at the center of the target object. The measured scattering data sample in Figure 4-5(a) are split into 200 segments so that each data segment contains 1815 amplitude samples. For example, the first segment in the red box #1 shown in Figure 4-5(a) and the frequency response are plotted in Figure 4-6. For each rotational angle  $\theta$ , a total of 200 images are generated from a large sequence of a single noise waveform, and the final image of the object at each rotational angular step is reconstructed via sum and average of all 200 images.

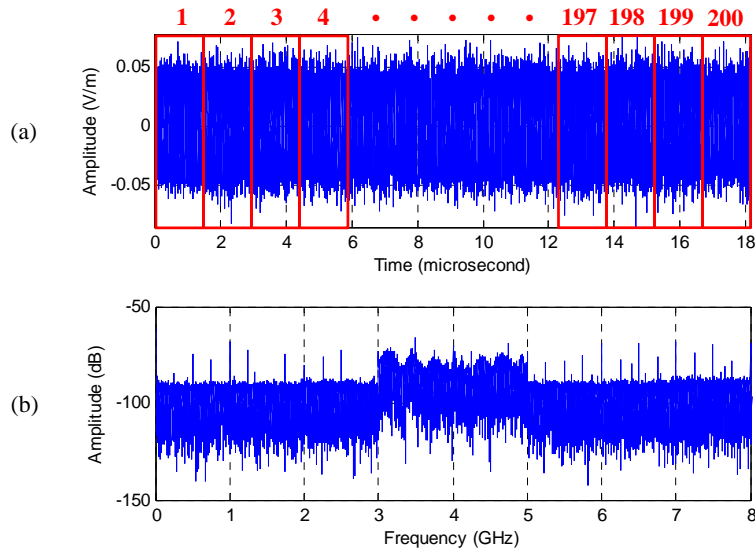


Figure 4-5. (a) The measured scattering data when both Tx and Rx are located at the center of the cylinder, and (b) the frequency spectrum of the measured data. The frequency spectrum ranges are shown from DC to 8 GHz only.

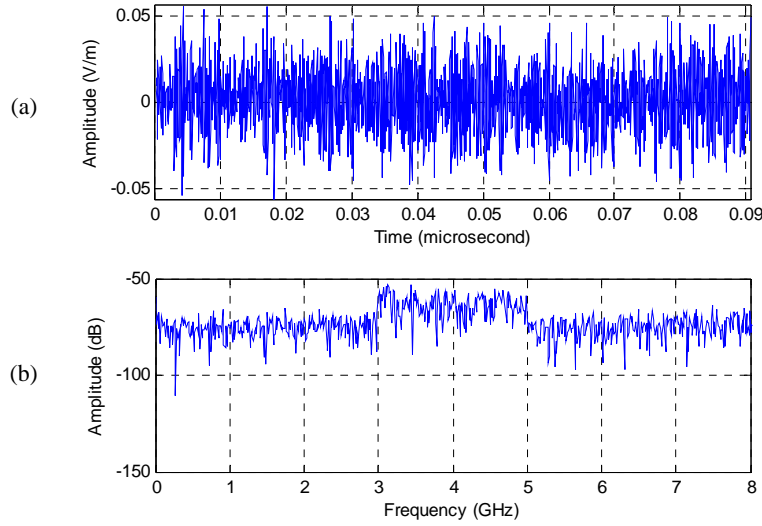


Figure 4-6. (a) The first segment of the measured scattering data shown in Figure 4-5(a), and (b) the frequency spectrum from DC to 8 GHz only.

### 4.3 Experimental Results

#### 4.2.1 Tomographic image for a circular metallic cylinder

A top view and side view of experiment configuration for a circular metallic cylinder are shown in Figure 4-7. The measured radius ( $r$ ) and height ( $h$ ) of the cylinder are approximately 10.2 cm and 40.6 cm, respectively, and the measured distance ( $d$ ) from the center of the cylinder to the edge of a transmitting antenna is approximately 66 cm. The measured dimensions of the circular metallic cylinder are shown in Figure 4-8. The transmitting antenna (Tx) is fixed at the center of the object, and the receiving antenna (Rx) is moving along the  $y$ -axis to collect the scattering data. Moving interval ( $\Delta y$ ) for Rx is 1.5 cm, i.e., scattering data are measured and recorded for 55 different positions along  $y$ -axis from (-66 cm, -40.5 cm) and (-66 cm, 40.5 cm).

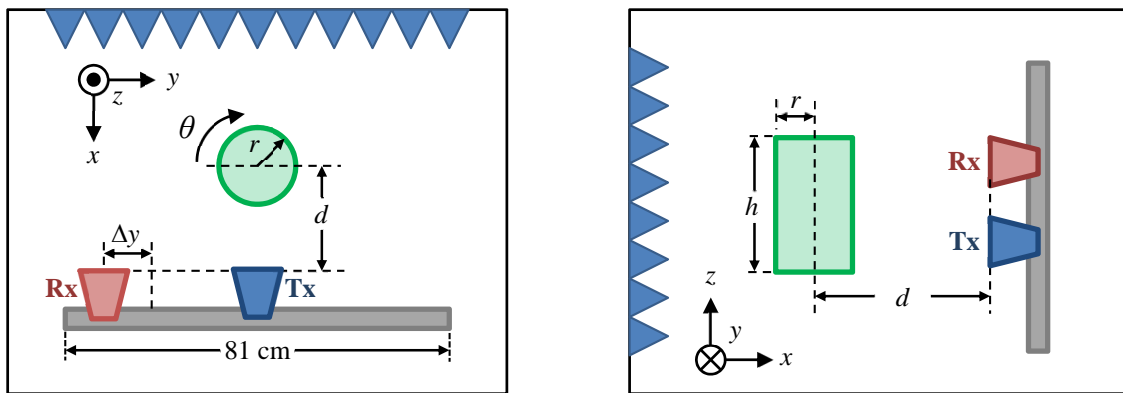


Figure 4-7. Top and side view of experiment configuration for a circular metallic cylinder. The cylinder is placed on the turntable for rotation. Also the microwave absorber behind the target is shown to minimize reflections from the back.



Figure 4-8. The metallic cylinder used for the experiment. The dimensions of the cylinder are measured in inches.

As shown in Figure 4-7, the target object is placed on the center of the turntable in front of a wall made of microwave absorbent foam. The turntable is configured to rotate  $9^\circ$  after a single line scan of 55 points along the linear scanner so that the scattering data is measured for 40 different angles. Figure 4-9 shows the complete tomographic image of the circular metallic cylinder based on the measured scattering data. As shown in Figure 4-9, the tomographic image

of the cylinder is correctly reconstructed; however, the image quality is not comparable to the simulated image displayed in Figure 3-9(d). Each pixel of the tomographic image displayed herein represents the normalized magnitude of scattering object function, which is proportional to the difference between the scattering due to the target object and the surrounding medium. Since the experiment is performed in the room surrounded by concrete walls, the image is severely affected by the additional scattering data due to concrete walls where no microwave absorbers are present. Also, unwanted noise from active RF components and equipment degrades the image quality. However, despite these unwanted reflections, the cylindrical shape is well recognized.

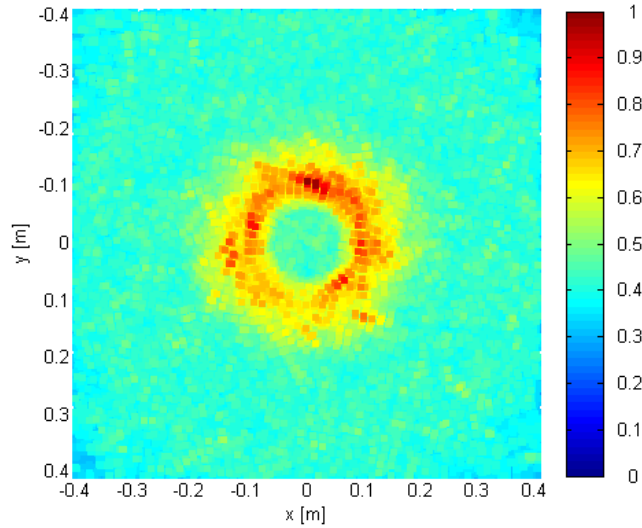


Figure 4-9. The final tomographic image of the metallic cylinder based on the measured data.

#### 4.2.2 Tomographic image for a square metallic box

Figure 4-10 displays a top view and side view of experiment configuration for a square metallic box. The dimension of the box is  $20.3 \times 20.3 \times 61$  cm. The measured distance ( $d$ ) from the center of the cylinder to the edge of a transmitting antenna is approximately 66 cm. The

measured dimensions of the square metallic box are shown in Figure 4-11. For the square metallic box measurement, moving interval ( $\Delta y$ ) for Rx is 1.5 cm so that scattering data are measured and recorded for 55 different positions along y-axis from (-66 cm, -40.5 cm) and (-66 cm, 40.5 cm). The turntable is configured to rotate 9° after a single line scan, and the scattering data is measured for 40 different angles.

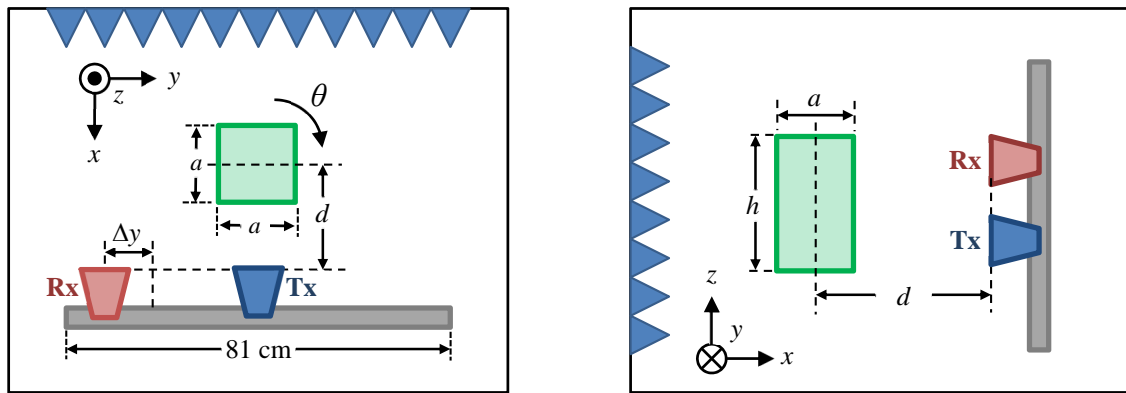


Figure 4-10. Top and side view of experiment configuration for a square metallic box. The box is placed on the turntable for rotation. Also the microwave absorber behind the target is shown to minimize reflections from the back.



Figure 4-11. The metallic box used for the experiment. The dimensions of the box are measured in inches.

As shown in Figure 4-12, the tomographic image of the box is correctly reconstructed as expected; however, the image quality is not comparable to the simulation results shown in Figure 3-11(d). Similarly, the image is severely affected by the additional scattering data due to concrete walls and unwanted noise from active RF components.

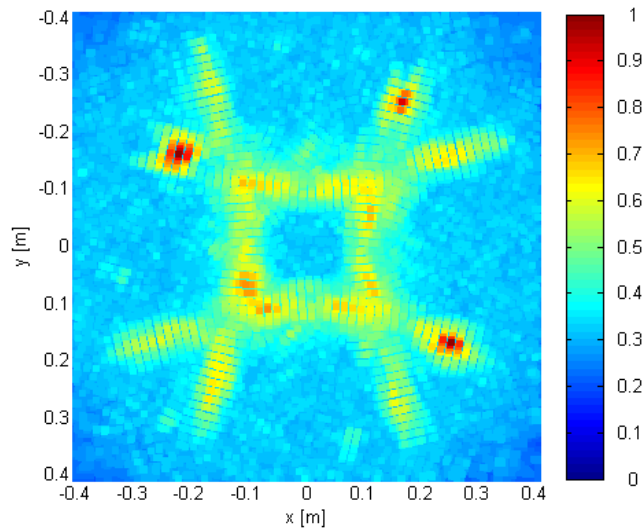


Figure 4-12. The final tomographic image of the metallic box based on the measured data.

#### 4.2.3 Tomographic image for an equilateral triangular metallic prism

Figure 4-13 shows a top view and side view of experiment configuration for an equilateral triangular metallic prism. The length of all sides of the triangle is 20.3 cm, and the height ( $h$ ) of the prism is 30.5 cm. The measured distance ( $d$ ) from the center of the prism to the edge of a transmitting antenna is approximately 66 cm. All other experimental configurations, such as the positions of 55 scanning points and the rotational angle, remain unchanged.

Figure 4-14 and Figure 4-15 show the actual triangular prism and the complete tomographic image with a full 360° rotation of the object, respectively. The image quality of

tomographic image shown in Figure 4-15 is degraded by the additional scattering data due to concrete walls and unwanted noise from active RF components. However, the cross-section image of the prism can be clearly inferred.

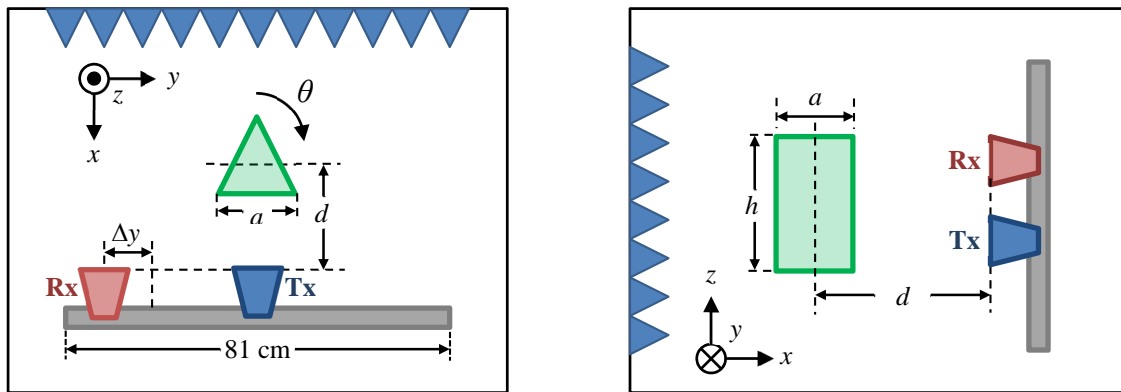


Figure 4-13. Top and side view of experiment configuration for an equilateral triangular metallic prism. The prism is placed on the turntable for rotation. Also the microwave absorber behind the target is shown to minimize reflections from the back.



Figure 4-14. The metallic prism used for the experiment. The dimensions of the prism are measured in inches.

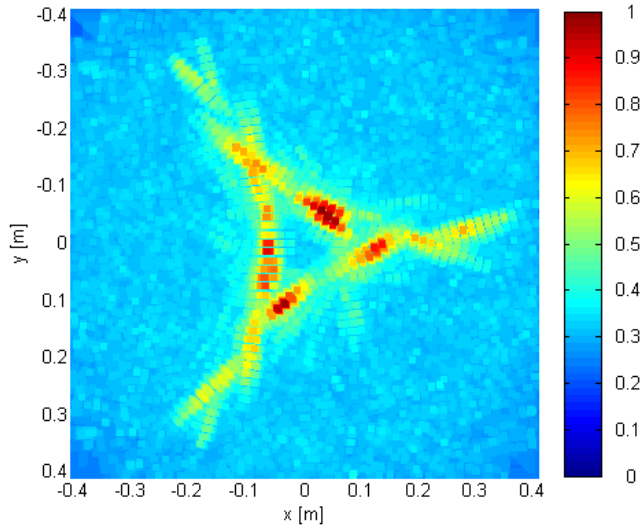


Figure 4-15. The final tomographic image of the metallic prism based on the measured data.

#### 4.2.4 Tomographic image for a circular concrete cylinder

A top view and side view of experiment configuration for a circular concrete cylinder are shown in Figure 4-16. The measured radius ( $r$ ) and height ( $h$ ) of the cylinder are approximately 7.6 cm and 30.5 cm, respectively, and the measured distance ( $d$ ) from the center of the cylinder to the edge of a transmitting antenna is approximately 66 cm. The measured dimensions of the circular concrete cylinder are shown in Figure 4-17. The transmitting antenna (Tx) is fixed at the center of the object, and the receiving antenna (Rx) is moving along the  $y$ -axis to collect the scattering data. Moving interval ( $\Delta y$ ) for Rx is 3 cm, i.e., scattering data are measured and recorded for 29 different positions along  $y$ -axis from (-66 cm, -40.5 cm) and (-66 cm, 40.5 cm).

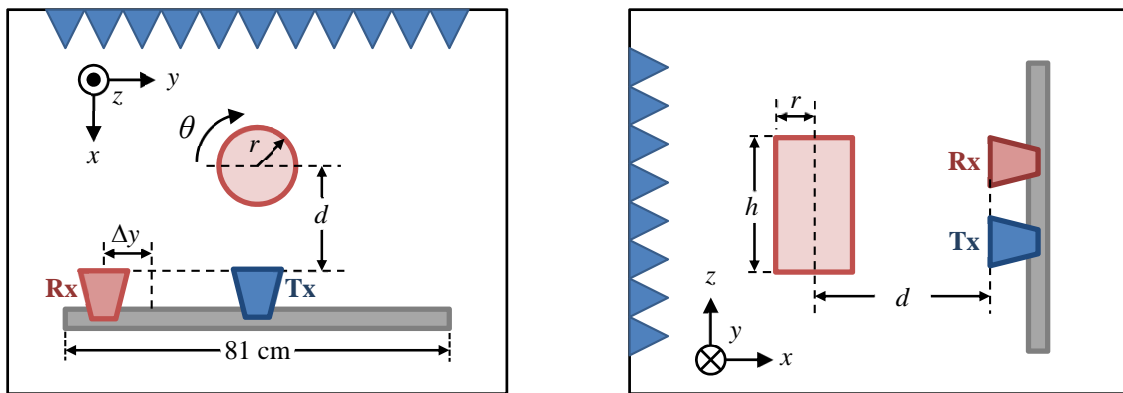


Figure 4-16. Top and side view of experiment configuration for a circular concrete cylinder. The cylinder is placed on the turntable for rotation. Also the microwave absorber behind the target is shown to minimize reflections from the back..



Figure 4-17. The concrete cylinder used for the experiment. The dimensions of the cylinder are measured in inches.

The turntable is configured to rotate  $9^\circ$  after a single line scan of 29 points along the linear scanner so that the scattering data is measured for 40 different angles. Figure 4-18 shows the complete tomographic image of the circular concrete cylinder based on the measured scattering data. Although the tomographic image of the dielectric cylinder is successfully obtained, the image is not truly vivid compared to the metallic circular cylinder, as expected. The

measured scattering field intensity due of concrete object is not as strong as the metallic object case. Also the surface roughness and the composition of concrete cylinder affect the scattering behavior, which degrades the image quality compared to the metallic cylinder case shown in Figure 4-9.

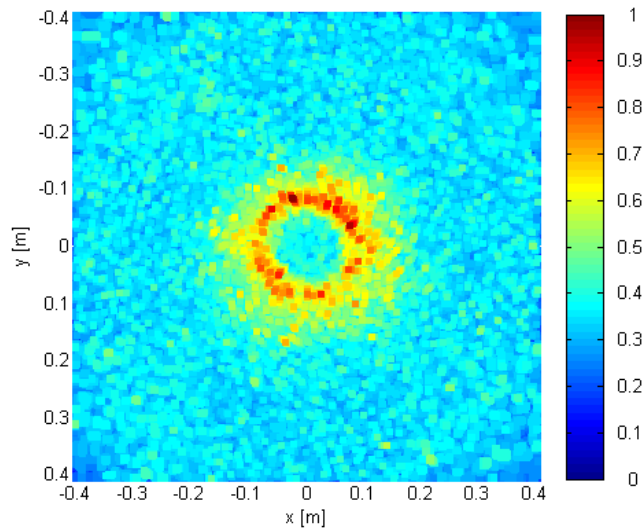


Figure 4-18. The final tomographic image of the concrete cylinder based on the measured data.

#### 4.2.5 Tomographic Image for a square concrete block

Figure 4-19 displays a top view and side view of experiment configuration for a square concrete block. The dimension of the block is  $15.2 \times 15.2 \times 28$  cm. The measured distance ( $d$ ) from the center of the cylinder to the edge of a transmitting antenna is approximately 66 cm. The measured dimensions of the square metallic box are shown in Figure 4-20. For the concrete block measurement, the transmitting antenna (Tx) is fixed at the center of the object, and only receiving antenna (Rx) is moving along the y-axis to collect the scattering data for 29 different

scanning points, i.e.,  $\Delta y = 3$  cm, from  $(-66\text{ cm}, -40.5\text{ cm})$  and  $(-66\text{ cm}, 40.5\text{ cm})$ . The turntable is configured to rotate  $9^\circ$  after a single line scan, and the scattering data is measured for 40 different angles.

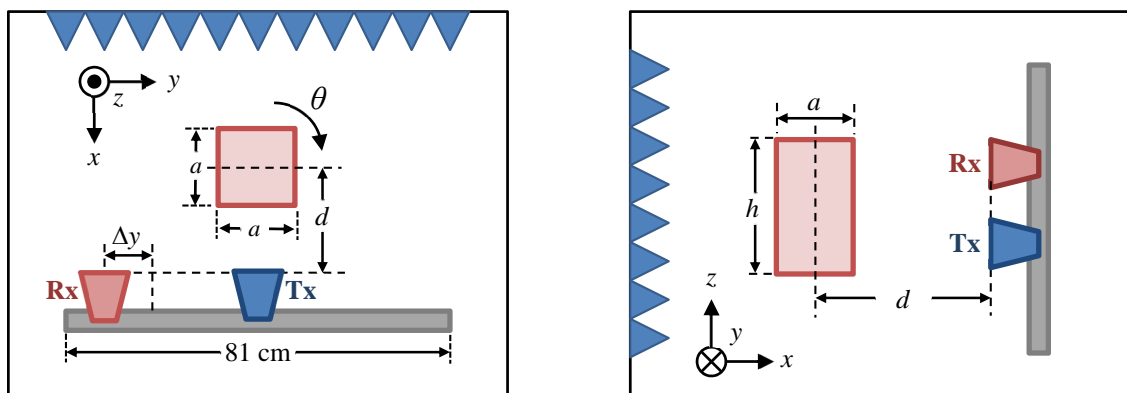


Figure 4-19. Top and side view of experiment configuration for a square concrete block. The box is placed on the turntable for rotation. Also the microwave absorber behind the target is shown to minimize reflections from the back.



Figure 4-20. The concrete block used for the experiment. The dimensions of the concrete block are measured in inches.

Figure 4-21 shows the complete tomographic image with a full 360° rotation of the object, respectively. As shown in Figure 4-21, the tomographic image of the box is correctly reconstructed. Similarly, the image of the concrete box is affected by the measured field intensity from the experiment. The surface of the concrete block is not truly smooth compared to the circular concrete cylinder as shown in Figure 4-20.

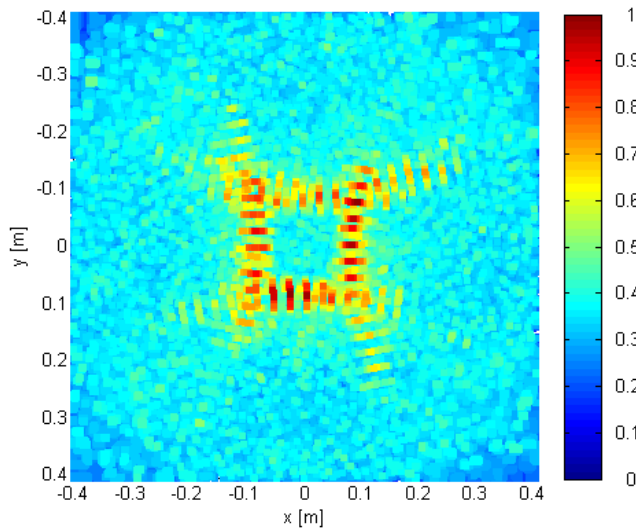


Figure 4-21. The final tomographic image of the concrete block based on the measured data.

#### 4.4 Summary

A bistatic UWB noise tomography radar system is implemented, demonstrating various tomographic imaging scenarios using iid WGN waveforms. The complete tomographic images of the sequentially rotated objects are successfully reconstructed with relatively simple hardware setup. Based on experimental results presented in this chapter, radar tomography using WGN waveforms is accomplished while maintaining the advantages of UWB noise radar such as LPI and high-resolution imaging capability. The cross-section of the metallic object is successfully

imaged compared to the dielectric object cases; however, more diffraction occurs from the sharp edges of the metallic objects compared to the dielectric objects. The reconstructed tomographic images based on measured scattering data can be compared with those obtained based on numerical simulation results, showing a good agreement between simulation and experiment results for both metallic and dielectric target object cases.

#### 4.5 References

- [1] A. Broquetas, R. Jordi, J. M. Rius, A. R. Elias-Fuste, A. Cardama and L. Jofre, "Cylindrical geometry: a further step in active microwave tomography," *IEEE Transactions on Microwave Theory and Techniques*, vol. 39, pp. 836-844, 1991.
- [2] J. C. Bolomey and C. Pichot, "Microwave tomography: from theory to practical imaging systems," *International Journal of Imaging Systems and Technology*, vol. 2, pp. 144–156, 1990.
- [3] S. Y. Semenov, R. H. Svenson, A. E. Boulyshev, A. E. Souvorov, V. Y. Borisov, Y. Sizov, A. N. Starostin, K. R. Dezern, G. P. Tatsis and V. Y. Baranov, "Microwave tomography: two-dimensional system for biological imaging," *IEEE Transactions on Biomedical Engineering*, vol. 43, pp. 869-877, 1996.
- [4] A. Verity, S. Gavrilov, T. Adigüzel, I. Voynovskyy, G. Yüceer and A. O. Salman, "C-band tomography system for imaging of cylindrical objects," in *Proc. SPIE Conference on Subsurface Sensors and Applications*, Denver, CO, 1999, pp. 224-230.
- [5] C. Gilmore, P. Mojabi, A. Zakaria, M. Ostadrahimi, C. Kaye, S. Noghanian, L. Shafai, S. Pistorius and J. LoVetri, "An ultra-wideband microwave tomography system: preliminary results," in *Proc. Annual International Conference of the IEEE Engineering in Medicine and Biology Society* (EMBC 2009), Minneapolis, MN, 2009, pp. 2288-2291.

- [7] M. Z. Abdullah, S. A. Binajjaj, T. F. Zanoon and A. J. Peyton, "High-resolution imaging of dielectric profiles by using a time-domain ultra wideband radar sensor," *Measurement*, vol. 44, pp. 859-870, 2011.

## Chapter 5

### Conclusions and Future Work

#### **5.1 Conclusions**

The dissertation has been concerned with tomographic imaging for UWB noise radar using Fourier diffraction theorem. This concluding chapter gives a summary of the results from previous chapters of the dissertation.

In Chapter 2, the theoretical foundations of diffraction tomography using a white Gaussian noise waveform as a transmitted signal for the cross-section images of multiple metallic target objects inside a rectangular geometry are presented. Further, the empirical solution to bypass the shortcoming of using UWB random noise waveform and the image quality measures of the reconstructed images under various SNR environments are discussed.

In Chapter 3, the principle and numerical simulation results of tomographic imaging of various target scenarios using UWB noise radar are presented. Theoretical analysis of the image reconstruction for a bistatic imaging radar system with a two-dimensional rotating cylinder using Fourier diffraction theorem under the assumption of plane wave illumination is discussed. Also, the numerical simulation results of diffraction tomography for UWB noise radar are shown in the chapter.

In Chapter 4, the hardware implementation and experimental investigation of UWB noise radar are proposed. Design considerations and performance for UWB noise radar using WGN waveforms are presented in the chapter. Further, tomographic image processing technique for large sets of collected data samples is proposed. The reconstructed tomographic images based on experiments for various target objects are presented as well.

## 5.2 Suggestions for Future Work

### 5.2.1 UWB noise radar tomography for X-band

The block diagram for the transmitter and the receiver portions of the system for 3–5 GHz frequency ranges are shown in Figure 4-2. Since the maximum sampling rate of AWG (Agilent M8190A) is 12 GSa/s, the maximum frequency of the output waveform is up to 6 GHz. For the operating frequency beyond 6 GHz, additional RF components are required for frequency up-conversion of the bandlimited noise waveforms by heterodyning on the transmitter block. Also, frequency down-conversion should be considered for the receiver design unless the sampling rate of the oscilloscope is twice of the frequency of the received signals.

X-band is a segment of frequency spectrum ranges between 8–12 GHz, which has been commonly used for high-resolution imaging and remote sensing applications in radars [1, 2, 3]. Figure 5-1 shows a proposed UWB noise radar configuration for X-band frequency operation, which is the modified hardware design based on the hardware configuration shown in Figure 4-2. As shown in Figure 5-1, the mixer and local oscillator are added for a frequency up-conversion purpose. Also, several power amplifiers may be cascaded in order to provide sufficient gain for higher frequency ranges. The beam pattern of both transmitting and receiving antennas should be investigated so that the target object is always in the main lobe for all measurements. In general, the image quality of the tomographic image can be degraded due to the effects of unwanted additive noise from additional active RF components.

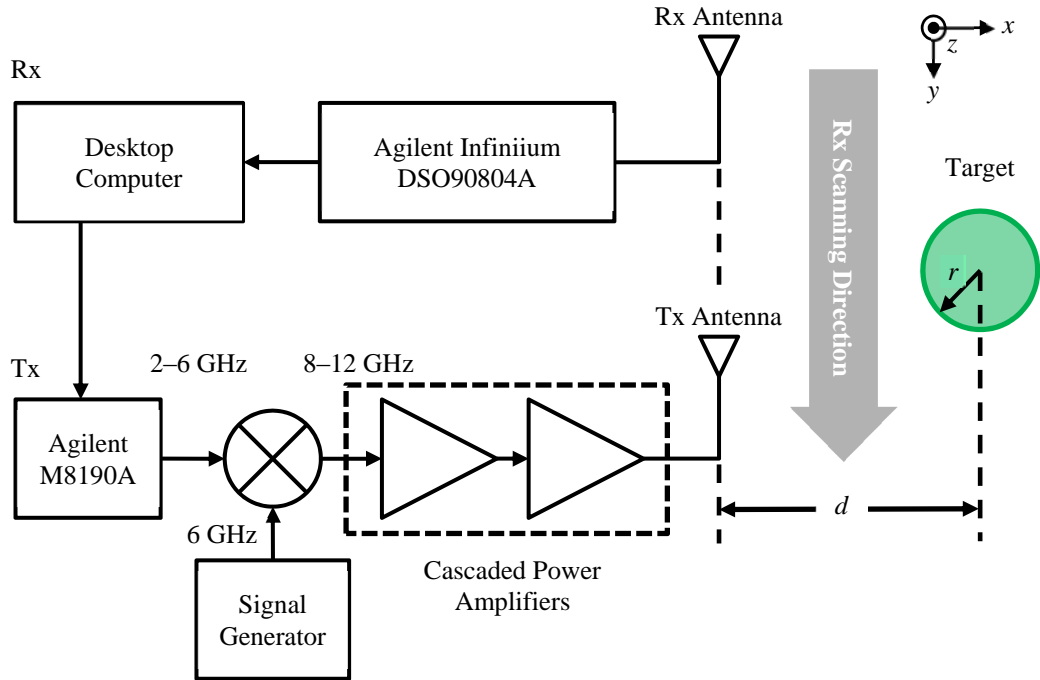


Figure 5-1. The proposed design of transmitter and receiver for X-band operation.

### 5.2.2 Moving average filter for noise suppression

The moving average filter (MAF) operates by averaging a number of points from the input signal to produce each point in the output signal. The general equation of the moving average filter is written as

$$y[i] = \frac{1}{M} \sum_{j=-(M-1)/2}^{(M-1)/2} x[i+j] \quad (5.1)$$

where  $x[\cdot]$  is the input signal,  $y[\cdot]$  is the output signal, and  $M$  is the number of points in the average. The measured scattered field data can be considered as the input signal,  $x[\cdot]$ , and the obtained signals after applying the moving average filter is considered as the output signal,  $y[\cdot]$ . The value of  $M$ , i.e., the number of points in the average, is changed accordingly to check how the moving average filter effectively suppresses the additive noise.

Figure 5-2 shows a top view and side view of experiment configuration for a circular metallic cylinder. The frequency ranges of the transmitted noise waveforms are 2–4 GHz, and 100 iid noise waveforms with amplitude samples of 1001 are transmitted and received. The measured radius ( $r$ ) and height ( $h$ ) of the cylinder are approximately 8 cm and 30.5 cm, respectively. The measured distance ( $d$ ) from the center of the cylinder to the edge of a transmitting antenna is approximately 71 cm. The transmitting antenna (Tx) is fixed at the center of the object, and the receiving antenna (Rx) is moving along the  $y$ -axis to collect the scattering data. Moving interval ( $\Delta y$ ) for Rx is 1.5 cm, i.e., scattering data are measured and recorded for 55 different positions along  $y$ -axis from (-71 cm, -40.5 cm) and (-71 cm, 40.5 cm). The target object is not rotated for the experiment of moving average filter.

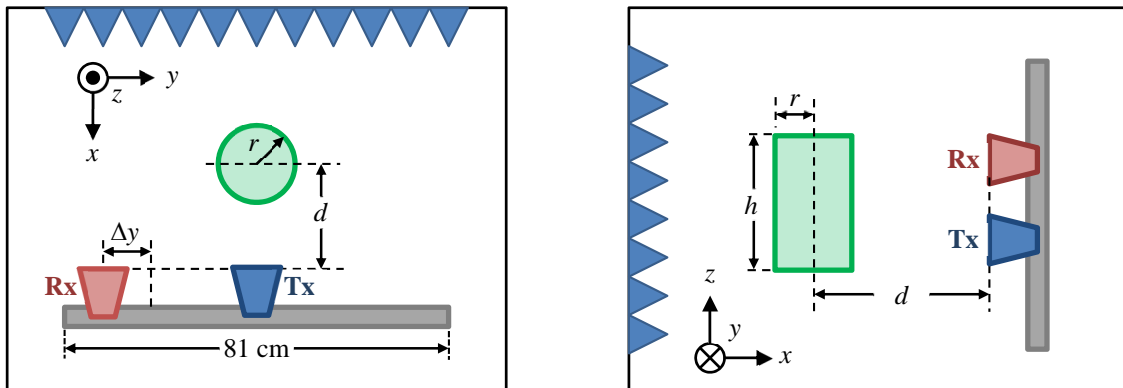


Figure 5-2. Top and side view of experiment configuration for a circular metallic cylinder. The cylinder is not rotated. Also the microwave absorber behind the target is shown to minimize reflections from the back.

Figure 5-3 shows the example of frequency domain scattering data plots among 1001 collected scattering data when both Tx and Rx antennas are aligned at the center of the linear scanner with different numbers of points in the average: 1-pt (no MAF), 3-pt, 5-pt and 7-pt MAF.

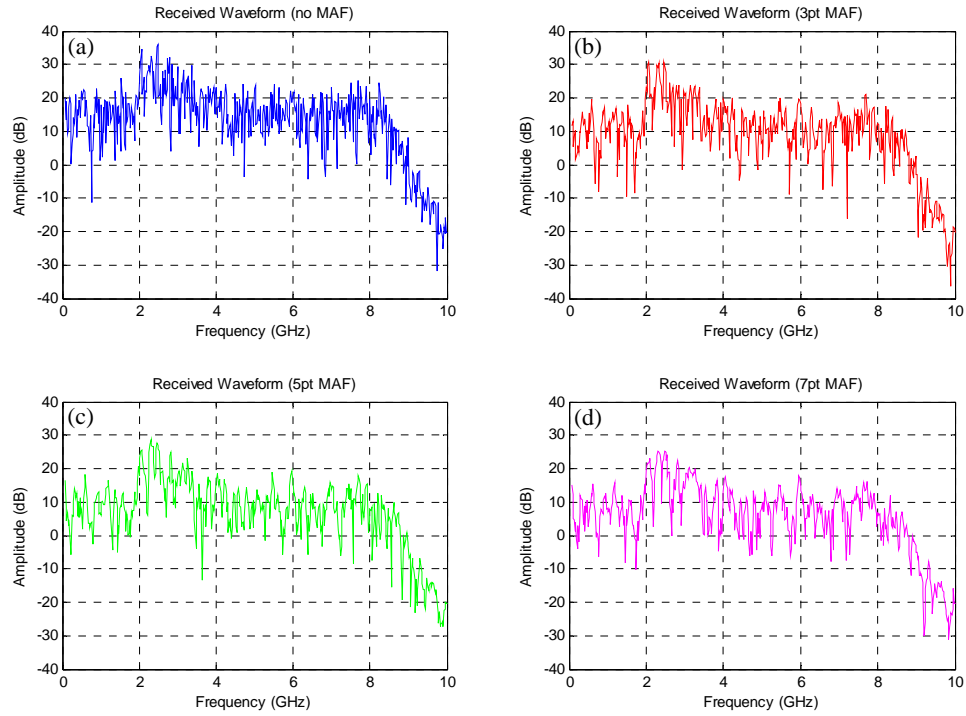


Figure 5-3. Frequency responses of the collected scattering data with (a) 1-pt (no MAF), (b) 3-pt, (c) 5-pt, and (d) 7-pt MAF applied.

As shown in Figure 5-3, the smoothing action of the moving average filter decreases the amplitude of the random noise in collected waveforms, but also reduces the sharpness of the original waveform as the number of average increase. In general, the amount of noise reduction is equal to the square root of the number of points in the average.

Figure 5-4 shows the reconstructed tomographic images based on 4 different points of moving average filter shown in Figure 5-3. As shown in Figure 5-4, tomographic images clearly show how the moving average filters effectively work by suppressing the random noise in collected waveforms.

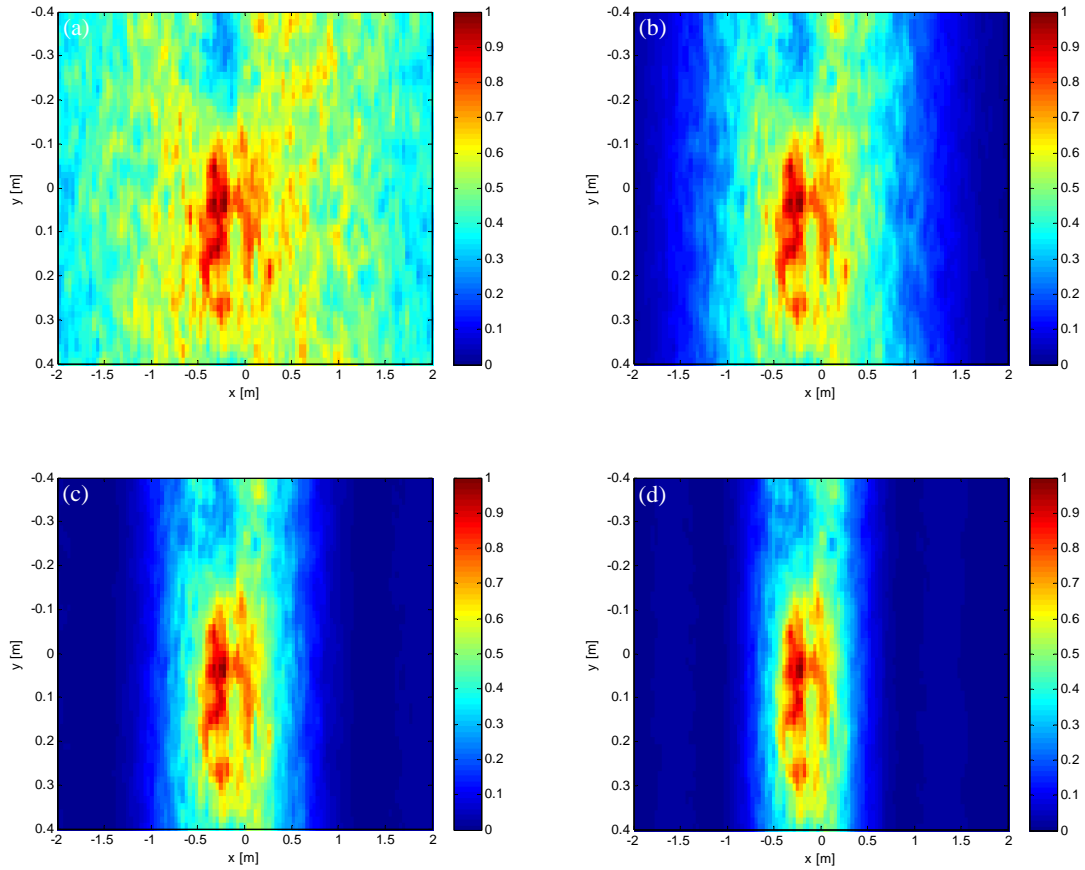


Figure 5-4. Tomographic images based on measured scattering data when (a) no MAF, (b) 3-pt MAF, (c) 5-pt MAF, and (d) 7-pt MAF applied.

### 5.2.3 Background subtraction method for image enhancement

Background subtraction is a widely used approach in the image processing, identifying target objects from the clutter or surrounding environment. Additional data acquisition and image processing are required in order to perform the background subtraction. When the scattering data acquisition process with a target object is complete, additional scattering data must be collected without the presence of the target object for obtaining a background image. The final tomographic image is reconstructed based on the comparison of two images, showing the intensity for the pixel which has changed in two images.

Two tomographic images shown in Figure 5-5 display the effectiveness of background subtraction. All experimental configurations for background subtraction technique are identical to the previous setup shown in Figure 5-2. As shown in Figure 5-5, the shape of the target object is clearly extracted and imaged, providing a noticeable difference in image after background subtraction is correctly implemented.

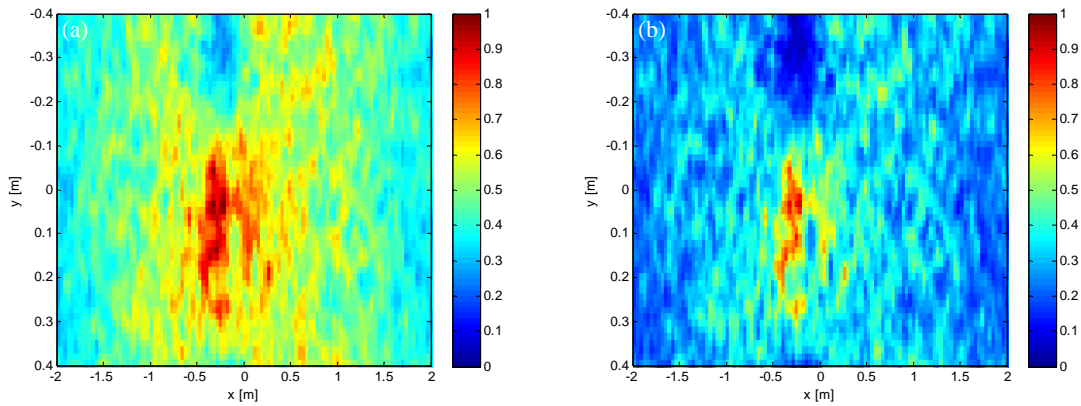


Figure 5-5. Tomographic images based on measured scattering data when (a) no background subtraction, and (b) background subtraction is implemented.

### 5.3 References

- [1] E. R. Stofan, D. L. Evans, C. Schmullius, B. Holt, J. J. Plaut, J. Van Zyl, S. D. Wall, J. Way, “Overview of results of spaceborne imaging radar-C, X-band synthetic aperture radar (SIR-C/X-SAR),” *IEEE Transactions on Geoscience and Remote Sensing*, vol. 33, no. 4, pp. 817-828, 1995.
- [2] R. Gangeskar, “Ocean current estimated from X-band radar sea surface, images,” *IEEE Transactions on Geoscience and Remote Sensing*, vol. 40, no. 4, pp. 783-792, 2002.

- [3] E. N. Anagnostou, M. N. Anagnostou, W. F. Krajewski, A. Kruger, and B. J. Miriovsky, "High-resolution rainfall estimation from X-band polarimetric radar measurements," *J. Hydrometeor*, vol. 5, pp. 110-128, 2004.

## VITA

### **Hee Jung Shin**

#### **Research Interests**

Computational and experimental electromagnetics, microwave system design and development, ultra-wideband radar system including radar image analysis.

#### **Education**

- Ph.D. The Pennsylvania State University, Electrical Engineering.
- M.S. University of California, Irvine, Electrical Engineering.
- B.S. University of California, Irvine, Electrical Engineering.

#### **Publications**

- Hee Jung Shin, Mark A. Asmuth, Ram M. Narayanan, and Muralidhar Rangaswamy, “Principle, design and implementation of UWB noise radar tomography,” preparing to submit to *Progress In Electromagnetics Research*, 2015.
- Hee Jung Shin, Ram M. Narayanan, and Muralidhar Rangaswamy, “Simulations of tomographic imaging of various target scenarios using noise waveforms,” accepted to *IEEE Radar Conference*, May 2015.
- Hee Jung Shin, Mark A. Asmuth, Ram M. Narayanan, and Muralidhar Rangaswamy, “Principle and experimental results of ultra-wideband noise radar imaging of a cylindrical conducting object using diffraction tomography,” accepted to *SPIE Conference on Radar Sensor Technology XIX*, April 2015.

- Mark A. Asmuth, **Hee Jung Shin**, Ram M. Narayanan, and Muralidhar Rangaswamy, “Design and implementation of a noise radar tomographic system,” accepted to SPIE Conference on Radar Sensor Technology XIX, April 2015.
- **Hee Jung Shin**, Ram M. Narayanan, and Muralidhar Rangaswamy, “Ultrawideband noise radar imaging of impenetrable cylindrical objects using diffraction tomography,” *International Journal of Microwave Science and Technology*, 2014.
- **Hee Jung Shin**, Ram M. Narayanan, and Muralidhar Rangaswamy, “Diffraction tomography for ultra-wideband noise radar and imaging quality measure of a cylindrical perfectly conducting object,” in *Proceedings of the 2014 IEEE Radar Conference*, May 2014.
- **Hee Jung Shin**, Ram M. Narayanan, and Muralidhar Rangaswamy, “Ultra-wideband noise radar imaging of cylindrical PEC objects using diffraction tomography,” in *Proceedings of the SPIE Conference on Radar Sensor Technology XVIII*, Baltimore, MD, May 2014.
- **Hee Jung Shin**, Ram M. Narayanan, and Muralidhar Rangaswamy, “Tomographic imaging with ultra-wideband noise radar using time-domain data,” in *Proceedings of the SPIE Conference on Radar Sensor Technology XVII*, Baltimore, MD, April 2013

The Pennsylvania State University  
The Graduate School College of Engineering

# **Noise radar tomography system design and data collection**

A Thesis in  
Electrical Engineering by  
Mark A. Asmuth  
© 2015 Mark A. Asmuth

Submitted in Partial Fulfillment of the Requirements  
for the Degree of  
Master of Science  
December 2015

The thesis of Mark A. Asmuth was reviewed and approved\* by the following:

Ram M. Narayanan  
Professor of Electrical Engineering  
Thesis Advisor

James K. Breakall  
Professor of Electrical Engineering

Kultegin Aydin  
Professor of Electrical Engineering  
Head of the Electrical Engineering Department

\* Signatures are on file in the Graduate School

## ABSTRACT

A hardware system has been developed to perform ultrawideband (UWB) noise radar tomographic imaging over the 3–5 GHz frequency range. The system has been tested on a variety of target objects that have been concealed in both cardboard and wood. The system utilizes RF hardware to transmit multiple independent and identically distributed (iid) UWB random noise waveforms. A 3–5 GHz band-limited signal is generated using an arbitrary waveform generator and the waveform is then amplified and transmitted through a horn antenna. A linear scanner with a single antenna is used in place of an antenna array to collect backscatter. The backscattered data are collected from the transmission of each waveform and reconstructed to form an image. The images that result from each scan are averaged to produce a single tomographic image of the target. After background subtraction, the scans are averaged to improve the image quality. The experimental results are compared to the theoretical predictions. The system is able to successfully image metallic and dielectric cylinders of different cross sections.

## Table of Contents

List of Figures	v
List of Tables	vii
Acknowledgements	viii
1 Introduction and Background	1
2 System Design and Implementation	4
3.1 Transmission and Reception .....	4
3.2 Turntable and Linear Scanner .....	7
3 Data Collection and Processing	12
4 Experimental Results	14
5 Future Work and Conclusions	20
5.1 Future Work .....	20
5.2 Conclusions .....	22
Appendix	23
A Images of test objects .....	23
B Computer programs. ....	31
References	71

## List of Figures

1	Block diagram of (a) transmitter and (b) receiver.	6
2	(a) Noise waveform taken directly out of the AWG, (b) averaged noise waveform taken directly from the AWG, and (c) reflected and averaged waveform off of a metal cylinder.	7
3	A metal cylinder placed on the turntable. Also shown are the transmitting and receiving antenna and microwave absorber behind the target to minimize reflections from the back.	7
4	Tomographic image of a metallic rectangular box imaged with (a) 55 lateral points, and (b) 29 lateral points. Note that the imaging with 55 points is much better and cleaner than the one with 29 points. All of the data presented in this document used 55 lateral points for imaging.	8
5	Tomographic image of (a) metal cylinder, and (b) dielectric cylinder.	14
6	Tomographic image of (a) aluminum rectangular box, and (b) dielectric rectangular box.	15
7	Tomographic image of triangular metal cylinder	16
8	Tomographic image of (a) triangular metal cylinder in a cardboard box, and (b) circular metal cylinder in a cardboard box.	17
9	Tomographic image of (a) metal cylinder 1, (b) metal cylinder 2, (c) metal rectangular box 1, (d) metal rectangular box 2, (e) metal cylinder with triangular cross section, (f) dielectric cylinder, and (g) dielectric rectangular box. These objects are concealed in a wooden box	19
10	High frequency transmitting system.	21
11	High frequency receiving system.	21
12	Metal Rectangular Box 1	23
13	Metal Rectangular Box 2	24
14	Metal Cylinder 1	25
15	Metal Cylinder 2	26
16	Dielectric Rectangular Box	27

17	Dielectric Circular Cylinder	28
18	Dielectric Semicircular Cylinder	29
18	Metal Cylinder with Triangular Cross Section	30

## **List of Tables**

1	Hardware Characteristics	5
2	Test objects imaged by the noise tomography system	10

## **Acknowledgments**

I would like to thank my advisor Dr. Ram Narayanan for his help and guidance and my committee member Dr. James Breakall for providing useful comments. I would like to thank my project partner Hee Jung Shin for assisting with the data collection and data analysis. I would also like to thank my fellow lab mates: Scott Wilson, Travis Butler, Kyle Gallagher, Brian Phelan and the rest of the Radar Communications lab for all their help. The support of the US Air Force Office of Scientific Research (AFOSR) through Grant # FA9550-12-1-0164 is gratefully acknowledged. Finally, I would like to thank Dr. Muralidhar Rangaswamy of the US Air Force Research Laboratory (AFRL) for providing assistance in all aspects of the research.

## 1. INTRODUCTION AND BACKGROUND

Microwave tomography has been developed and refined over the past few decades to obtain high-resolution images of metallic targets and dielectric contrasts embedded within a dielectric medium. The objective of active microwave tomography is to reconstruct the dielectric properties of a body illuminated with microwaves from a measurement of the scattered fields. Conventional microwave tomography systems are based on illuminating the body with a plane wave and measuring the scattered fields with a linear array of probes. A practical requirement when using this method is the need for mechanical rotation of either the body or the antenna in order to obtain measurements in different views<sup>1</sup>. Every object, when inserted into an electromagnetic field, causes a well-defined field change, and diffraction occurs when the wavelength of the microwave radiation is of the order of the dimension of the object. A one-to-one relationship relating the scattered field to the object complex permittivity can be obtained within the Born approximation, via a Fourier transform using the so-called Fourier Diffraction Theorem<sup>2</sup>. Microwave imaging has been studied for malignant breast cancer detection<sup>3-5</sup>. Several hardware systems have been developed and implemented over the years. A microwave tomographic system consisting of 64 circularly arranged electronically scanned antennas, divided into 32 transmitters and 32 receivers, operating at a frequency of 2.45 GHz was developed for biological tissue imaging<sup>6</sup>. A C-band system operating at 7.5 GHz was developed for imaging weakly scattering objects, such as paper cylinders<sup>7</sup>. More recently, a four-port imaging system using a vector network analyzer (VNA) operating over the 7.5–12.5 GHz frequency range was used to reconstruct images of continuous and discrete conducting objects and a B-52 model aircraft<sup>8</sup>. A 2D UWB microwave imaging system 3–6 GHz frequency range using

24 antenna elements connected to a VNA via a  $2 \times 24$  port matrix switch was able to quantitatively reconstruct dielectric objects<sup>9</sup>. A time-domain UWB tomographic imaging system transmitting a differentiated cosine-modulated Gaussian pulse with a carrier frequency of 1 GHz was used to reconstruct plastic phantoms of different sizes and shapes immersed in a tank filled with pipe water<sup>10</sup>. Tomographic reconstruction has been used in many settings, such as medical and infrastructure<sup>11-13</sup>.

Noise waveforms have been used in radar for many years<sup>14-15</sup>. Noise waveforms provide several advantages for covert applications due to their low probability of intercept (LPI) and low probability of detection (LPD) characteristics<sup>16-19</sup>. These attributes come from the fact the random noise signal changes constantly and does not repeat<sup>20</sup>. Radar tomography using an UWB Gaussian noise waveform has been proposed as a covert tomographic imaging technique. Using either resistors or noise diodes and then amplifying the thermal noise it is possible to cheaply generate the noise<sup>21</sup>. This process relies on the properties of the noise used in the waveform. The method uses band-limited independent and identically distributed (iid) white Gaussian Noise (WGN) for the waveform. The approach utilizes the fact that WGN has a flat frequency spectrum. To actually achieve the flat frequency spectrum in hardware, multiple WGN waveforms must be averaged together. Using Fourier diffraction theory, it has been shown that is indeed possible to construct a tomographic image of the object<sup>22</sup>.

This thesis discusses a UWB noise tomographic system specially developed by us to generate tomographic images of various objects and presents the experimental results from this system. Chapter 2 describes the hardware implementation. Chapter 3 presents the data collection and processing approach. Chapter 4 shows experimental tomographic

images on a variety of metallic and dielectric targets, both under open and concealed conditions. Chapter 5 presents conclusions and future work.

## **2. SYSTEM DESIGN AND IMPLEMENTATION**

The data collection system is controlled using a single computer. The computer is directly connected to four devices. The computer directly controls two Arduinos, an Arbitrary Waveform Generator (AWG), and an oscilloscope. Before the data collection process begins, the computer uploads a noise waveform to the AWG using a MATLAB code. The AWG continuously transmits that noise waveform for the duration of the test. The two Arduinos are used to control the position of the turntable that the test object is placed on and the receiving antenna. The Arduino in control of the turntable rotates the object a certain number of degrees that is selected using MATLAB using a stepper motor. The second Arduino controls a linear scanner that has the receiving antenna mounted on it. The scanner stops at each point that is designated in MATLAB so data can be collected at that point. The receiving antenna is connected directly to the oscilloscope for sampling. The oscilloscope collects time-domain data and then passes that data back to the computer.

### **2.1 Transmission and Reception**

The block diagram for the transmit and the receive portions of the system are shown in Figure 1. The computer uploads an iid Gaussian Noise Waveform to the AWG. The AWG is an Agilent M8190A system mounted on a M9602A chassis. The AWG continuously transmits the noise waveform at an output power of 0 dBm. The iid Gaussian noise waveform is then amplified through a Mini-Circuits ZVE-8G+ amplifier having a gain of 30 dB across the operating band of 3–5 GHz. The output of the amplifier is at +30 dBm. The cable between the AWG and the amplifier is 1.52 m (5 ft) long and has 1.6 dB of

insertion loss over the 3-5 GHz frequency range. The amplified waveform is transmitted through an A-Info dual-polarization horn antenna. The dual-polarized horn antenna operates over the frequency range of 2–18 GHz. The antenna has a gain of approximately 10 dB over our 3–5 GHz operating range. There is another 1.6 dB of loss between the amplifier and the antenna due to cable loss. The receiving side of the system uses an identical antenna to collect the scattered power. The receive antenna is connected to an Agilent Infinium DS090804A oscilloscope which has a maximum sampling rate of 40 GSa/s. For this case the oscilloscope sampled at 20 GSa/s. The cable between the receiving antenna and the oscilloscope is 1.83 m (6 ft) long and adds another 2 dB of insertion loss. The oscilloscope then collects and directly samples the reflected waveform and then sends it to the computer for processing. A comparison of the output of the AWG and the reflection from an aluminum cylinder are presented in Figure 2.

TABLE 1: HARDWARE CHARACTERISTICS

3 dB Beamwidth (deg)	44.75-40.07
Antenna Gain	10 dB
Amplifier Gain	30 dB
Cable Insertion Loss	5.2 dB
AWG Output Power	0 dBm

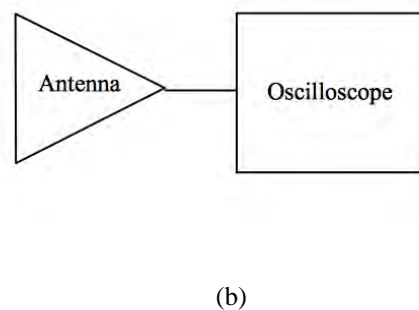
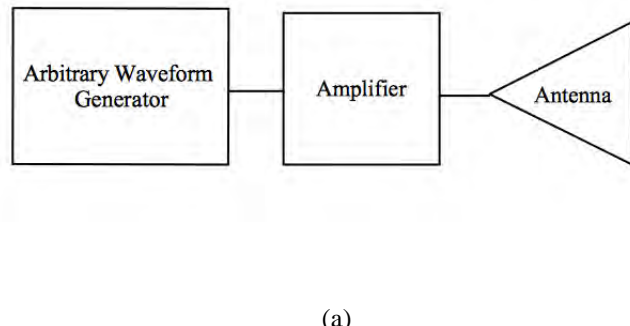
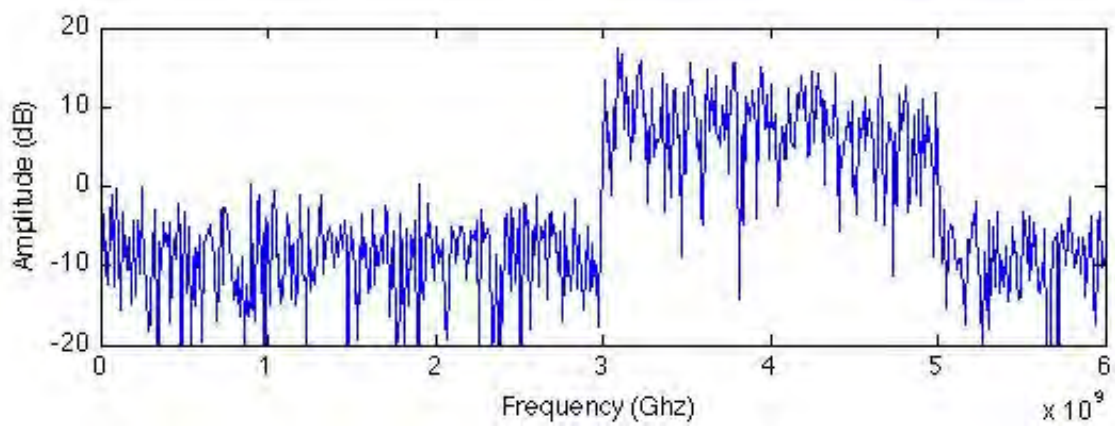
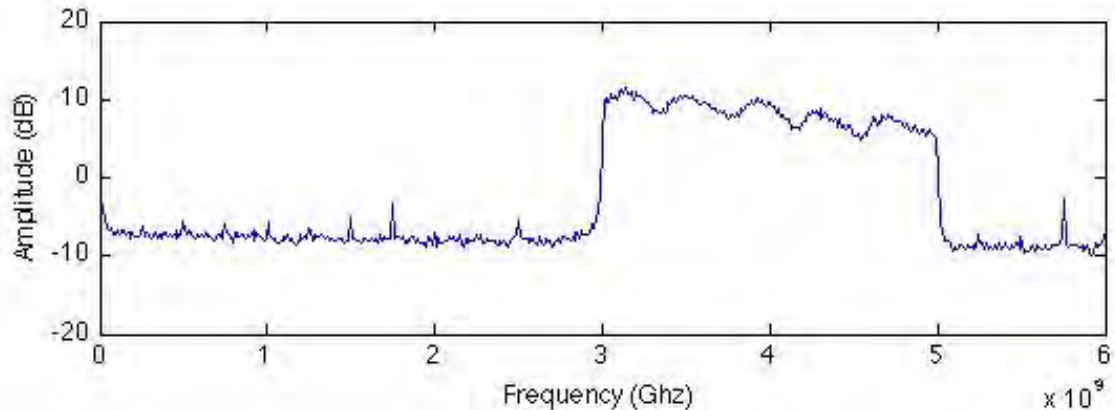


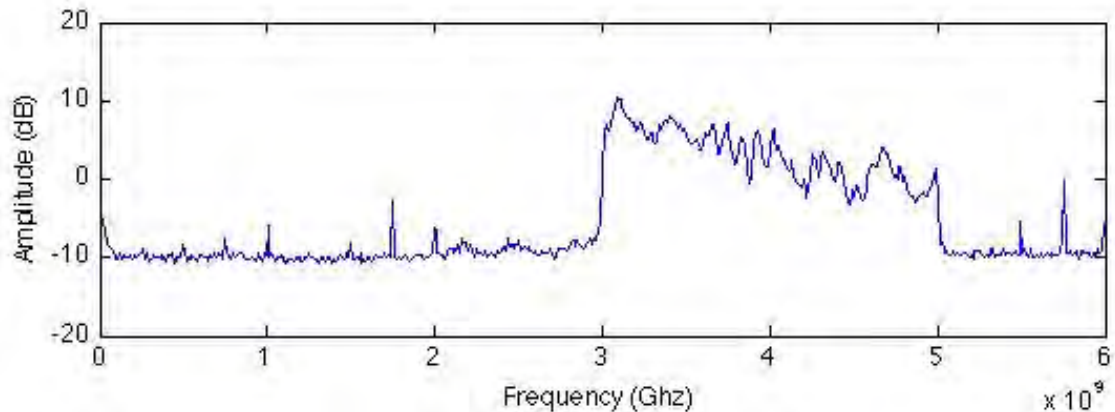
Figure 1: Block diagram of (a) transmitter and (b) receiver.



(a)



(b)



(c)

Figure 2: (a) Noise waveform taken directly out of the AWG, (b) averaged noise waveform taken directly from the AWG, and (c) reflected and averaged waveform off of a metal cylinder.

## 2.2 Turntable and Linear Scanner

The receiving antenna is placed on a linear scanner in place of an antenna array, as shown in Figure 3. The scanner stops at 55 points (locations) for the majority of the collected data. We also experimented with 29 points for the antenna but the image was noticeably

worse than the 55-point image, as shown in Figure 4 for a metallic rectangular box. Therefore, we used 55 points to collect all subsequent data.

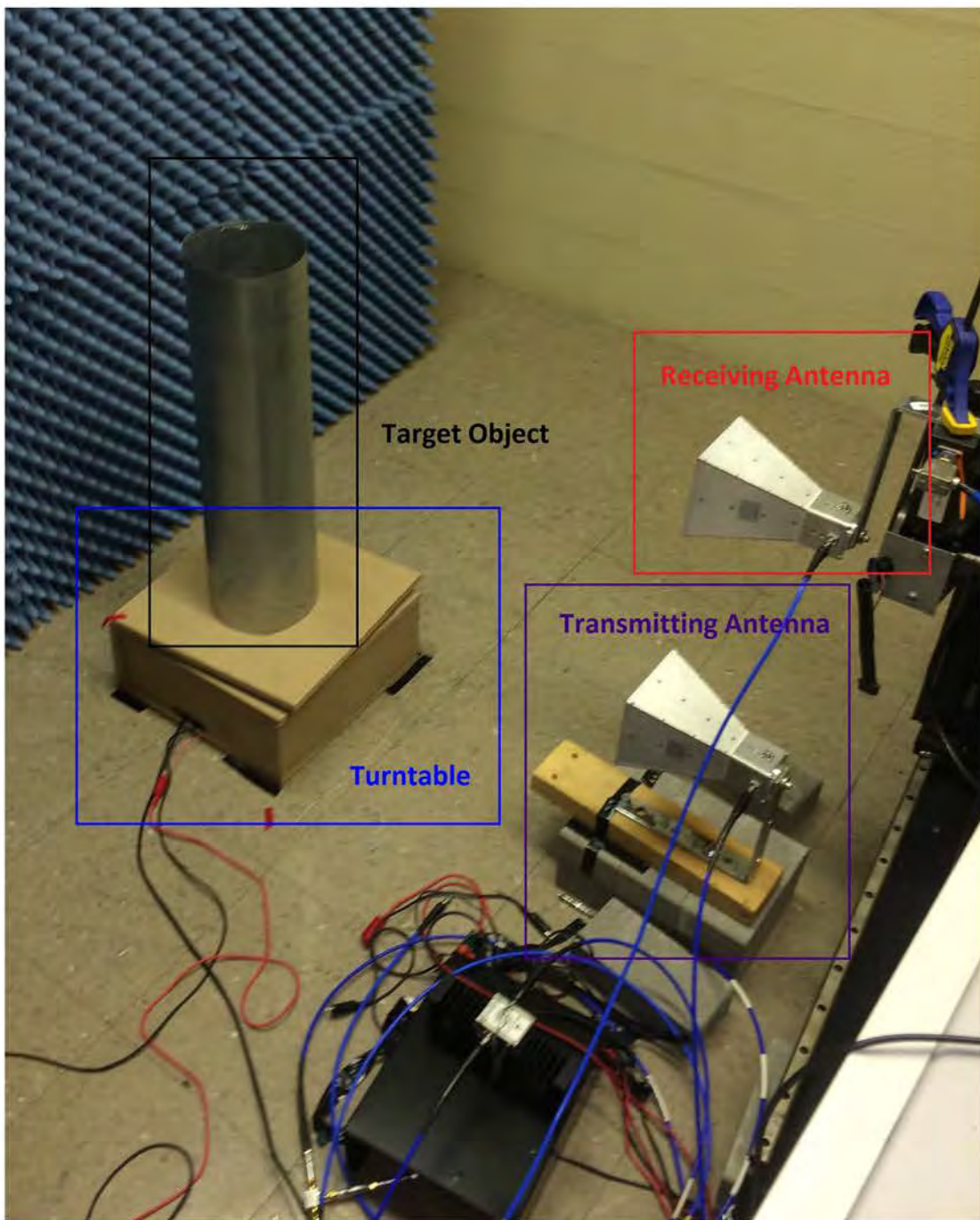


Figure 3: A metal cylinder placed on the turntable. Also shown are the transmitting and receiving antenna and microwave absorber behind the target to minimize reflections from the back.

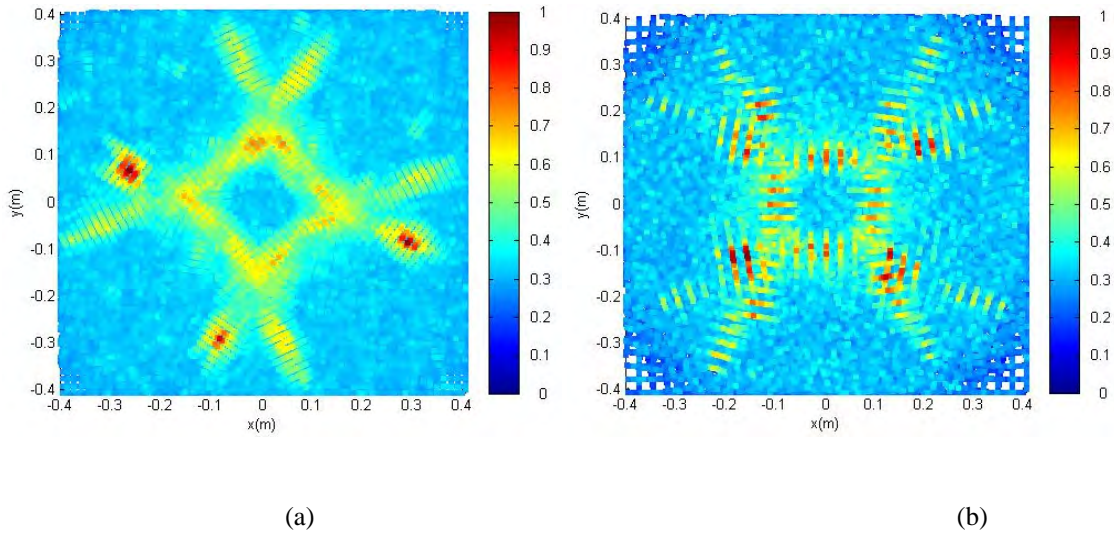


Figure 4: Tomographic image of a metallic rectangular box imaged with (a) 55 lateral points, and (b) 29 lateral points. Note that the imaging with 55 points is much better and cleaner than the one with 29 points. All of the data presented in this document used 55 lateral points for imaging.

The test objects consisted of simple geometric shapes of different sizes. The test objects were made out of two different materials. The metal test objects were constructed from sheets of aluminum. The dielectric objects were made out of solid concrete. The test objects were placed on the center of the turntable one at a time. Table I shows the test objects for which the images are presented herein. The photographic images of the test object are included in the appendix.

TABLE 2: TEST OBJECTS IMAGED BY THE TOMOGRAPHIC NOISE SYSTEM

DESCRIPTION	DIMENSIONS
Metal Rectangular Box 1	20.3 cm × 20.3 cm × 60.96 cm (8" × 8" × 24")
Metal Rectangular Box 2	30.48 cm × 30.48 cm × 30.48 cm (12" × 12" × 12")
Metal Cylinder 1	15.24 cm diameter × 60.96 cm height (6" diameter × 24" height)
Metal Cylinder 2	20.32 cm diameter × 40.64 cm height (8" diameter × 16" height)
Dielectric Rectangular Box	15.24 cm × 15.24 cm × 30.48 cm (6" × 6" × 12")
Dielectric Cylinder	15.24 cm diameter × 30.48 cm height (6" diameter × 12" height)
Dielectric Semicircle	7.62 cm radius × 30.48 cm height (3" radius × 12" height)
Metal Cylinder of Triangular Cross Section	15.24" cm side × 30.48 cm height (6" side × 12" height)

The tomographic images for a metal rectangular box with dimensions  $20.3\text{ cm} \times 20.3\text{ cm} \times 60.96\text{ cm}$  are shown in Figure 4(a). At each point, the antenna stops in order to ensure that the oscilloscope has time to collect a sufficient amount of data. After all 55 point of data are collected, the linear scanner moves back to its initial position. As the linear scanner is moving back to the first point, the turntable rotates by 9 degrees. The linear scanner then starts and stops at the same 55 points as before. This rotation and then linear scan process are continued until the object has rotated by a full 360 degrees. In the data presented in this document, a total of 40 angular measurements are made ( $360 \div 9 = 40$ ). The number of scanning points and the angle of rotation were chosen as a tradeoff between data collection time and image resolution. The turntable is controlled by a stepper motor and is able to rotate in any multiple of 1.8 degrees.

### **3. DATA COLLECTION AND PROCESSING**

The target object is placed on the center of a turntable in front of a wall made of microwave absorbent foam. Both the transmitting and the receiving antennas point towards the foam wall. The turntable is pictured with a metal cylinder on it in Figure 3.

The data collection process starts with the Gaussian noise waveform being uploaded to the AWG. The AWG automatically transmits the most recently uploaded waveform. The noise waveform is not identical between tests. The waveform is also not saved. The processing only requires that the transmitted waveform be iid and white Gaussian. The waveform is then amplified and then transmitted from a stationary antenna located at the center of the window. The linear scanner then moves to each one of the 55 designated points stopping at each one. Each time the linear scanner stops, the oscilloscope collects a total of 363,000 amplitude samples. After a single line scan has been taken, the turntable rotates 9 degrees and the process repeats. The data are stored as they come in and they are then saved in a  $40 \times 363,000$  array for processing at a later point in time.

Each 363,000 point sample is split into 200 segments for processing. The collected waveform has to be split up due to the memory limitations of the computer. Each of the 200 segments is then averaged and processed to create an image. An image is created for each angle at which the turntable stops. For the data presented in this document, there were 40 images created for each object. Using image processing, these 40 images were combined into one final image such as those presented in this document.

A long sample length or the averaging of multiple samples is necessary to achieve a flat frequency spectrum. Fourier diffraction theory is used to construct a tomography image of

the object. If too little data are used, then the spectrum is no longer flat and it is not possible to create a recognizable image. In Figure 2(a), the Fourier transform of a single sample of length 1815 shows that the spectrum is not really flat, as desired. In Figure 2(b), 200 segments are averaged together to create a much flatter frequency spectrum, which has been shown to be absolutely necessary to create a good image<sup>19</sup>.

## 4. EXPERIMENTAL RESULTS

The noise tomography system was used to acquire data from targets with rectangular, cylindrical, and triangular cross sections. The images of the objects were successfully reconstructed. As expected, there is less scattered power from the dielectric test objects compared to the metallic objects.

Figure 5 shows the reconstructed tomographic image of a metal cylinder and a dielectric (i.e. concrete) cylinder. We note that the circular cross-section is clearly seen in both cases. The metal cylinder shows a much stronger and clearer image with very low noise outside its physical extent. In the case of the dielectric cylinder, the shape can be clearly inferred; however, there is observed noise outside its physical extent, owing to its lower scattered power.

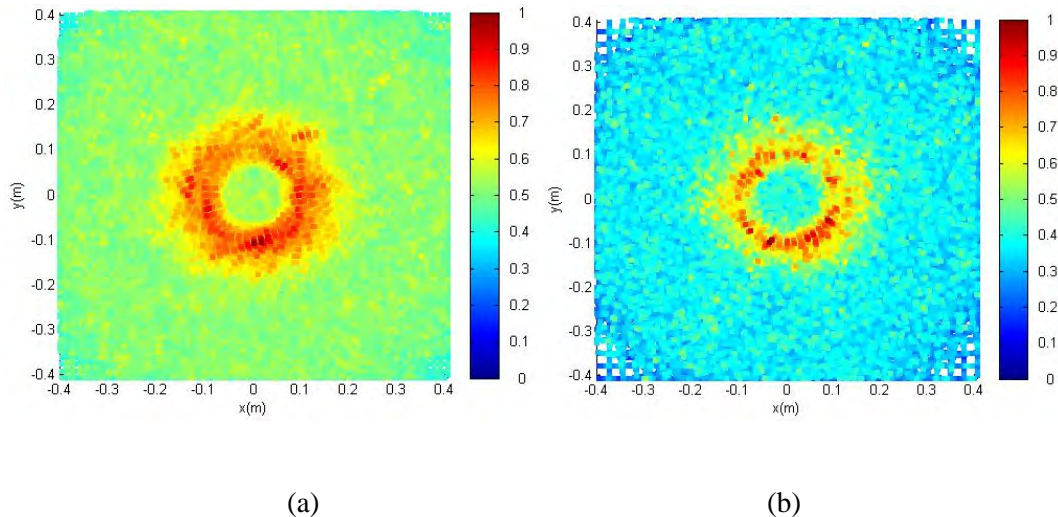


Figure 5: Tomographic image of (a) aluminum cylinder, and (b) dielectric cylinder.

The system also successfully imaged rectangular boxes made of both types of materials, as seen in Figure 6. The rectangular objects have a large amount of diffraction from their edges, which can be seen as plumes. Again, the cross-section of the metal box is well imaged compared to the dielectric box; however, there is more diffraction from the edges of the metal box compared to the dielectric box.

Figure 7 shows the image of a metal cylinder having a triangular cross-section. Its shape can be seen as also the wave diffraction from its edges.

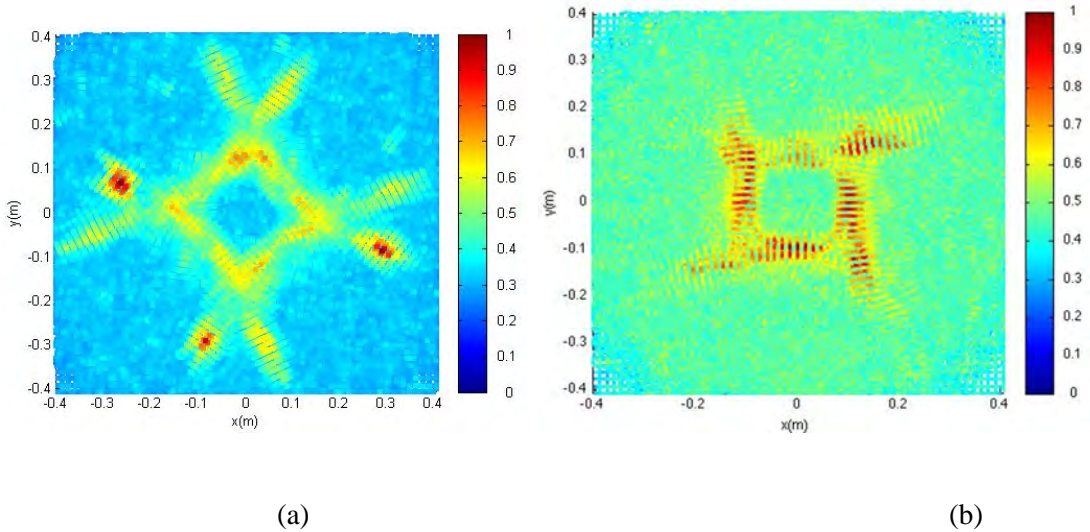


Figure 6: Tomographic image of (a) aluminum rectangular box, and (b) dielectric rectangular box.

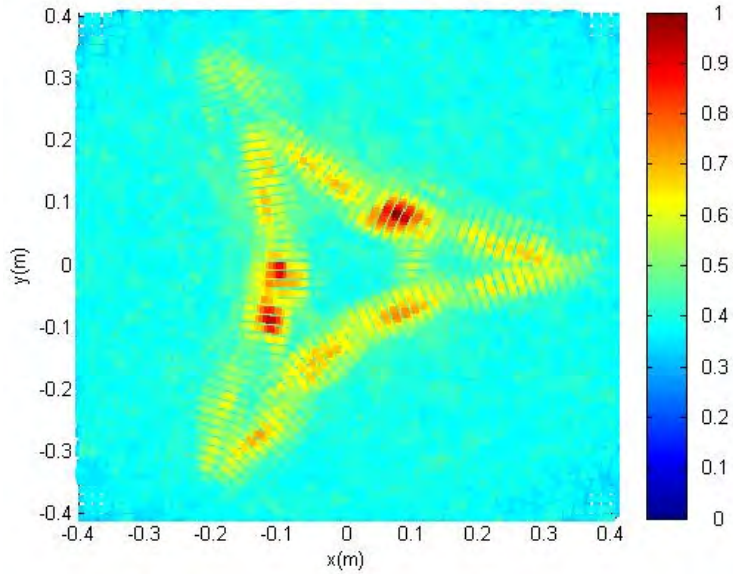


Figure 7: Tomographic image of a triangular metal cylinder.

Some objects were also imaged when concealed within a cardboard box of size 50.8 cm × 40.64 cm × 54.07 cm. Figures 8(a) and 8(b) show the images of metal triangular and circular cylinders inside the cardboard box, respectively. By comparing Figures 7 and 8(a) and also Figures 5(a) and 8(b), it can be observed that while the cardboard adds a small amount of noise, the target object is still clearly visible and discernible.

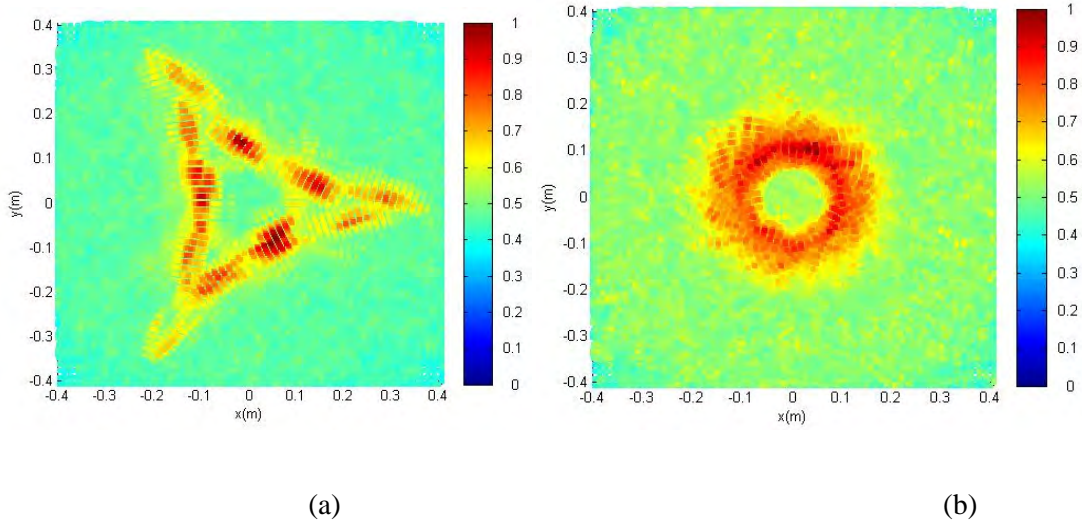
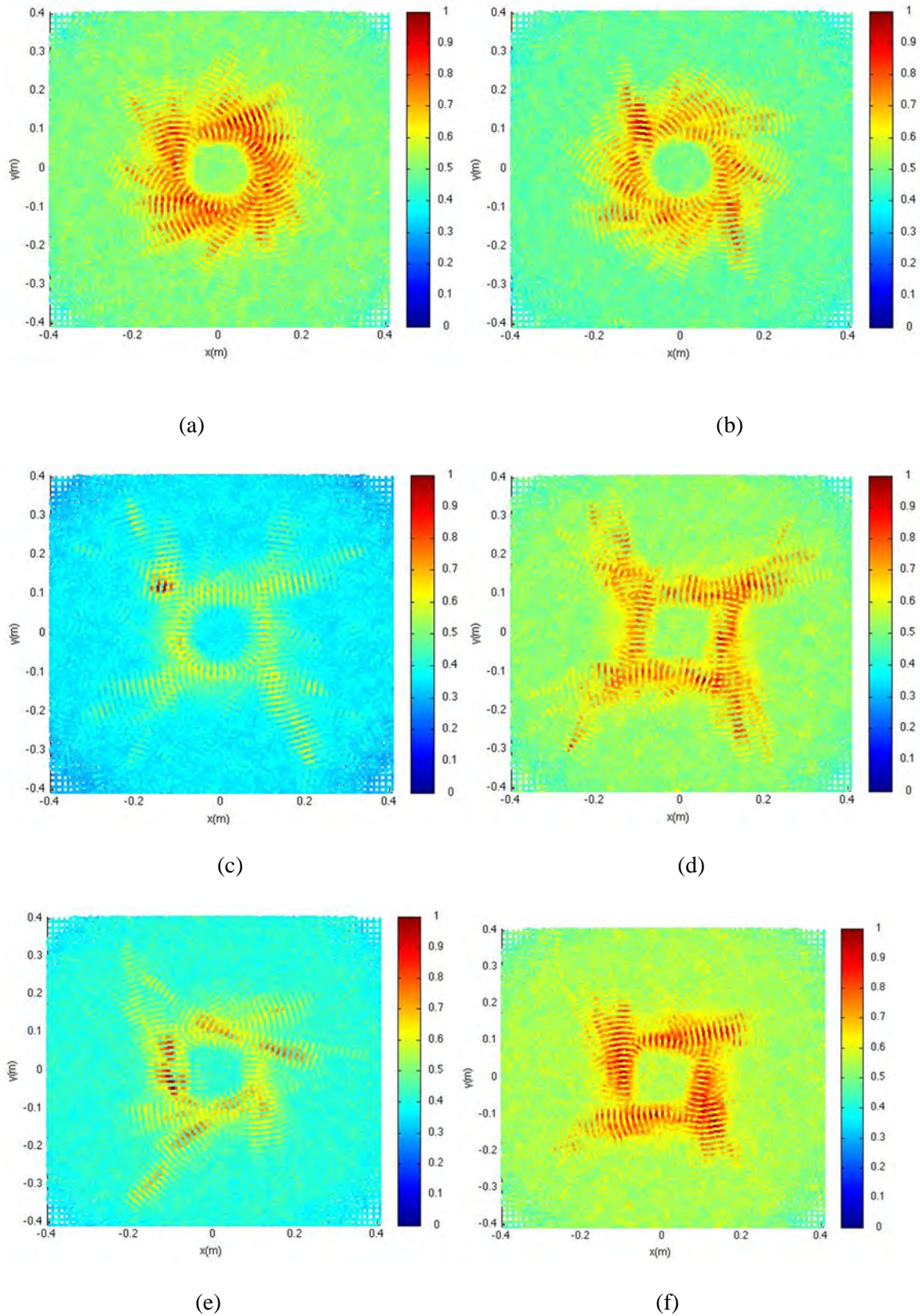


Figure 8: Tomographic image of (a) triangular metal cylinder in a cardboard box, and (b) circular metal cylinder in a cardboard box.

Objects were concealed in a wooden box with sides that are 1.27 cm thick. The dimensions of the box are 38.1 cm x 38.1 cm x 38.1 cm. Figure 9 a-e shows metal objects in the wooden box. The wooden box adds more noise but the target objects are still visible and recognizable.



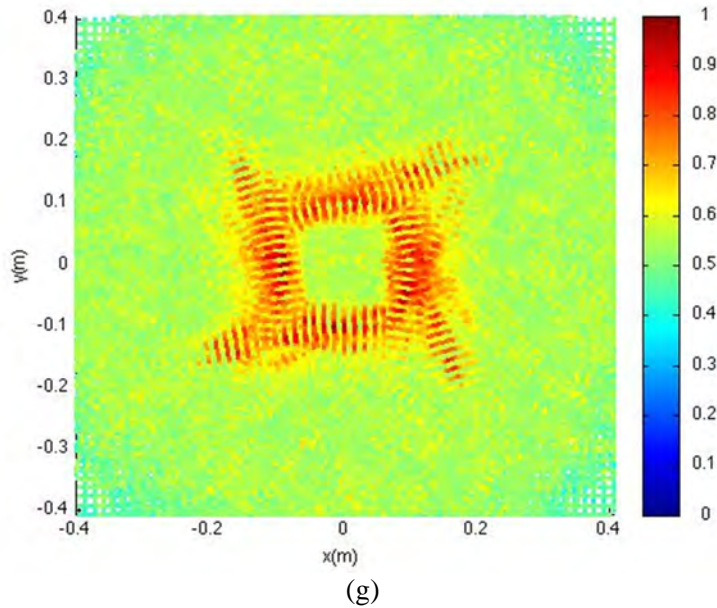


Figure 9: Tomographic image of (a) metal cylinder 1, (b) metal cylinder 2, (c) metal rectangular box 1, (d) metal rectangular box 2, (e) metal cylinder with triangular cross section, (f) dielectric cylinder, and (g) dielectric rectangular box. These objects are concealed in a wooden box.

## 5. FUTURE WORK AND CONCLUSIONS

### 5.1 Future Work

Some work has been done towards developing a higher frequency version of the noise radar tomography system. The system operates from 8-10 GHz. The block diagram for the transmit and the receive portions of the system are shown in Figures 10 and 11. The computer uploads an iid Gaussian Noise Waveform to the AWG. The AWG is an Agilent M8190A system mounted on a M9602A chassis. The AWG continuously transmits the noise waveform at an output power of 0 dBm. The Gaussian waveform is transmitted at 2-4 GHz through two Minicircuit filters. The waveform is then mixed with a 6 GHz tone from a signal generator. 3 dB attenuators are located on each terminal of the mixer. The resulting waveform is 8-10 GHz. The waveform is then filtered again before being transmitted through two cascaded amplifiers. The amplifiers have a 7 dB attenuator in between them to prevent saturation in the second amplifier. The first amplifier is a Mini-Circuits ZX60-24-S+ with a gain of 24 dB. The second amplifier is a Miteq AMF-5B-8012-29P with a gain of 28 dB. The waveform is finally transmitted through an A-Info dual-polarized horn antenna.

An identical antenna is used to collect the backscatter off of the target object. The waveform is amplified using a Minicircuits ZX60-24-S+ with gain 24 dB. The waveform is then filtered and passed to the Agilent Infinium DS090804A oscilloscope.

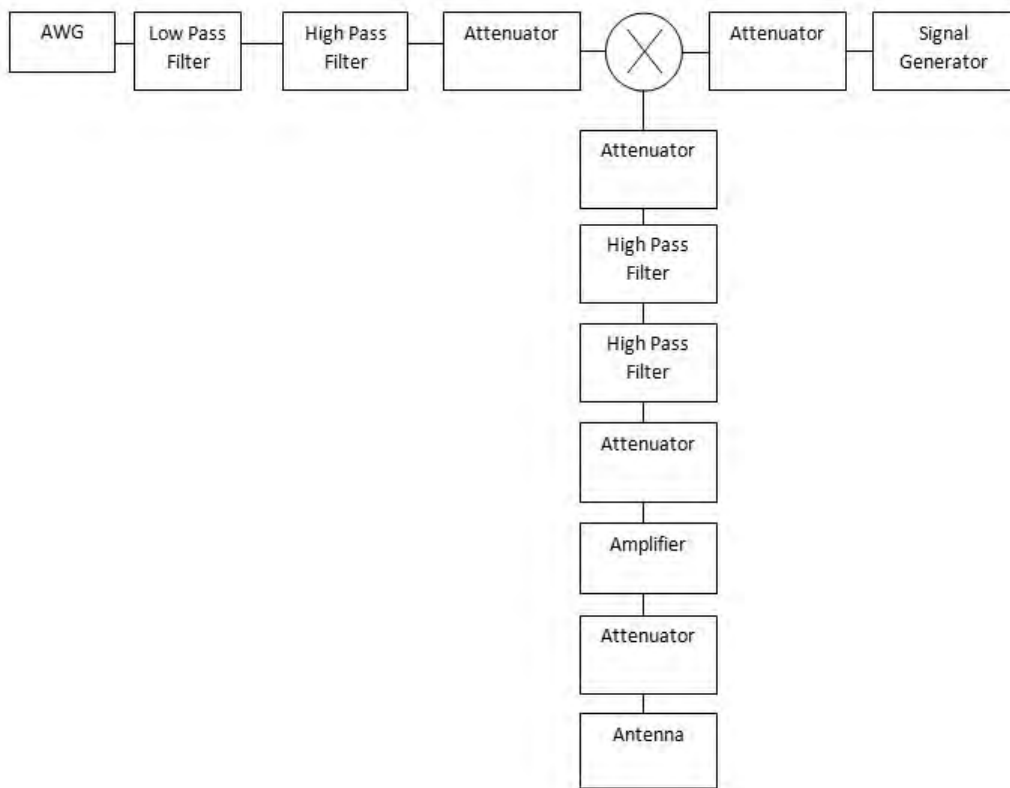


Figure 10 : High frequency transmitting system.

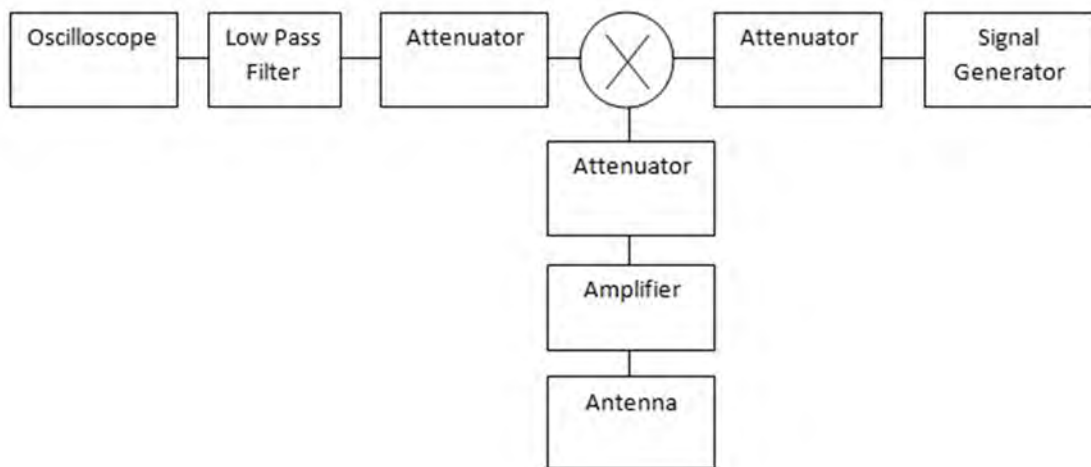


Figure 11: High frequency receiving system.

## **5.2 Conclusions**

The UWB noise tomography hardware system designed by us was able to successfully image a variety of shapes and materials using a relatively simple setup. It was demonstrated that an iid WGN waveform can be used to correctly image target objects. This shows that radar tomography can be accomplished while maintaining LPI and LPD properties. This document described a successful data collection system for noise radar tomography. Even with obstructions such as a wooden box, the system was able to image objects quite clearly.

## Appendix A Images of Test Objects

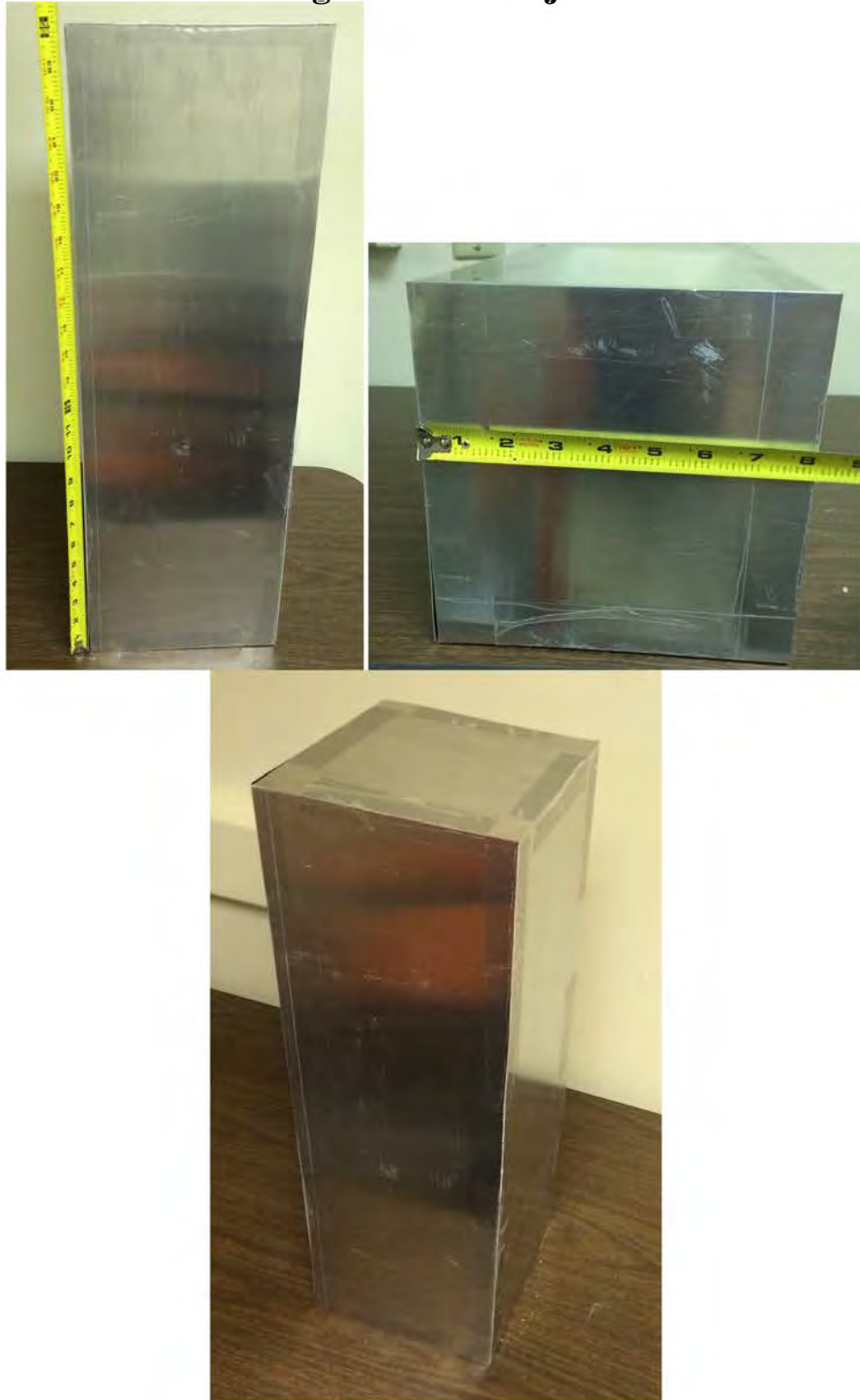


Figure 12: Metal Rectangular Box 1.

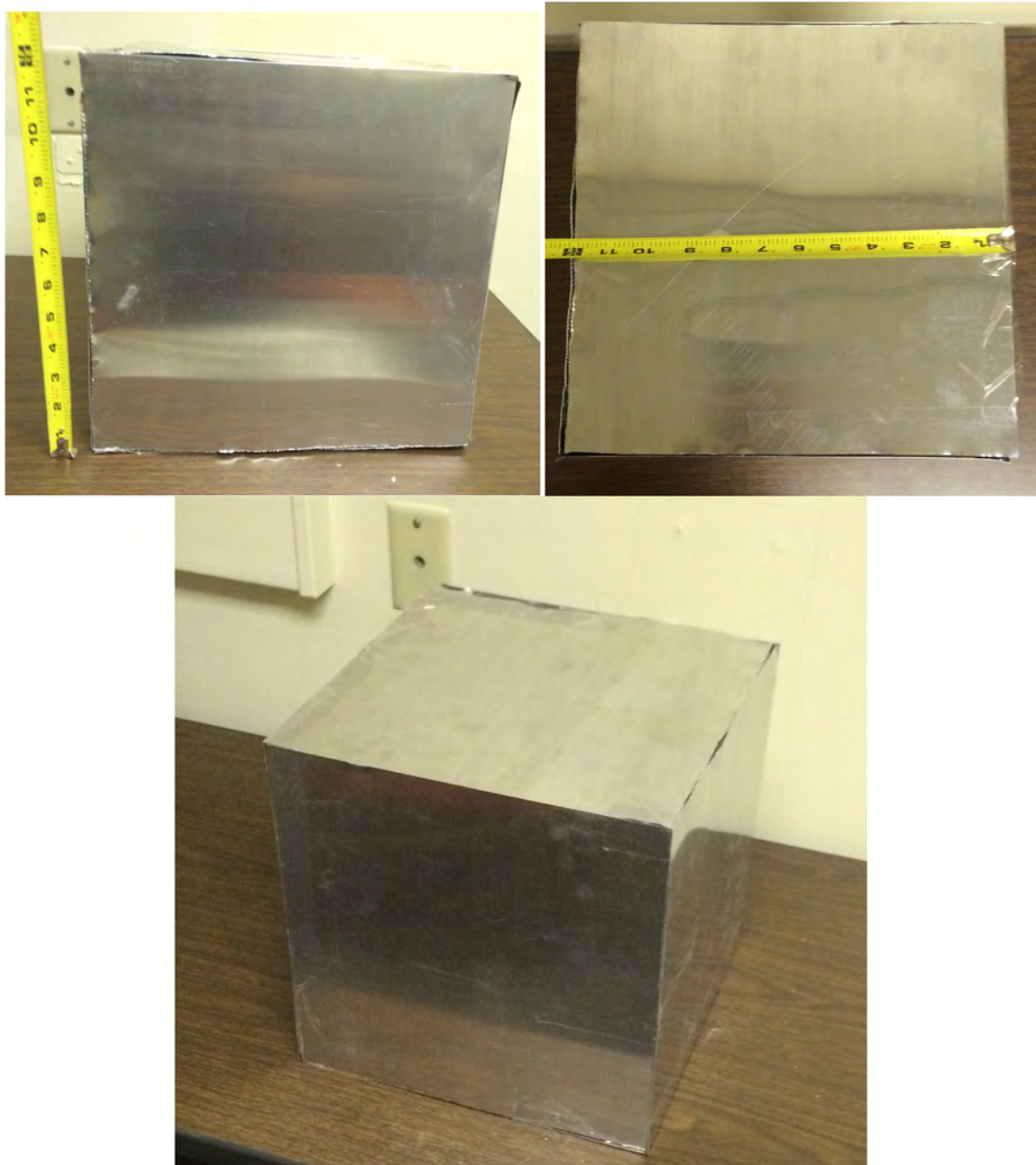


Figure 13: Metal Rectangular Box 2.



Figure 14: Metal Cylinder 1.



Figure 15: Metal Cylinder 2.



Figure 16: Dielectric Rectangular Box.



Figure 17: Dielectric Circular Cylinder.



Figure 18: Dielectric Semicircular Cylinder.

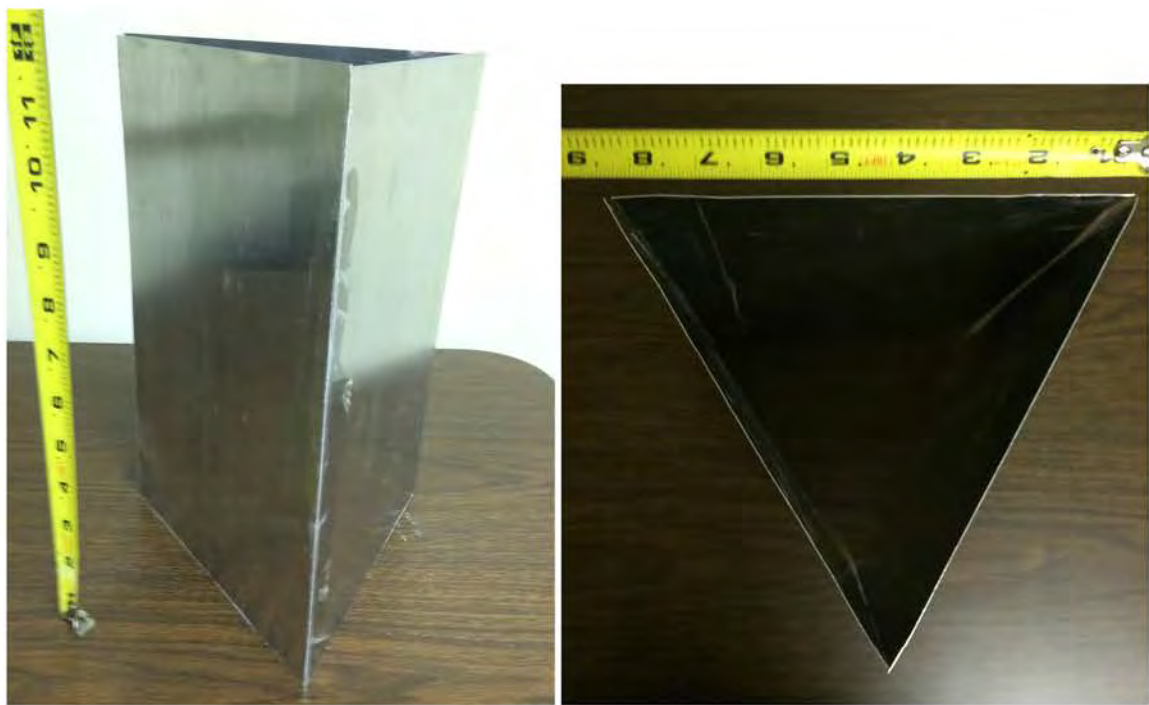


Figure 20: Metal Cylinder of Triangular Cross Section.

## Appendix B

### Computer Programs

```
% Original code written by Scott Wilson modified for radar
tomography by Mark Asmuth
function varargout = ScannerGUI(varargin)
% SCANNERGUI M-file for ScannerGUI.fig
%     SCANNERGUI, by itself, creates a new SCANNERGUI or
raises the existing
%     singleton*.
%
%     H = SCANNERGUI returns the handle to a new SCANNERGUI
or the handle to
%     the existing singleton*.
%
%     SCANNERGUI( 'CALLBACK' ,hObject,eventData,handles,... )
calls the local
%     function named CALLBACK in SCANNERGUI.M with the
given input arguments.
%
%     SCANNERGUI('Property','Value',...) creates a new
SCANNERGUI or raises the
%     existing singleton*. Starting from the left,
property value pairs are
%     applied to the GUI before ScannerGUI_OpeningFcn gets
called. An
%     unrecognized property name or invalid value makes
property application
%     stop. All inputs are passed to ScannerGUI_OpeningFcn
via varargin.
%
%     *See GUI Options on GUIDE's Tools menu. Choose "GUI
allows only one
%     instance to run (singleton)".
%
% See also: GUIDE, GUIDATA, GUIHANDLES

% Edit the above text to modify the response to help
ScannerGUI

% Last Modified by GUIDE v2.5 29-Oct-2013 14:16:00

% Begin initialization code - DO NOT EDIT
gui_Singleton = 1;
gui_State = struct('gui_Name',          mfilename, ...
                   'gui_Singleton',    gui_Singleton, ...
                   'gui_OpeningFcn',   @ScannerGUI_OpeningFcn,
...

```

```

'gui_OutputFcn', @ScannerGUI_OutputFcn,
...
'gui_LayoutFcn', [], ...
'gui_Callback', []);

if nargin && ischar(varargin{1})
    gui_State.gui_Callback = str2func(varargin{1});
end

if narginout
    [varargout{1:narginout}] = gui_mainfcn(gui_State,
varargin{:});
else
    gui_mainfcn(gui_State, varargin{:});
end
% End initialization code - DO NOT EDIT

%%%%%%%%%%%%%%%
%%%%%%%
% --- Executes just before ScannerGUI is made visible.
function ScannerGUI_OpeningFcn(hObject, eventdata, handles,
varargin)
% This function has no output args, see OutputFcn.
% hObject    handle to figure
% eventdata   reserved - to be defined in a future version of
MATLAB
% handles    structure with handles and user data (see
GUIDATA)
% varargin    command line arguments to ScannerGUI (see
VARARGIN)

% Choose default command line output for ScannerGUI
handles.output = hObject;
set(gcf, 'CloseRequestFcn', @CloseGuiFcn)

handles.root_dir = 'C:\Holograms2\';

axes(handles.holAxes);
axis image;
% colormap(bone);
axes(handles.imAxes);
axis image;
% colormap(bone);

try
% OSC = visa('agilent', 'GPIB0::8::INSTR');
%
% handles.OSC = OSC;
% set(OSC, 'InputBufferSize', 1e8);
% OSC.Timeout=10;
% OSC.ByteOrder='littleEndian';
%
% fopen(OSC);

```

```

% fprintf(OSC,'*RST; :AUTOSCALE');
% idn='Oscilloscope';

OSC = visa('agilent', 'TCPIP::130.203.252.125::INSTR');

handles.OSC = OSC;
set(OSC, 'InputBufferSize', 1e7);
set(OSC, 'timeout', 20);
OSC.Timeout=20;
OSC.ByteOrder='littleEndian';

fopen(OSC);
fprintf(OSC,'*RST; :AUTOSCALE');
idn='Oscilloscope';
msg = msgbox(['Connected to ',idn], 'OSC Connected');
osc= handles.OSC;
set(handles.vnaConnStatText, 'String', 'Connected', 'Foreground
Color', 'g');
fprintf(osc,'*RST; :AUTOSCALE');

fprintf(osc,:WAVEFORM:SOURCE CHAN1);           % Specify data
from Channel 1

% Set up VNA frequency scale
fprintf(osc,:TIMEBASE:REFERENCE CENTER);      % Display
reference at center
fprintf(osc,:TIMEBASE:RANGE 1e-5);            % Time base to
100 ns full scale
fprintf(osc,:TIMEBASE:DELAY 0');                % Delay to zero
fprintf(osc,:CHANNEL1:RANGE 2.5');              % Vertical
range to 1.6 V full scale
fprintf(osc,:CHANNEL1:OFFSET 0');
fprintf(osc,:WAVEFORM:TYPE? RAW');
fprintf(osc,:ACQUIRE:POINTS 363000');
fprintf(osc,:WAVEFORM:BYTEORDER LSBFirst');    % Set the byte
order on the instrument as well
pause(10);
uiwait(msg);
catch ME
    msg = msgbox('Unable to connect to GPIB0::8:INSTR
!', 'Connection Error');
    uiwait(msg);
end

try
    s = serial('COM10','BaudRate',9600);        % Connect to
Arduino via Serial
    handles.s = s;

    set(s,'InputBufferSize',512);
    fopen(s);    % Open serial port

set(handles.scanConnStatText, 'String', 'Connected', 'Foreground
Color', 'g');

```



```

MATLAB
% handles      structure with handles and user data (see
GUIDATA)

% Get default command line output from handles structure
varargout{1} = handles.output;

%
% -----
%
function menuBar_Callback(hObject, eventdata, handles)
% hObject      handle to menuFile (see GCBO)
% eventdata    reserved - to be defined in a future version of
MATLAB
% handles      structure with handles and user data (see
GUIDATA)

%
% -----
%
function menuFile_Callback(hObject, eventdata, handles)
% hObject      handle to menuFile (see GCBO)
% eventdata    reserved - to be defined in a future version of
MATLAB
% handles      structure with handles and user data (see
GUIDATA)

%
% -----
%
function menuEdit_Callback(hObject, eventdata, handles)
% hObject      handle to menuEdit (see GCBO)
% eventdata    reserved - to be defined in a future version of
MATLAB
% handles      structure with handles and user data (see
GUIDATA)

%
% -----
%
function editParams_Callback(hObject, eventdata, handles)
% hObject      handle to editParams (see GCBO)
% eventdata    reserved - to be defined in a future version of
MATLAB
% handles      structure with handles and user data (see
GUIDATA)

%
% -----
%
function editSave_Callback(hObject, eventdata, handles)
% hObject      handle to editSave (see GCBO)
% eventdata    reserved - to be defined in a future version of
MATLAB

```

```

% handles      structure with handles and user data (see
GUIDATA)

%%%%%%%%%%%%%
%%% --- Executes on slider movement.
function fSlider_Callback(hObject, eventdata, handles)
% hObject    handle to fSlider (see GCBO)
% eventdata  reserved - to be defined in a future version of
MATLAB
% handles      structure with handles and user data (see
GUIDATA)

% Hints: get(hObject,'Value') returns position of slider
%         get(hObject,'Min') and get(hObject,'Max') to
determine range of slider

try

NofFreqs = length(handles.freqs);

if(NofFreqs > 1)
    set(handles.fSlider, 'Visible', 'on');
    f_ind = get(handles.fSlider, 'Value');

set(handles.fSliderText, 'String', num2str(handles.freqs(f_ind
)/10^9,2));
else
    set(handles.fSlider, 'Visible', 'off');
end

axes(handles.imAxes);
imagesc(handles.x, handles.y,
abs(handles.recon_data(:,:,f_ind)));
colormap(bone)
axes(handles.holAxes);
imagesc(handles.x, handles.y,
abs(handles.hol_data(:,:,f_ind))/(2*pi));
colormap(bone)

catch ME
end

%%%%%%%%%%%%%

```

```

%%%%%
% --- Executes on slider movement.
function zSlider_Callback(hObject, eventdata, handles)
% hObject    handle to zSlider (see GCBO)
% eventdata   reserved - to be defined in a future version of
MATLAB
% handles    structure with handles and user data (see
GUIDATA)

% Hints: get(hObject,'Value') returns position of slider
%         get(hObject,'Min') and get(hObject,'Max') to
determine range of slider

z = get(handles.zSlider,'Value');
set(handles.zSliderText,'String',num2str(z,3));

zo = z;

NoffFreqs = length(handles.freqs);
if(NoffFreqs > 1)
    set(handles.fSlider,'Visible','on');
    f_ind = get(handles.fSlider,'Value');
else
    set(handles.fSlider,'Visible','off');
end

x = handles.x * handles.dx;
y = handles.y * handles.dy;

if(NoffFreqs > 1)
    handles.recon_data = Fourier3D(handles.hol_data, [], [], handles.kz, zo);

    axes(handles.imAxes);
    imagesc(handles.x, handles.y,
abs(handles.recon_data(:,:,:f_ind)));
    axes(handles.holAxes);
    imagesc(handles.x, handles.y,
abs(handles.hol_data(:,:,:f_ind)));

else
    handles.recon_data = Fourier2D(handles.hol_data,
handles.kz, zo);

    axes(handles.imAxes);
    imagesc(x, y, abs(handles.recon_data));
    axes(handles.holAxes);
    imagesc(x, y, abs(handles.hol_data));
end

% Update handles structure
guidata(hObject, handles);

```



```

    set(handles.zSlider, 'Min', 0);
    set(handles.zSlider, 'Max', 2);
    set(handles.zSlider, 'SliderStep', [0.005 0.1]);

    if(NoffFreqs > 1)
        set(handles.fSlider, 'Visible','on');
        set(handles.fSlider, 'Value',1);
        set(handles.fSlider, 'Min',1);
        set(handles.fSlider, 'Max',NoffFreqs);
        set(handles.fSlider, 'SliderStep', [1/(NoffFreqs-1)
0.1]);
        temp = get(handles.fSlider, 'Value') * (NoffFreqs-1) +
1;
    else
        set(handles.fSlider, 'Visible','off');
    end

    catch ME
        set(handles.zSlider, 'Max',1);
        set(handles.zSlider, 'SliderStep', [0.01 0.1]);
        set(handles.fSlider, 'Min',0);
        set(handles.fSlider, 'Max',NoffFreqs);
        set(handles.fSlider, 'SliderStep', [0.1 0.1]);
    end

    Nx = length(handles.x);
    Ny = length(handles.y);

    [handles.kx handles.ky handles.kz] =
calc_wavenums(handles.freqs, Ny, Nx);
    zo = Root.zo(1);

%     hol_data_cart =
sphere2cart_gridinterp(handles.hol_data,handles.freqs);
if(NoffFreqs > 1)
    handles.recon_data = Fourier3D(handles.hol_data,
handles.kx, handles.ky, handles.kz, zo);
else
    handles.recon_data = Fourier2D(handles.hol_data,
handles.kz, zo);
end

%     handles.est_targ_dist =
estimate_target_distance(handles.recon_data);
else
    msgbox('Please select a data file.', 'Unable to load
file');
end

% Update handles structure
guidata(hObject, handles);

```

```
%-----%
```

```
% --- Executes during object creation, after setting all
properties.
function zSlider_CreateFcn(hObject, eventdata, handles)
% hObject    handle to zSlider (see GCBO)
% eventdata   reserved - to be defined in a future version of
MATLAB
% handles    empty - handles not created until after all
CreateFcns called
```

```
% Hint: slider controls usually have a light gray
background.
if isequal(get(hObject,'BackgroundColor'),
get(0,'defaultUicontrolBackgroundColor'))
    set(hObject,'BackgroundColor',[.9 .9 .9]);
end
```

```
% --- Executes during object creation, after setting all
properties.
function fSlider_CreateFcn(hObject, eventdata, handles)
% hObject    handle to fSlider (see GCBO)
% eventdata   reserved - to be defined in a future version of
MATLAB
% handles    empty - handles not created until after all
CreateFcns called
```

```
% Hint: slider controls usually have a light gray
background.
if isequal(get(hObject,'BackgroundColor'),
get(0,'defaultUicontrolBackgroundColor'))
    set(hObject,'BackgroundColor',[.9 .9 .9]);
end
```

```
% --- Executes on button press in render3dBtn.
function render3dBtn_Callback(hObject, eventdata, handles)
% hObject    handle to render3dBtn (see GCBO)
% eventdata   reserved - to be defined in a future version of
MATLAB
% handles    structure with handles and user data (see
GUIDATA)
```

```

figure;
isosurface(abs(handles.recon_data));

%%%%%%%%%%%%%%%
% --- Executes on button press in startScanBtn.
function startScanBtn_Callback(hObject, eventdata, handles)
% hObject    handle to startScanBtn (see GCBO)
% eventdata   reserved - to be defined in a future version of
MATLAB
% handles    structure with handles and user data (see
GUIDATA)

pause(2);

x_max = str2double(get(handles.scanWidthText,'String'));
y_max = str2double(get(handles.scanWidthText,'String'));
angle = 0; % = 90; % H-pol or V-pol
m = str2double(get(handles.XsamplesText,'String'));
n = str2double(get(handles.YsamplesText,'String'));

handles.x_max = x_max;
handles.y_max = y_max;
handles.m = m;
handles.n = n;
handles.x = linspace(0,x_max,m);
handles.y = linspace(0,y_max,n);

handles.angle = angle;

axes(handles.holAxes);
imagesc(zeros(m,n));

[file p_data p_ind] = create_position_data(m, n, x_max,
y_max, angle);

handles.p_ind = p_ind; % indices for scan position
handles.a_data = check_position_data(p_data);

handles.hol_data = run_scan(hObject, handles);

handles.lastSavePath = save_hol_data(handles);

axes(handles.imAxes);

% Update handles structure
guidata(hObject, handles);

%%%%%%%%%%%%%%

```

```

% --- Executes on button press in browseBtn.
function pushbutton4_Callback(hObject, eventdata, handles)
% hObject    handle to browseBtn (see GCBO)
% eventdata   reserved - to be defined in a future version of
MATLAB
% handles    structure with handles and user data (see
GUIDATA)

function fileTextbox_Callback(hObject, eventdata, handles)
% hObject    handle to fileTextbox (see GCBO)
% eventdata   reserved - to be defined in a future version of
MATLAB
% handles    structure with handles and user data (see
GUIDATA)

% Hints: get(hObject,'String') returns contents of
fileTextbox as text
%         str2double(get(hObject,'String')) returns contents
of fileTextbox as a double

% --- Executes during object creation, after setting all
properties.
function fileTextbox_CreateFcn(hObject, eventdata, handles)
% hObject    handle to fileTextbox (see GCBO)
% eventdata   reserved - to be defined in a future version of
MATLAB
% handles    empty - handles not created until after all
CreateFcns called

% Hint: edit controls usually have a white background on
Windows.
%       See ISPC and COMPUTER.
if ispc && isequal(get(hObject,'BackgroundColor'),
get(0,'defaultUicontrolBackgroundColor'))
    set(hObject,'BackgroundColor','white');
end

%%%%%%%%%%%%%%%
% --- Executes on button press in browseBtn.

```



```

function ScanHeightBox_Callback(hObject, eventdata, handles)
% hObject    handle to ScanHeightBox (see GCBO)
% eventdata   reserved - to be defined in a future version of
MATLAB
% handles    structure with handles and user data (see
GUIDATA)

% Hints: get(hObject,'String') returns contents of
ScanHeightBox as text
%         str2double(get(hObject,'String')) returns contents
of ScanHeightBox as a double

% --- Executes during object creation, after setting all
properties.
function ScanHeightBox_CreateFcn(hObject, eventdata,
handles)
% hObject    handle to ScanHeightBox (see GCBO)
% eventdata   reserved - to be defined in a future version of
MATLAB
% handles    empty - handles not created until after all
CreateFcns called

% Hint: edit controls usually have a white background on
Windows.
%       See ISPC and COMPUTER.
if ispc && isequal(get(hObject,'BackgroundColor'),
get(0,'defaultUicontrolBackgroundColor'))
    set(hObject,'BackgroundColor','white');
end


function XsamplesBox_Callback(hObject, eventdata, handles)
% hObject    handle to XsamplesBox (see GCBO)
% eventdata   reserved - to be defined in a future version of
MATLAB
% handles    structure with handles and user data (see
GUIDATA)

% Hints: get(hObject,'String') returns contents of
XsamplesBox as text
%         str2double(get(hObject,'String')) returns contents
of XsamplesBox as a double

% --- Executes during object creation, after setting all
properties.
function XsamplesBox_CreateFcn(hObject, eventdata, handles)
% hObject    handle to XsamplesBox (see GCBO)
% eventdata   reserved - to be defined in a future version of
MATLAB
% handles    empty - handles not created until after all

```

```

CreateFcns called

% Hint: edit controls usually have a white background on
Windows.
%       See ISPC and COMPUTER.
if ispc && isequal(get(hObject, 'BackgroundColor'),
get(0, 'defaultUicontrolBackgroundColor'))
    set(hObject, 'BackgroundColor', 'white');
end

function YsamplesBox_Callback(hObject, eventdata, handles)
% hObject    handle to YsamplesBox (see GCBO)
% eventdata   reserved - to be defined in a future version of
MATLAB
% handles    structure with handles and user data (see
GUIDATA)

% Hints: get(hObject,'String') returns contents of
YsamplesBox as text
%       str2double(get(hObject,'String')) returns contents
of YsamplesBox as a double

% --- Executes during object creation, after setting all
properties.
function YsamplesBox_CreateFcn(hObject, eventdata, handles)
% hObject    handle to YsamplesBox (see GCBO)
% eventdata   reserved - to be defined in a future version of
MATLAB
% handles    empty - handles not created until after all
CreateFcns called

% Hint: edit controls usually have a white background on
Windows.
%       See ISPC and COMPUTER.
if ispc && isequal(get(hObject, 'BackgroundColor'),
get(0, 'defaultUicontrolBackgroundColor'))
    set(hObject, 'BackgroundColor', 'white');
end

% --- Executes on button press in SingleFreqRadio.
function SingleFreqRadio_Callback(hObject, eventdata,
handles)
% hObject    handle to SingleFreqRadio (see GCBO)
% eventdata   reserved - to be defined in a future version of
MATLAB
% handles    structure with handles and user data (see
GUIDATA)

% Hint: get(hObject,'Value') returns toggle state of
SingleFreqRadio

```

```

% --- Executes on button press in MultiFreqRadio.
function MultiFreqRadio_Callback(hObject, eventdata,
handles)
% hObject    handle to MultiFreqRadio (see GCBO)
% eventdata   reserved - to be defined in a future version of
MATLAB
% handles    structure with handles and user data (see
GUIDATA)

% Hint: get(hObject,'Value') returns toggle state of
MultiFreqRadio


function stopFreqBox_Callback(hObject, eventdata, handles)
% hObject    handle to stopFreqBox (see GCBO)
% eventdata   reserved - to be defined in a future version of
MATLAB
% handles    structure with handles and user data (see
GUIDATA)

% Hints: get(hObject,'String') returns contents of
stopFreqBox as text
%         str2double(get(hObject,'String')) returns contents
of stopFreqBox as a double


% --- Executes during object creation, after setting all
properties.
function stopFreqBox_CreateFcn(hObject, eventdata, handles)
% hObject    handle to stopFreqBox (see GCBO)
% eventdata   reserved - to be defined in a future version of
MATLAB
% handles    empty - handles not created until after all
CreateFcns called

% Hint: edit controls usually have a white background on
Windows.
%       See ISPC and COMPUTER.
if ispc && isequal(get(hObject,'BackgroundColor'),
get(0,'defaultUicontrolBackgroundColor'))
    set(hObject,'BackgroundColor','white');
end


function startFreqBox_Callback(hObject, eventdata, handles)
% hObject    handle to startFreqBox (see GCBO)
% eventdata   reserved - to be defined in a future version of
MATLAB
% handles    structure with handles and user data (see
GUIDATA)
```

```

% Hints: get(hObject,'String') returns contents of
startFreqBox as text
% str2double(get(hObject,'String')) returns contents
of startFreqBox as a double

% --- Executes during object creation, after setting all
properties.
function startFreqBox_CreateFcn(hObject, eventdata, handles)
% hObject    handle to startFreqBox (see GCBO)
% eventdata reserved - to be defined in a future version of
MATLAB
% handles    empty - handles not created until after all
CreateFcns called

% Hint: edit controls usually have a white background on
Windows.
% See ISPC and COMPUTER.
if ispc && isequal(get(hObject,'BackgroundColor'),
get(0,'defaultUicontrolBackgroundColor'))
    set(hObject,'BackgroundColor','white');
end


function FsamplesBox_Callback(hObject, eventdata, handles)
% hObject    handle to FsamplesBox (see GCBO)
% eventdata reserved - to be defined in a future version of
MATLAB
% handles    structure with handles and user data (see
GUIDATA)

% Hints: get(hObject,'String') returns contents of
FsamplesBox as text
% str2double(get(hObject,'String')) returns contents
of FsamplesBox as a double

% --- Executes during object creation, after setting all
properties.
function FsamplesBox_CreateFcn(hObject, eventdata, handles)
% hObject    handle to FsamplesBox (see GCBO)
% eventdata reserved - to be defined in a future version of
MATLAB
% handles    empty - handles not created until after all
CreateFcns called

% Hint: edit controls usually have a white background on
Windows.
% See ISPC and COMPUTER.
if ispc && isequal(get(hObject,'BackgroundColor'),
get(0,'defaultUicontrolBackgroundColor'))
    set(hObject,'BackgroundColor','white');

```

```

end

% --- Executes on button press in abortScanBtn.
function abortScanBtn_Callback(hObject, eventdata, handles)
% hObject    handle to abortScanBtn (see GCBO)
% eventdata   reserved - to be defined in a future version of
MATLAB
% handles    structure with handles and user data (see
GUIDATA)

function scanWidthText_Callback(hObject, eventdata, handles)
% hObject    handle to scanWidthText (see GCBO)
% eventdata   reserved - to be defined in a future version of
MATLAB
% handles    structure with handles and user data (see
GUIDATA)

% Hints: get(hObject,'String') returns contents of
scanWidthText as text
%         str2double(get(hObject,'String')) returns contents
of scanWidthText as a double

% --- Executes during object creation, after setting all
properties.
function scanWidthText_CreateFcn(hObject, eventdata,
handles)
% hObject    handle to scanWidthText (see GCBO)
% eventdata   reserved - to be defined in a future version of
MATLAB
% handles    empty - handles not created until after all
CreateFcns called

% Hint: edit controls usually have a white background on
Windows.
%       See ISPC and COMPUTER.
if ispc && isequal(get(hObject,'BackgroundColor'),
get(0,'defaultUicontrolBackgroundColor'))
    set(hObject,'BackgroundColor','white');
end

function scanHeightText_Callback(hObject, eventdata,
handles)
% hObject    handle to scanHeightText (see GCBO)
% eventdata   reserved - to be defined in a future version of
MATLAB
% handles    structure with handles and user data (see
GUIDATA)

```

```

% Hints: get(hObject,'String') returns contents of
scanHeightText as text
% str2double(get(hObject,'String')) returns contents
of scanHeightText as a double

% --- Executes during object creation, after setting all
properties.
function scanHeightText_CreateFcn(hObject, eventdata,
handles)
% hObject    handle to scanHeightText (see GCBO)
% eventdata   reserved - to be defined in a future version of
MATLAB
% handles    empty - handles not created until after all
CreateFcns called

% Hint: edit controls usually have a white background on
Windows.
% See ISPC and COMPUTER.
if ispc && isequal(get(hObject,'BackgroundColor'),
get(0,'defaultUicontrolBackgroundColor'))
    set(hObject,'BackgroundColor','white');
end

function XsamplesText_Callback(hObject, eventdata, handles)
% hObject    handle to XsamplesText (see GCBO)
% eventdata   reserved - to be defined in a future version of
MATLAB
% handles    structure with handles and user data (see
GUIDATA)

% Hints: get(hObject,'String') returns contents of
XsamplesText as text
% str2double(get(hObject,'String')) returns contents
of XsamplesText as a double

% --- Executes during object creation, after setting all
properties.
function XsamplesText_CreateFcn(hObject, eventdata, handles)
% hObject    handle to XsamplesText (see GCBO)
% eventdata   reserved - to be defined in a future version of
MATLAB
% handles    empty - handles not created until after all
CreateFcns called

% Hint: edit controls usually have a white background on
Windows.
% See ISPC and COMPUTER.
if ispc && isequal(get(hObject,'BackgroundColor'),
get(0,'defaultUicontrolBackgroundColor'))
    set(hObject,'BackgroundColor','white');

```

```

end

function YsamplesText_Callback(hObject, eventdata, handles)
% hObject    handle to YsamplesText (see GCBO)
% eventdata   reserved - to be defined in a future version of
MATLAB
% handles    structure with handles and user data (see
GUIDATA)

% Hints: get(hObject,'String') returns contents of
YsamplesText as text
%         str2double(get(hObject,'String')) returns contents
of YsamplesText as a double

% --- Executes during object creation, after setting all
properties.
function YsamplesText_CreateFcn(hObject, eventdata, handles)
% hObject    handle to YsamplesText (see GCBO)
% eventdata   reserved - to be defined in a future version of
MATLAB
% handles    empty - handles not created until after all
CreateFcns called

% Hint: edit controls usually have a white background on
Windows.
%       See ISPC and COMPUTER.
if ispc && isequal(get(hObject,'BackgroundColor'),
get(0,'defaultUicontrolBackgroundColor'))
    set(hObject,'BackgroundColor','white');
end

function edit5_Callback(hObject, eventdata, handles)
% hObject    handle to fileTextbox (see GCBO)
% eventdata   reserved - to be defined in a future version of
MATLAB
% handles    structure with handles and user data (see
GUIDATA)

% Hints: get(hObject,'String') returns contents of
fileTextbox as text
%         str2double(get(hObject,'String')) returns contents
of fileTextbox as a double

% --- Executes during object creation, after setting all
properties.
function edit5_CreateFcn(hObject, eventdata, handles)
% hObject    handle to fileTextbox (see GCBO)
% eventdata   reserved - to be defined in a future version of

```

```

MATLAB
% handles    empty - handles not created until after all
CreateFcns called

% Hint: edit controls usually have a white background on
Windows.
%       See ISPC and COMPUTER.
if ispc && isequal(get(hObject, 'BackgroundColor'),
get(0, 'defaultUicontrolBackgroundColor'))
    set(hObject, 'BackgroundColor', 'white');
end

% --- Executes on button press in singleFreqRadio.
function singleFreqRadio_Callback(hObject, eventdata,
handles)
% hObject    handle to singleFreqRadio (see GCBO)
% eventdata   reserved - to be defined in a future version of
MATLAB
% handles    structure with handles and user data (see
GUIDATA)

% Hint: get(hObject, 'Value') returns toggle state of
singleFreqRadio

% --- Executes on button press in multiFreqRadio.
function multiFreqRadio_Callback(hObject, eventdata,
handles)
% hObject    handle to multiFreqRadio (see GCBO)
% eventdata   reserved - to be defined in a future version of
MATLAB
% handles    structure with handles and user data (see
GUIDATA)

% Hint: get(hObject, 'Value') returns toggle state of
multiFreqRadio

function startFreqText_Callback(hObject, eventdata, handles)
% hObject    handle to startFreqText (see GCBO)
% eventdata   reserved - to be defined in a future version of
MATLAB
% handles    structure with handles and user data (see
GUIDATA)

% Hints: get(hObject, 'String') returns contents of
startFreqText as text
%         str2double(get(hObject, 'String')) returns contents
of startFreqText as a double

% --- Executes during object creation, after setting all

```

```

properties.
function startFreqText_CreateFcn(hObject, eventdata,
handles)
% hObject    handle to startFreqText (see GCBO)
% eventdata   reserved - to be defined in a future version of
MATLAB
% handles    empty - handles not created until after all
CreateFcns called

% Hint: edit controls usually have a white background on
Windows.
%       See ISPC and COMPUTER.
if ispc && isequal(get(hObject, 'BackgroundColor'),
get(0, 'defaultUicontrolBackgroundColor'))
    set(hObject, 'BackgroundColor', 'white');
end


function stopFreqText_Callback(hObject, eventdata, handles)
% hObject    handle to stopFreqText (see GCBO)
% eventdata   reserved - to be defined in a future version of
MATLAB
% handles    structure with handles and user data (see
GUIDATA)

% Hints: get(hObject, 'String') returns contents of
stopFreqText as text
%         str2double(get(hObject, 'String')) returns contents
of stopFreqText as a double

% --- Executes during object creation, after setting all
properties.
function stopFreqText_CreateFcn(hObject, eventdata, handles)
% hObject    handle to stopFreqText (see GCBO)
% eventdata   reserved - to be defined in a future version of
MATLAB
% handles    empty - handles not created until after all
CreateFcns called

% Hint: edit controls usually have a white background on
Windows.
%       See ISPC and COMPUTER.
if ispc && isequal(get(hObject, 'BackgroundColor'),
get(0, 'defaultUicontrolBackgroundColor'))
    set(hObject, 'BackgroundColor', 'white');
end


function FsamplesText_Callback(hObject, eventdata, handles)
% hObject    handle to FsamplesText (see GCBO)
% eventdata   reserved - to be defined in a future version of

```

```

MATLAB
% handles      structure with handles and user data (see
GUIDATA)

% Hints: get(hObject,'String') returns contents of
FsamplesText as text
%           str2double(get(hObject,'String')) returns contents
of FsamplesText as a double

% --- Executes during object creation, after setting all
properties.
function FsamplesText_CreateFcn(hObject, eventdata, handles)
% hObject      handle to FsamplesText (see GCBO)
% eventdata    reserved - to be defined in a future version of
MATLAB
% handles      empty - handles not created until after all
CreateFcns called

% Hint: edit controls usually have a white background on
Windows.
%       See ISPC and COMPUTER.
if ispc && isequal(get(hObject,'BackgroundColor'),
get(0,'defaultUicontrolBackgroundColor'))
    set(hObject,'BackgroundColor','white');
end

% --- Executes during object creation, after setting all
properties.
function loadDataFileText_CreateFcn(hObject, eventdata,
handles)
% hObject      handle to loadDataFileText (see GCBO)
% eventdata    reserved - to be defined in a future version of
MATLAB
% handles      empty - handles not created until after all
CreateFcns called

% Hint: edit controls usually have a white background on
Windows.
%       See ISPC and COMPUTER.
if ispc && isequal(get(hObject,'BackgroundColor'),
get(0,'defaultUicontrolBackgroundColor'))
    set(hObject,'BackgroundColor','white');
end

% --- Executes on button press in browseBtn.
function pushbutton6_Callback(hObject, eventdata, handles)
% hObject      handle to browseBtn (see GCBO)
% eventdata    reserved - to be defined in a future version of
MATLAB
% handles      structure with handles and user data (see
GUIDATA)
```

```

function loadDataFileText_Callback(hObject, eventdata,
handles)
% hObject    handle to loadDataFileText (see GCBO)
% eventdata   reserved - to be defined in a future version of
MATLAB
% handles    structure with handles and user data (see
GUIDATA)

% Hints: get(hObject,'String') returns contents of
loadDataFileText as text
%         str2double(get(hObject,'String')) returns contents
of loadDataFileText as a double

% --- If Enable == 'on', executes on mouse press in 5 pixel
border.
% --- Otherwise, executes on mouse press in 5 pixel border
or over render3dBtn.
function render3dBtn_ButtonDownFcn(hObject, eventdata,
handles)
% hObject    handle to render3dBtn (see GCBO)
% eventdata   reserved - to be defined in a future version of
MATLAB
% handles    structure with handles and user data (see
GUIDATA)

figure;
isosurface(handles.recon_data);

```

```

function set_xy_position(s, x, y, z, delay)

stepsPerInch = 520; %Define scanner resolution
stepsPerDegree = 67;

%fgets(s);
%sit and wait for device to say it has reset to (0,0,0)
%while(s.BytesAvailable == 0) ; end

%fgets(s); % clear serial buffer

x_value = num2str(x); %Write the x-value of that position as
a string.
y_value = num2str(y); %Write the y-value of that position as
a string.
z_value = num2str(z); %Write the z-value of that position as
a string.
delay_value = num2str(delay); %Write the y-value of that
position as a string.

string2Arduino = strcat(x_value,';',y_value,';',z_value,';',
delay_value,';'); %Combine x, y and z together, separated by
;'s.
query(s,string2Arduino);

%disp(string2Arduino);
disp(['Current Point: x = ', num2str((x/stepsPerInch)), ' , y
= ', num2str((y/stepsPerInch)), ' , z = ',
num2str((z/stepsPerDegree))]);
disp(' ');

%This sits and waits for data to be available...
% while(s.BytesAvailable == 0) %While the buffer is empty
(no data has been sent back)
    %No OPeration NOOP
% end %Continuously wait (infinite loop).
% fgets(s); %Gets ok signal from Arduino to proceed.

end

```

```

function [saveFilePath] = save_hol_data(h)

root_dir = h.root_dir;
hol_data = h.hol_data;

saveYesOrNo = questdlg('Keep data?', 'Save
data', 'Yes', 'No', 'Yes');

if( strcmp(saveYesOrNo, 'Yes') )

    % Create data structure for saving
% Root.
Root.m = h.m;
Root.n = h.n;
Root.x_max = h.x_max;
Root.y_max = h.y_max;
Root.x = h.x;
Root.y = h.y;
Root.dx = h.x_max / h.m;
Root.dy = h.y_max / h.n;
Root.zo = 0;
Root.img = 0;    % needed to run through simulation model

Root.angle = h.angle;
Root.p_ind = h.p_ind;
Root.hol_data = h.hol_data;

p = 0;
saveFilePath = [root_dir 'hol_scan_' num2str(p, '%04d')
'.mat'];

while(exist(saveFilePath, 'file') )
    p = p + 1;
    saveFilePath = [root_dir 'hol_scan_'
num2str(p, '%04d') '.mat'];
end

save(saveFilePath, 'Root', '-mat');
end

uiwait(msgbox(['Data saved as: ' saveFilePath], 'Data
Saved', 'modal'));

end
function [hol_data] = run_scan(hObject, handles)
root_dir_turntable = 'C:\Holograms3\';

% osc= handles.OSC;
% fprintf(osc,'*RST: :AUTOSCALE');
osc= handles.OSC;
s = handles.s;
a_data = handles.a_data;

```

```

m = handles.m;
n = handles.n;
    s2 = serial('COM4','BaudRate',9600);      % Connect to
Arduino via Serial


    set(s2,'InputBufferSize',512);
    fopen(s2);    % Open serial port
    x=-400;

    delay=20;
x_value = num2str(x); %Write the x-value of that position as
a string.
%y_value = num2str(y); %Write the y-value of that position
as a string.
%z_value = num2str(z); %Write the z-value of that position
as a string.
delay_value = num2str(delay); %Write the y-value of that
position as a string.

string2Arduino = strcat(x_value,';', delay_value,';');
%Combine x, y and z together, separated by ;'s.
%query(s2,string2Arduino);
x=400;
x_value = num2str(x); %Write the x-value of that position as
a string.
%y_value = num2str(y); %Write the y-value of that position
as a string.
%z_value = num2str(z); %Write the z-value of that position
as a string.
delay_value = num2str(delay); %Write the y-value of that
position as a string.

string2Arduino = strcat(x_value,';', delay_value,';');
%Combine x, y and z together, separated by ;'s.
%query(s2,string2Arduino);
% fprintf(osc,'*RST; :AUTOSCALE');
%
% fprintf(osc,:WAVEFORM:SOURCE CHAN1');           % Specify
data from Channel 1
%
% % Set up VNA frequency scale
% fprintf(osc,:TIMEBASE:REFERENCE CENTER');       % Display
reference at center
% fprintf(osc,:TIMEBASE:RANGE 75E-9');           % Time base to
100 ns full scale
% fprintf(osc,:TIMEBASE:DELAY 0');                 % Delay to
zero
% fprintf(osc,:CHANNEL1:RANGE 1.6');              % Vertical
range to 1.6 V full scale
% fprintf(osc,:CHANNEL1:OFFSET 0');
% fprintf(osc,:WAVEFORM:TYPE? RAW');
% fprintf(osc,:WAVEFORM:BYTEORDER LSBFirst');   % Set the
byte order on the instrument as well

```

```

%
% %
% if(length(f) > 1)
% %    fprintf(vna,['STAR ' num2str(min(f)*10^9)] );      %
Set start freq
% %    fprintf(vna,['STOP ' num2str(max(f)*10^9)] );      %
Set start freq
%    fprintf(osc,'LINFREQ;');                                % Set to
linear-sweep mode
% %    fprintf(vna,['POIN ' num2str(length(f)) ';' ] );
% %    fprintf(vna,'MANTRIG;');                                % Enable manual
sweep trigger
% else
% %    fprintf(vna,'SENS:SWEEP:TYPE CW'); % Put analyzer
in CW mode
%    fprintf(osc,['CWFREQ ' num2str(f*10^9)]);
% end
%
% Get the nr of trace points
% Get the reference level
% fprintf(osc,:WAVEFORM:DATA? );
% WaveformRawData = fscanf(osc);
% temp = str2num(WaveformRawData);
% holLength=length(temp)
rotations=10;
scan_iterations=1;
% meas_data = zeros( length(a_data),length(f) );
fprintf(osc,:WAVEFORM:DATA? );
WaveformRawData = fscanf(osc);
temp = str2num(WaveformRawData);
hol_data = zeros(n, m,scan_iterations, length(temp));

axes(handles.holAxes);

x_ind = handles.p_ind(:,2);      % indices switched for
imagesc(... .
y_ind = handles.p_ind(:,1);
    x = a_data(1,1);
    y = a_data(1,2);
    angle = a_data(1,3);
    delay = a_data(1,4);
set_xy_position(s,x,y,angle,delay);
pause

x = a_data(1,1);
y = a_data(1,2);
angle = a_data(1,3);
delay = a_data(1,4);

set_xy_position(s,x,y,angle,delay);
pause(10)
for c=1:rotations

for i = 1:length(a_data)

```

```

x = a_data(i,1);
y = a_data(i,2);
angle = a_data(i,3);
delay = a_data(i,4);

set_xy_position(s,x,y,angle,delay);

pause(1);

%query(pxa,'OPC?;SING;');
op. complete % Wait till
% fprintf(osc,:WAVEFORM:DATA?' );
% WaveformRawData = fscanf(osc);
% length(str2num(WaveformRawData))
% % hol_data(x_ind(i),y_ind(i),:) =
str2num(WaveformRawData);
% %
% for j=1:scan_iterations
% fprintf(osc,:WAVEFORM:DATA?' );
% WaveformRawData = fscanf(osc);
% temp = str2num(WaveformRawData);
% hol_data(x_ind(i),y_ind(i),c,j,:)=temp;
% pause(2)
% end
for j=1:scan_iterations
fprintf(osc,:WAVEFORM:DATA?' );
WaveformRawData = fscanf(osc);
temp = str2num(WaveformRawData);
hol_data(x_ind(i),y_ind(i),j,:)=temp;
pause(2)
end
% figure(1)
% imagesc(abs(hol_data(:,:,c,1)));
% axis image;
% guidata(hObject, handles.holAxes);
pause(0.01);
data=hol_data(x_ind(i),y_ind(i),1,:);
data=squeeze(data);
dt=10*10^-9;
fs=1/dt;
N=length(temp);
df=1/(N*dt);
freqs=(0:N/2)*40000000;
Fx=fft(temp);
Fx2=Fx(1:(N/2+1));
% figure(2)
% stem(freqs(1:500),Fx2(1:500))
% figure(3)
% stem(abs(Fx2(1:3198)))
mvariable=abs(Fx2(1:3198));
for k=3:(length(mvariable)-3)
meanvariable(k)=(mvariable(k-2)+mvariable(k-1)+mvariable(k)+mvariable(k+1)+mvariable(k+2))/5;
end

```

```

meanvariable(1)=0;
meanvariable(2)=0;
meanvariable=20*log10(meanvariable);
%figure(4)
%plot(meanvariable(1:500))
% activate the grid lines

% Disconnect an clean up

end
fclose(s);
s = serial('COM10','BaudRate',9600);      % Connect to
Arduino via Serial

set(s,'InputBufferSize',512);
fopen(s);    % Open serial port
fgets(s);   % Clear junk data
x=40;
x_value = num2str(x); %Write the x-value of that position as
a string.
%y_value = num2str(y); %Write the y-value of that position
as a string.
%z_value = num2str(z); %Write the z-value of that position
as a string.
delay_value = num2str(delay); %Write the y-value of that
position as a string.

string2Arduino = strcat(x_value,';', delay_value,';');
%Combine x, y and z together, separated by ;'s.
query(s2,string2Arduino);
pause(120)
p = 0;
saveFilePath = [root_dir_turntable 'hol_scan_'
num2str(p,'%04d') '.mat'];

while(exist(saveFilePath,'file'))
    p = p + 1;
    saveFilePath = [root_dir_turntable 'hol_scan_'
num2str(p,'%04d') '.mat'];
end

save(saveFilePath,'hol_data','-mat');
end
fclose(s2);
guidata(hObject, handles);

```

```

function [file, pos_data, pos_ind] =
create_pos_data(NofXpts, NofYpts, Xrange, Yrange, angle)

delay = 300;      % delay between measurements, milliseconds

X = linspace(0,Xrange,NofXpts);
Y = linspace(0,Yrange,NofYpts);

file = 'xy_pos_data.txt';
delete(file);
fid = fopen(file, 'w');

pos_data = zeros(length(X)*length(Y), 4);
pos_ind = zeros(length(X)*length(Y), 3);
n = 1;

for i = 1:length(angle)
    for j = 1:length(Y)
        if( mod(j,2) )
            for k = 1:1:length(X)
                pos_ind(n,1) = k;
                pos_ind(n,2) = j;
                pos_ind(n,3) = i;
                pos_data(n,1) = X(k);
                pos_data(n,2) = Y(j);
                pos_data(n,3) = angle;
                pos_data(n,4) = delay;

                fprintf(fid, '%2.3f %2.3f %2.3f %4.0f
\n', X(k), Y(j), angle, delay);

                n = n + 1;
            end
        else
            for k = length(X):-1:1
                pos_ind(n,1) = k;
                pos_ind(n,2) = j;
                pos_ind(n,3) = i;
                pos_data(n,1) = X(k);
                pos_data(n,2) = Y(j);
                pos_data(n,3) = angle;
                pos_data(n,4) = delay;
                fprintf(fid, '%2.3f %2.3f %2.3f %4.0f
\n', X(k), Y(j), angle, delay);
                n = n + 1;
            end
        end
    end
end

fclose(fid);

```



```

function [Arduino_data] = check_position_data(position_data)

%Define the limits in inches of the scanner
x_limit = 35.6;
y_limit = 35.6;
z_limit = 360;

%Find the indices of values that are outside of the scanner
bounds
ix1 = find(position_data(:,1) > x_limit);
iy1 = find(position_data(:,2) > y_limit);
iz1 = find(position_data(:,3) > z_limit);

%make sure the value are positive....
ix2 = find(position_data(:,1) < 0);
iy2 = find(position_data(:,2) < 0);
iz2 = find(position_data(:,3) < 0);

%put the bad data indicies together
ix = [ix1 ix2];
iy = [iy1 iy2];
iz = [iz1 iz2];

%Find the x and y values that are outside of the scanner
bounds
bad_x_vals = position_data(ix,1);
bad_y_vals = position_data(iy,2);
bad_z_vals = position_data(iz,3);

if ( (length(ix) ~= 0) || (length(iy) ~=0) || (length(iz)
~=0) ) %If there is at least one value outside of the range
    for c = 1:length(ix) %Display x-values and indices that
exceed range
        disp(['Your x value of ' num2str(bad_x_vals(c)) ' '
inches in point number ' ...
        num2str(ix(c)) ' are out of the ' ...
        num2str(x_limit) ' inch range. Please revise.'])
    end
    for c = 1:length(iy) %Display y-values and indices that
exceed range
        disp(['Your y value of ' num2str(bad_y_vals(c)) ' '
inches in point number ' ...
        num2str(iy(c)) ' are out of the ' ...
        num2str(y_limit) ' inch range. Please revise.'])
    end
    for c = 1:length(iz) %Display z-values and indices that
exceed range
        disp(['Your z value of ' num2str(bad_z_vals(c)) ' '
degrees in point number ' ...
        num2str(iz(c)) ' are out of the ' ...
        num2str(z_limit) ' degree range. Please revise.'])
    end
    error('Exiting m-file') %Exit the m-file35
else %If no values are outside the range

```

```

    disp('All values are within bounds of scanner!') %Let
the user know the scan will proceed
end

%Convert position data to step information
stepsPerInch = 520; %Define scanner resolution
stepsPerDegree = 67;
step_data_x = round(stepsPerInch*position_data(:,1) );
%Convert x direction to steps
step_data_y = round(stepsPerInch*position_data(:,2) );
%Convert to steps
step_data_z = round(stepsPerDegree*position_data(:,3));
%Convert to steps
delay = position_data(:,4);

%Add in delay column
Arduino_data = [step_data_x step_data_y step_data_z delay];
end

```

```

function [kx ky kz] = calc_wavenums(freqs, Ny, Nx)

freqs = freqs;
c = 3e8;                                     % speed of light
k = 2*pi*freqs/c;                           % wave number(s)
NofFreqs = length(freqs);
kx = zeros(Ny,Nx,NofFreqs);
ky = kx;
kz = kx;

for i = 1:NofFreqs
    for j = 1:Ny
        kx(j,:,:i) = linspace(-2*k(i), 2*k(i), Nx);
    end
    for j = 1:Nx
        ky(:,j,i) = linspace(-2*k(i), 2*k(i), Ny);
    end
    kz(:,:,i) = sqrt(4*k(i)^2 - kx(:,:,i).^2 -
ky(:,:,i).^2);
    end
end

```

```

#define xpinClk 6
#define xpinDir 8
#define ypinClk 5
#define ypinDir 7
#define zpinClk 4
#define zpinDir 9
#define pinStop 2
#define pinsensor 10

int StepsX;
int StepsY;
int StepsZ;
int PauseBtwPoints;
int targetStepsX;
int targetStepsY;
int targetStepsZ;
int xPos = 0;
int yPos = 0;
int zPos = 0;
int endStop;
int MoveDelay = 500; //This controls the speed of the
scanner.
int sensor;

void setup() {
    pinMode(xpinClk,OUTPUT);
    pinMode(xpinDir,OUTPUT);
    pinMode(ypinClk,OUTPUT);
    pinMode(ypinDir,OUTPUT);
    pinMode(zpinClk,OUTPUT);
    pinMode(zpinDir,OUTPUT);
    pinMode(pinStop,INPUT);
    pinMode(pinsensor,INPUT);
    digitalWrite(pinStop,HIGH);
    Serial.begin(9600);
    Serial.setTimeout(10);
    Serial.flush();
    Serial.println(digitalRead(sensor));
    SetToHome();
    Serial_flush(); // once home is set, set the serial port
to let matlab know
}

void loop() {
    //This is the main code that will run for each
coordinate.
    while(Serial.available() < 1){ //Wait for a data point
to be sent over serial
    }
    StepsX = Serial.parseInt(); //X value in steps
    StepsY = Serial.parseInt(); //Y value in steps
    StepsZ = Serial.parseInt(); //Z value in steps
    PauseBtwPoints = Serial.parseInt(); //Delay in
}

```

```

milliseconds

    if(StepsX > xPos)
        digitalWrite(xpinDir,LOW);
    else
        digitalWrite(xpinDir,HIGH);
    if(StepsY < yPos)
        digitalWrite(ypinDir,LOW);
    else
        digitalWrite(ypinDir,HIGH);

    targetStepsX = abs(StepsX - xPos); //Calculate target X
    value using current X position.
    targetStepsY = abs(StepsY - yPos); //Calculate target Y
    value using current Y position.
    targetStepsZ = abs(StepsZ - zPos); //Calculate target Z
    value using current Z position.

    MoveXMot(targetStepsX);
    MoveYMot(targetStepsY);
    MoveRotMot(targetStepsZ);
    xPos = StepsX;
    yPos = StepsY;
    zPos = StepsZ;
    Serial_flush();
}

void MoveRotMot(int stepsZ)
{
    int k = 1;

    if(stepsZ > 0){
        digitalWrite(zpinDir,HIGH);
        for( k; k <=(stepsZ); k++)
        {

            digitalWrite(zpinClk,HIGH);
            delayMicroseconds(MoveDelay);
            digitalWrite(zpinClk,LOW);
            delayMicroseconds(MoveDelay);
        }
        digitalWrite(zpinClk,HIGH);
    }
    else{
        if(stepsZ < 0){
            digitalWrite(zpinDir,LOW);
            for( k; k >=(stepsZ); k--)
            {
                digitalWrite(zpinClk,LOW);
                delayMicroseconds(MoveDelay);
                digitalWrite(zpinClk,HIGH);
                delayMicroseconds(MoveDelay);
            }
        }
    }
}

```

```

        digitalWrite(zpinClk,LOW);
    }
}

void Serial_flush(){
    while(Serial.available()>0){
        Serial.read();
    }
    delay(PauseBtwPoints); //Delay to give positions time to
settle.
    Serial.println(1); //Print value to line telling MATLAB to
continue
}

void SetToHome(){
    //Set X Home
    endStop = digitalRead(pinStop);
    digitalWrite(xpinDir,HIGH);
    while(endStop != 1){
        endStop = digitalRead(pinStop);
        digitalWrite(xpinClk,HIGH);
        delayMicroseconds(MoveDelay);
        digitalWrite(xpinClk,LOW);
        delayMicroseconds(MoveDelay);

    }
    delay(500);
    digitalWrite(xpinDir,LOW);
    for(int j=1;j<=50;j++){
        digitalWrite(xpinClk,HIGH);
        delayMicroseconds(MoveDelay);
        digitalWrite(xpinClk,LOW);
        delayMicroseconds(MoveDelay);
    }
    delay(1000);
    xPos = 0;

    //Set Y home
    endStop = digitalRead(pinStop);
    digitalWrite(ypinDir,LOW);
    while(endStop != 1){
        endStop = digitalRead(pinStop);
        digitalWrite(ypinClk,HIGH);
        delayMicroseconds(MoveDelay);
        digitalWrite(ypinClk,LOW);
        delayMicroseconds(MoveDelay);
    }

    digitalWrite(ypinDir,HIGH);
    delay(500);
    for(int l=1;l<=50;l++){
        digitalWrite(ypinClk,HIGH);

```

```

        delayMicroseconds(MoveDelay);
        digitalWrite(yPinClk,LOW);
        delayMicroseconds(MoveDelay);
    }
    delay(1000);
    yPos = 0;

    //Set Z Home
    /*
    sensor = digitalRead(pinSensor);
    while(sensor != 0)
    {
        digitalWrite(zPinClk,HIGH);
        delayMicroseconds(MoveDelay);
        digitalWrite(zPinClk,LOW);
        delayMicroseconds(MoveDelay);
        sensor = digitalRead(pinSensor);
    }
    delay(200);
    digitalWrite(zPinDir,HIGH);
    for(int j=1;j<=450;j++){
        digitalWrite(zPinClk,HIGH);
        delayMicroseconds(MoveDelay);
        digitalWrite(zPinClk,LOW);
        delayMicroseconds(MoveDelay);
    }
    zPos=0;
    delay(500);
    */
    Serial_flush();
}

void e_STOP(){
    digitalWrite(xPinClk,LOW);
    digitalWrite(yPinClk,LOW);
    while(1){
    }
}

void MoveXMot(int stepsX)
{
    endStop = digitalRead(pinStop);
    if(endStop == 1)
        e_STOP();

    for( int k=0; k <= stepsX; k++)
    {
        digitalWrite(xPinClk,HIGH);
        delayMicroseconds(MoveDelay);
        digitalWrite(xPinClk,LOW);
        delayMicroseconds(MoveDelay);
    }
}

```

```
void MoveYMot(int stepsY)
{
    endStop = digitalRead(pinStop);
    if(endStop == 1)
        e_STOP();

    for( int k=0; k <= stepsY; k++)
    {
        digitalWrite(ypinClk,HIGH);
        delayMicroseconds(MoveDelay);
        digitalWrite(ypinClk,LOW);
        delayMicroseconds(MoveDelay);
    }
}
```

## REFERENCES

- [1] Broquetas, A., Jordi, R., Rius, J.M., Elias-Fuste, A.R., Cardama, A., and Jofre, L., "Cylindrical geometry: a further step in active microwave tomography," *IEEE Transactions on Microwave Theory and Techniques* 39, 836-844 (1991).
- [2] Bolomey, J.-C., and Pichot, C., "Microwave tomography: from theory to practical imaging systems," *International Journal of Imaging Systems and Technology* 2, 144-156 (1990).
- [3] T.M. Grzegorczyk, P.M. Meaney, P.A. Kaufman, R.M. di Florio-Alexander, and K.D. Paulsen, "Fast 3-D tomographic microwave imaging for breast cancer detection," *IEEE Transactions on Medical Imaging*, vol. 31, pp. 1584–1592, 2012.
- [4] M.H. Khalil, W. Shahzad, and J.D. Xu, "In the medical field detection of breast cancer by microwave imaging is a robust tool," in *Proceedings of the 25<sup>th</sup> International Vacuum Nanoelectronics Conference (IVNC)*, Jeju, South Korea, July 2012, 2 pages, doi: 10.1109/IVNC.2012.6316913.
- [5] Z. Wang, E.G. Lim, Y.Tang, and M. Leach, "Medical applications of microwave imaging," *The Scientific World Journal*, Article ID 147016, vol. 2014, 2014, 7 pages, doi: 10.1155/2014/147016.
- [6] Semenov, S.Y., Svenson, R.H., Boulyshev, A.E., Souvorov, A.E., Borisov, V.Y., Sizov, Y., Starostin, A.N., Dezern, K.R., Tatsis, G.P., and Baranov, V.Y., "Microwave tomography: two-dimensional system for biological imaging, *IEEE Transactions on Biomedical Engineering* 43, 869-877 (1996).

- [7] Verity, A., Gavrilov, S., Adigüzel, T., Voynovskyy, I., Yüceer, G., and Salman, A.O. (1999). “C-band tomography system for imaging of cylindrical objects,” in [Proc. SPIE Conference on Subsurface Sensors and Applications], Denver, CO, 224-230 (1999).
- [8] Tseng, C.-H., and Chu, T.-H., “An effective usage of vector network analyzer for microwave imaging,” IEEE Transactions on Microwave Theory and Techniques 53, 2884-2891 (2005).
- [9] Gilmore, C., Mojabi, P., Zakaria, A., Ostadrahimi, M., Kaye, C., Noghanian, S., Shafai, L., Pistorius, S., and LoVetri, J. (2009). “An ultra-wideband microwave tomography system: preliminary results,” in [Proc. Annual International Conference of the IEEE Engineering in Medicine and Biology Society (EMBC 2009)], Minneapolis, MN, 2288-2291 (2009).
- [10] Abdullah, M.Z., Binajjaj, S.A., Zanoon, T.F., and Peyton, A.J., “High-resolution imaging of dielectric profiles by using a time-domain ultra wideband radar sensor,” Measurement 44, 859-870 (2011).
- [11] Kim, Y.J., Jofre, L., De Flaviis, F., and Feng, M.Q., “Microwave reflection tomographic array for damage detection of civil structures,” IEEE Transactions on Antennas and Propagation 51, 3022-3032 (2003).
- [12] Zimdars, D., and White, J.S. (2004). “Terahertz reflection imaging for package and personnel inspection,” in [Proc. SPIE Conf. on Terahertz for Military and Security Applications II], Orlando, FL, 78-83 (2004).

- [13] Li, X., Bond, E.J., Van Veen, B.D., and Hagness, S.C., “An overview of ultra-wideband microwave imaging via space-time beamforming for early-stage breast-cancer detection,” IEEE Antennas and Propagation Magazine 47(1), 19-34 (2005).
- [14] Horton, B.M., “Noise-modulated distance measuring systems,” Proceedings of the IRE 47, 821-828 (1959).
- [15] Grant, M.P., Cooper, G.R., and Kamal, A.K., “A class of noise radar systems,” Proceedings of the IEEE 51, 1060- 1061 (1963).
- [16] Lukin, K.A., “Noise radar technology,” Telecommunications and Radio Engineering 55, 8-16 (2001).
- [17] Narayanan, R.M., and Xu, X. (2003). “Principles and applications of coherent random noise radar technology,” In [Proc. SPIE Conference on Noise in Devices and Circuits], Santa Fe, NM, 503-514 (2003).
- [18] Axelsson, S.R.J., “Noise radar using random phase and frequency modulation,” IEEE Transactions on Geoscience and Remote Sensing 42, 2370-2384 (2004).
- [19] Turner, L. (1991). “The evolution of featureless waveforms for LPI communications,” in [Proc. IEEE 1991 National Aerospace and Electronics Conference (NAECON)], Dayton, OH, 1325-1331 (1991).
- [20] Vela, R., Narayanan, R.M., Gallagher, K.A., and Rangaswamy, M. (2012). “Noise radar tomography,” In [Proc. IEEE Radar Conference], Atlanta, GA, 720-724 (2012).
- [21] Shin, H.J., Narayanan, R.M., and Rangaswamy, M., “Ultrawideband noise radar imaging of impenetrable cylindrical objects using diffraction tomography,” International Journal of Microwave Science and Technology 2014, 601659, doi: 10.1155/2014/601659 (2014).

- [22] Shin, H.J., Narayanan, R.M., and Rangaswamy, M. (2014). “Ultra-wideband noise radar imaging of cylindrical PEC objects using diffraction tomography,” in [Proc. SPIE Conference on Radar Sensor Technology XVIII], Baltimore, MD, 90770J1-90770J10 (2014).

## Publications

### Journal Papers:

1. H.J. Shin, R.M. Narayanan, and M. Rangaswamy, "Ultrawideband Noise Radar Imaging of Impenetrable Cylindrical Objects using Diffraction Tomography," *International Journal of Microwave Science and Technology*, Vol. 2014, Article ID 601659, 22 pages, 2014, doi: 10.1155/2014/601659.
2. H.J. Shin, M.A. Asmuth, R.M. Narayanan, and M. Rangaswamy, "Radar Tomography Using Ultrawideband Noise Waveforms: Basic Principles, Simulations, and Experimental Validation," *Progress in Electromagnetics Research B*, submitted and under review.

### Conference Papers:

1. H.J. Shin, R.M. Narayanan, and M. Rangaswamy, "Tomographic Imaging with Ultra-wideband Noise Radar using Time-domain Data," *Proc. SPIE Conference on Radar Sensor Technology XVII*, Baltimore, MD, Vol. 8714, pp. 87140R-1–87140R-9, April 2013, doi: 10.1117/12.2016898.
2. H.J. Shin, R.M. Narayanan, and M. Rangaswamy, "Ultra-Wideband Noise Radar Imaging of Cylindrical PEC Objects using Diffraction Tomography," *Proc. SPIE Conference on Radar Sensor Technology XVIII*, Baltimore, MD, Vol. 9077, pp. 90770J-1–90770J-10, May 2014, doi: 10.1117/12.2050133.
3. H.J. Shin, R.M. Narayanan, and M. Rangaswamy, "Diffraction Tomography for Ultra-Wideband Noise Radar and Imaging Quality Measure of a Cylindrical Perfect Conducting Object," *Proc. IEEE Radar Conference (RadarCon 2014)*, Cincinnati, OH, pp. 702–707, May 2014.
4. H.J. Shin, M.A. Asmuth, R.M. Narayanan, and M. Rangaswamy, "Principle and Experimental Results of Ultra-Wideband Noise Radar Imaging of a Cylindrical Conducting Object Using Diffraction Tomography," *Proc. SPIE Conference on Radar Sensor Technology XIX and Active and Passive Signatures VI*, Baltimore, MD, Vol. 9461, pp. 94610V-1–94610V-11, April 2015, doi: 10.1117/12.2176752.
5. M.A. Asmuth, H.J. Shin, R.M. Narayanan, and M. Rangaswamy, "Design and Implementation of a Noise Radar Tomographic System," *Proc. SPIE Conference on Radar Sensor Technology XIX and Active and Passive Signatures VI*, Baltimore, MD, Vol. 9461, pp. 94610W-1–94610W-9, April 2015, doi: 10.1117/12.2176753.
6. H.J. Shin, R.M. Narayanan, and M. Rangaswamy, "Simulations of Tomographic Imaging of Various Target Scenarios Using Noise Waveforms," *Proc. IEEE International Radar Conference*, Arlington, VA, pp. 963–968, May 2015.

1.

**1. Report Type**

Final Report

**Primary Contact E-mail**

**Contact email if there is a problem with the report.**

ram@engr.psu.edu

**Primary Contact Phone Number**

**Contact phone number if there is a problem with the report**

8148632602

**Organization / Institution name**

Pennsylvania State University

**Grant/Contract Title**

**The full title of the funded effort.**

Noise Tomography and Adaptive Illumination in Noise Radar

**Grant/Contract Number**

**AFOSR assigned control number. It must begin with "FA9550" or "F49620" or "FA2386".**

FA9550-12-1-0164

**Principal Investigator Name**

**The full name of the principal investigator on the grant or contract.**

Ram Narayanan

**Program Manager**

**The AFOSR Program Manager currently assigned to the award**

Dr. Arje Nachman

**Reporting Period Start Date**

04/01/2012

**Reporting Period End Date**

08/31/2015

**Abstract**

Ultra-wideband (UWB) waveforms achieve excellent spatial resolution for better characterization of targets in tomographic imaging applications compared to narrowband waveforms. In this report, two-dimensional tomographic images of multiple scattering objects are successfully obtained using the diffraction tomography approach by transmitting multiple independent and identically distributed (iid) UWB random noise waveforms. The feasibility of using a random noise waveform for tomography is investigated by formulating a white Gaussian noise (WGN) model using spectral estimation. The analytical formulation of object image formation using random noise waveforms is established based on the backward scattering, and several numerical diffraction tomography simulations are performed in the spatial frequency domain to validate the analytical results by reconstructing the tomographic images of scattering objects. The final image of the object based on multiple transmitted noise waveforms is reconstructed by averaging individually formed images which compares very well with the image created using the traditional Gaussian pulse. Pixel difference-based measure is used to analyze and estimate the image quality of the final reconstructed tomographic image under various signal-to-noise ratio (SNR) conditions. A UWB noise radar was designed to transmit multiple UWB random noise waveforms over the 3–5 GHz frequency range and to measure the backward scattering data for the validation of the theoretical analysis and numerical simulation results. The reconstructed tomographic images of the rotating cylindrical objects based on DISTRIBUTION A: Distribution approved for public release.

experimental results are seen to be in good agreement with the simulation results, which demonstrates the capability of UWB noise radar for complete two-dimensional tomographic image reconstruction of various shaped metallic and dielectric target objects.

### Distribution Statement

This is block 12 on the SF298 form.

Distribution A - Approved for Public Release

### Explanation for Distribution Statement

If this is not approved for public release, please provide a short explanation. E.g., contains proprietary information.

### SF298 Form

Please attach your [SF298](#) form. A blank SF298 can be found [here](#). Please do not password protect or secure the PDF. The maximum file size for an SF298 is 50MB.

[FINAL Report Cover Page.pdf](#)

**Upload the Report Document. File must be a PDF. Please do not password protect or secure the PDF . The maximum file size for the Report Document is 50MB.**

[Final report.pdf](#)

**Upload a Report Document, if any. The maximum file size for the Report Document is 50MB.**

### Archival Publications (published) during reporting period:

Journal Papers:

1. H.J. Shin, R.M. Narayanan, and M. Rangaswamy, "Ultrawideband Noise Radar Imaging of Impenetrable Cylindrical Objects using Diffraction Tomography," International Journal of Microwave Science and Technology, Vol. 2014, Article ID 601659, 22 pages, 2014, doi: 10.1155/2014/601659.

2. H.J. Shin, M.A. Asmuth, R.M. Narayanan, and M. Rangaswamy, "Radar Tomography Using Ultrawideband Noise Waveforms: Basic Principles, Simulations, and Experimental Validation," Progress in Electromagnetics Research B, submitted and under review.

Conference Papers:

1. H.J. Shin, R.M. Narayanan, and M. Rangaswamy, "Tomographic Imaging with Ultra-wideband Noise Radar using Time-domain Data," Proc. SPIE Conference on Radar Sensor Technology XVII, Baltimore, MD, Vol. 8714, pp. 87140R-1–87140R-9, April 2013, doi: 10.1117/12.2016898.

2. H.J. Shin, R.M. Narayanan, and M. Rangaswamy, "Ultra-Wideband Noise Radar Imaging of Cylindrical PEC Objects using Diffraction Tomography," Proc. SPIE Conference on Radar Sensor Technology XVIII, Baltimore, MD, Vol. 9077, pp. 90770J-1–90770J-10, May 2014, doi: 10.1117/12.2050133.

3. H.J. Shin, R.M. Narayanan, and M. Rangaswamy, "Diffraction Tomography for Ultra-Wideband Noise Radar and Imaging Quality Measure of a Cylindrical Perfect Conducting Object," Proc. IEEE Radar Conference (RadarCon 2014), Cincinnati, OH, pp. 702–707, May 2014.

4. H.J. Shin, M.A. Asmuth, R.M. Narayanan, and M. Rangaswamy, "Principle and Experimental Results of Ultra-Wideband Noise Radar Imaging of a Cylindrical Conducting Object Using Diffraction Tomography," Proc. SPIE Conference on Radar Sensor Technology XIX and Active and Passive Signatures VI, Baltimore, MD, Vol. 9461, pp. 94610V-1–94610V-11, April 2015, doi: 10.1117/12.2176752.

5. M.A. Asmuth, H.J. Shin, R.M. Narayanan, and M. Rangaswamy, "Design and Implementation of a Noise Radar Tomographic System," Proc. SPIE Conference on Radar Sensor Technology XIX and Active and Passive Signatures VI, Baltimore, MD, Vol. 9461, pp. 94610W-1–94610W-9, April 2015, doi:

DISTRIBUTION A: Distribution approved for public release.

10.1117/12.2176753.

6. H.J. Shin, R.M. Narayanan, and M. Rangaswamy, "Simulations of Tomographic Imaging of Various Target Scenarios Using Noise Waveforms," Proc. IEEE International Radar Conference, Arlington, VA, pp. 963–968, May 2015.

**Changes in research objectives (if any):**

None.

**Change in AFOSR Program Manager, if any:**

The project was managed at the start by Dr. Jon Sjogren. Following his retirement, the project was managed by Dr. Tristan Nguyen. The current Program Manager is Dr. Arje Nachman.

**Extensions granted or milestones slipped, if any:**

No cost extension given to move the end date from 31 March 2015 to 31 August 2015.

**AFOSR LRIR Number**

**LRIR Title**

**Reporting Period**

**Laboratory Task Manager**

**Program Officer**

**Research Objectives**

**Technical Summary**

**Funding Summary by Cost Category (by FY, \$K)**

	Starting FY	FY+1	FY+2
Salary			
Equipment/Facilities			
Supplies			
Total			

**Report Document**

**Report Document - Text Analysis**

**Report Document - Text Analysis**

**Appendix Documents**

**2. Thank You**

**E-mail user**

Sep 29, 2015 13:39:48 Success: Email Sent to: ram@engr.psu.edu